

# Near- and mid-infrared studies of the Galactic Center and Sagittarius A<sup>\*</sup>

INAUGURAL-DISSERTATION

zur

Erlangung des Doktorgrades  
der Mathematisch-Naturwissenschaftlichen Fakultät  
der Universität zu Köln

vorgelegt von

**Thomas Viehmann**  
aus Leiden (Niederlande)

Köln 2007

Berichterstatter:

Prof. Dr. A. Eckart

Prof. Dr. M. Abd-Elmeguid

Tag der mündlichen Prüfung:

06. Juli 2007

# Kurzzusammenfassung

Das Hauptaugenmerk dieser Doktorarbeit liegt auf der Analyse und Interpretation von Nah- und Midinfrarotbildern der Zentralregion der Milchstraße, mit dem Ziel, das Verständnis dieser Region, insbesondere bei längeren Wellenlängen, zu erhöhen.

Photometrie von Aufnahmen mit großem Gesichtsfeld ( $70'' \times 70''$ ) in mehreren Infrarot-Wellenlängenbändern ( $H$ ,  $K$ ,  $L$  und  $M$ , d.h. 1.6, 2.1, 3.78 und  $4.66 \mu\text{m}$ ) führt zu einer neuen Flußdichtenkalibration für das  $L$ -Band, welche die merkwürdigen Farbeffekte, die in früheren Studien des zentralen Sternhaufens auftraten, eliminiert. Die erhaltenen Farbdaten deuten darauf hin, daß die mittlere Extinktion zum galaktischen Zentrum, insbesondere zu der Region, in der der nördliche Arm der "Minispirale" und Sgr A\* liegen, niedriger ist als bisher angenommen. Dies bestätigt die Ergebnisse von Scoville et al. (2003). Der Vergleich der Sternpopulation in den inneren paar Bogensekunden mit derjenigen weiter außen, d.h. bis zu etwa einer halben Bogenminute von der Position von Sgr A\* entfernt, ergibt, daß die Extinktion über das gesamte Gesichtsfeld des ISAAC-Instrumentes ( $70'' \times 70''$ ) nicht signifikant zunimmt. Mit Hilfe der großen Anzahl untersuchter Quellen (über 500) läßt sich die  $M$ -Band-Extinktion aus der mittleren ( $L - M$ )-Farbe bestimmen, was einen höheren Wert als den des "Standard"-Extinktionsgesetzes von Rieke & Lebofsky (1985) ergibt. Es zeigt sich, daß die ( $L - M$ )-Farbe ein nützliches diagnostisches Werkzeug darstellt, um heiße und kühle Sterne voneinander zu unterscheiden, insbesondere dann, wenn genauere Methoden (z.B. Spektroskopie) nicht zur Verfügung stehen. Die ungewöhnliche Morphologie der hellen Midinfrarotquelle IRS 3 wird ebenfalls diskutiert. Aus der Analyse der ersten  $N$ - und  $Q$ -Band-Beobachtungen ( $\approx 10$  und  $20 \mu\text{m}$  Wellenlänge) mit VISIR ("Commissioning"-Phase) ergibt sich die bisher umfangreichste Untersuchung von Midinfrarotquellen im Zentrum der Milchstraße (bis zu 64 Quellen bei  $8.6 \mu\text{m}$ ). Zum ersten Mal konnten viele stellare Quellen, wie die heißen Helium-Emissionslinien-Sterne IRS 16NE, IRS 16NW und AF/AHH sowie die roten Riesen IRS 12, IRS 14NE und IRS 14SW im  $N$ -Band nachgewiesen werden. Durch Kombination der VISIR-Daten mit Daten aus kürzeren Wellenlängenbereichen konnte eine bisher unerreichte Anzahl von spektralen Energieverteilungen (SEDs) über den Nah- und Midinfrarotbereich von 1.6 bis  $19.5 \mu\text{m}$  aufgestellt werden. Diese SEDs lassen sich nach ihren Eigenschaften wie folgt klassifizieren: 1. eingebettete Quellen des nördlichen Arms, 2. Bugwellenobjekte mit niedrigerer Leuchtkraft, 3. kühle Sterne, 4. heiße Sterne sowie 5. unbekannte Quellen, einschließlich IRS 3. Ein Vergleich der Daten bei  $11.3 \mu\text{m}$  Wellenlänge mit denen bei benachbarten Wellenlängen liefert Hinweise auf Quellen mit intrinsischer, durch das Objekt selbst hervorgerufener Silikat-Absorption, welche ein Anzeichen für die Bildung von Staub darstellt. Desweiteren wird eine Gruppe heller Midinfrarotquellen vorgestellt, welche östlich von IRS 5 liegt und ungewöhnliche, bisher nicht erklärte Eigenschaften besitzt.

Midinfrarotflußdichten, die an der Position von Sgr A\*, dem supermassiven schwarzen

---

Loch im Zentrum der Milchstraße, gewonnen wurden, ergänzen die Ergebnisse der Multi-Wellenlängen-Kampagne des Jahres 2004 zur Beobachtung und Überwachung von Sgr A\*. Hierdurch werden den theoretischen Modellen, die die spektrale Energieverteilung von Sgr A\* sowohl während seiner Nahinfrarot- und Röntgenausbrüche, als auch im Quasi-Ruhezustand erklären sollen, engere Grenzen gesteckt, insbesondere, da gezeigt wird, daß fast die gesamte beobachtete Midinfrarotflußdichte an der Position von Sgr A\* von warmem Staub hervorgerufen wird. Es scheint, daß ein Modell mit Synchrotronstrahlung und einem durch Compton-Streuung an derselben Elektronenpopulation erzeugten Anteil höherenergetischer Strahlung (SSC – “Synchrotron Self-Compton”) ein vielversprechendes Konzept darstellt, um die beobachteten spektralen Energieverteilungen zu modellieren.

# Abstract

The focus of this thesis lies on the analysis and interpretation of near- and mid-infrared images of the Galactic center, with a view to improving the understanding of this region, especially at longer wavelengths.

Multi-band ( $H$ ,  $K$ ,  $L$  and  $M$ , i.e. 1.6, 2.1, 3.78 and 4.66  $\mu\text{m}$ ) photometry of images with a large field of view results in a new  $L$ -band calibration which eliminates anomalous color effects found in previous surveys of the Galactic center stellar cluster. The color data obtained indicates that the average extinction toward the region containing the Northern Arm and Sgr A\* is lower than previously assumed, confirming the findings of Scoville et al. (2003). The stellar population of the inner few arcseconds is compared to that situated up to approximately 0.5 arcminutes out from the position of Sgr A\*, revealing that the extinction does not increase significantly over the entire field of view of the ISAAC instrument (i.e.  $70'' \times 70''$ ). Using the large number of sources (over 500), the  $M$ -band extinction is calculated from the average  $L-M$  colors, resulting in a higher value than that of the “standard” extinction law of Rieke & Lebofsky (1985). The  $L-M$  color is shown to be a useful diagnostic tool in distinguishing hot and cool stars, when more precise methods (e.g. spectroscopy) are not available. The unusual morphology of the bright mid-infrared source IRS 3 is also discussed.

Data from the first VISIR  $N$ - and  $Q$ -band ( $\approx 10$  and 20  $\mu\text{m}$ ) observations (commissioning) of the Galactic center were analysed, resulting in the largest sample of mid-infrared source data for the Galactic center to date (64 sources in total at 8.6  $\mu\text{m}$ ). Many stellar sources such as the Helium-emission-line stars IRS 16NE, IRS 16NW and AF/AHH, and the red giants IRS 12, IRS 14NE and IRS 14SW are detected for the first time in the  $N$ -band. Combining the VISIR data with shorter wavelength data produced an unprecedented number of spectral energy distributions (SEDs) across the whole 1.6 to 19.5  $\mu\text{m}$  range. These can be grouped according to their properties, resulting in the following classification: 1. Northern Arm embedded sources, 2. lower luminosity bow shock sources, 3. cool stars, 4. hot stars, 5. unknown, including IRS 3. Comparing the data at 11.3  $\mu\text{m}$  with that at surrounding wavelengths reveals sources with intrinsic silicate absorption, which is a sign of dust formation. A group of bright mid-infrared sources situated to the east of the Northern Arm source IRS 5 is briefly discussed, however, their nature remains unclear.

Flux densities obtained at the position of Sgr A\* (the supermassive black hole at the center of the Galaxy) complement the results of the 2004 multi-wavelength campaign to monitor the emission from Sgr A\*, providing tighter constraints to theoretical models attempting to explain both the flared state and the interim-quiescent (IQ) state SED of Sgr A\*, especially since it is shown that most of the observed flux density at mid-infrared wavelengths originates from warm dust. A synchrotron self-Compton model with a pure synchrotron component appears to be a promising concept to describe the observed SEDs.

---

# Contents

<b>1</b>	<b>Introduction</b>	<b>1</b>
<b>2</b>	<b>Physical Background</b>	<b>5</b>
2.1	Basic processing of infrared images . . . . .	5
2.1.1	Sky background . . . . .	5
2.1.2	Magnitude Calibration . . . . .	6
2.2	Types of photometry . . . . .	8
2.2.1	Aperture photometry . . . . .	8
2.2.2	PSF-fitting photometry . . . . .	8
2.3	Interstellar dust and extinction . . . . .	11
2.3.1	Interstellar dust . . . . .	11
2.3.2	Interstellar extinction . . . . .	14
2.4	The Synchrotron Self-Compton (SSC) emission mechanism . . . . .	18
<b>3</b>	<b>Observations and data reduction</b>	<b>21</b>
3.1	ISAAC observations . . . . .	21
3.1.1	Data reduction . . . . .	21
3.2	NAOS/CONICA observations . . . . .	22
3.2.1	Data reduction of 2004 images . . . . .	24
3.3	VISIR observations . . . . .	25
3.3.1	Data reduction . . . . .	26
3.4	Additional near-infrared data . . . . .	27
3.5	Observations in other wavelength regimes . . . . .	28
3.5.1	<i>Chandra</i> X-Ray Observations . . . . .	28
3.5.2	SMA Observations . . . . .	29
3.5.3	VLA 7 mm Observations . . . . .	31
3.6	Photometry . . . . .	32
3.6.1	Photometry of ISAAC and 2002 NAOS/CONICA images . . . . .	32
3.6.2	Photometry of VISIR images . . . . .	33
<b>4</b>	<b>Colour analysis of stellar sources in the Galactic Center</b>	<b>35</b>
4.1	Extinction to the Galactic Center . . . . .	35
4.1.1	Comparison of outer and inner field . . . . .	36
4.1.2	<i>M</i> -band extinction . . . . .	36
4.2	Colours of He-emission-line stars and red giants . . . . .	37
4.3	Structure of IRS 3 in the <i>L</i> - and <i>M</i> -band . . . . .	38

---

<b>5</b>	<b>Compact <i>N</i>- and <i>Q</i>-band sources in the Galactic Center</b>	<b>41</b>
5.1	Classification of sources by SED . . . . .	41
5.2	Intrinsic silicate absorption . . . . .	43
5.3	Excess emission at 12.8 $\mu\text{m}$ . . . . .	43
5.4	Unusual sources east of IRS 5 . . . . .	44
<b>6</b>	<b>Flare Activity and midinfrared Properties of Sgr A*</b>	<b>47</b>
6.1	Light Curves of flaring events of Sgr A* . . . . .	47
6.2	Flux Densities and Spectral Indices . . . . .	53
6.3	Constraining the near- and mid-infrared spectrum of Sgr A* . . . . .	54
6.3.1	Contamination by Mid-Infrared Dust Emission . . . . .	55
6.4	Near-infrared and X-Ray Flares . . . . .	57
6.5	Interpretation . . . . .	59
6.5.1	Description and Properties of the SSC Model . . . . .	60
6.5.2	Modeling Results . . . . .	61
<b>A</b>	<b>Long Tables</b>	<b>67</b>
<b>B</b>	<b>Large Figures</b>	<b>79</b>
	<b>Bibliography</b>	<b>96</b>
	<b>Acknowledgements</b>	<b>106</b>



# Chapter 1

## Introduction

The Galactic center has been known as a bright source of near- and mid-infrared radiation since the late 1960s (Becklin & Neugebauer 1968, 1969; Low et al. 1969). The main source of near-infrared radiation is photospheric emission from a dense stellar cluster, and thus a crowded field of point sources, while almost all of the mid-infrared radiation originates from extended gas and dust features, as well as dust emission from the circumstellar regions of a dozen individual sources interacting with the more extended Galactic center interstellar medium.

The Galactic center stellar cluster shows some intriguing characteristics: It is extremely dense, with an unusual observed stellar population consisting mainly (80% of the  $K \leq 14$  stars according to Ott et al. 1999) of late-type red giants, many of which lie on the asymptotic giant branch (AGB), as well as young massive stars with energetic winds. Spectroscopic measurements (e.g. Krabbe et al. 1995; Najarro et al. 1997) allow identification of these two components, the late-type red giants showing strong  $2.3 \mu\text{m}$  CO bandhead absorption and the massive, hot stars with strong winds exhibiting helium and hydrogen emission lines (“He stars”). The emission line stars appear to dominate energetically in the central few arcseconds, accounting for over half the ionizing luminosity of that region. These stars are generally classified as Ofpe/WN9, although some of them might be luminous blue variables (LBV) and a few show characteristics of Wolf-Rayet stars (see e.g. Clénet et al. 2001; Eckart et al. 2004b; Moulataka et al. 2005). Their presence in the immediate vicinity of the Galactic center is currently not fully understood and is sometimes referred to as the “paradox of youth”: On the one hand, these stars are too young to have formed further away from the Galactic center and migrated there within their lifetimes, on the other hand, star formation in the conditions of extreme tidal forces due to the presence of a supermassive black hole and an extremely dense stellar cluster, as well as a strong, energetic radiation field, strong magnetic fields and stellar winds was thought to be impossible. Nevertheless, potentially even younger objects have been discovered that might even hint at very recent or ongoing star formation in the Galactic center (Eckart et al. 2003b, 2004b, 2005; Moulataka et al. 2004a,b). A third, less numerous component of the Galactic center stellar cluster consists of luminous, extended objects with steep, red and featureless ( $K$ -band) spectra and a strong infrared excess, making them the brightest mid-infrared sources. These sources were considered as potential YSO candidates (Clénet et al. 2001; Ott et al. 1999; Krabbe et al. 1995); however, it is now clear that IRS 1W, 2, 5, 10W, and 21 are bow-shock sources, caused by bright stars with strong winds plowing through the ambient gas and dust of the Northern Arm (Tanner et al. 2002, 2003, 2005;

Rigaut et al. 2003; Eckart et al. 2004b; Geballe et al. 2004). Of the fainter mid-infrared sources, IRS 7 (which is very bright at shorter wavelengths) is an M2 supergiant, while most of the others remain enigmatic.

From observations with the European Southern Observatory's Very Large Telescope (ESO VLT), I obtained multi-band ( $H$ ,  $K$ ,  $L$  and  $M$ ) photometry of the Galactic center (first presented in Viehmann et al. 2004), in order to further investigate the properties of the Galactic center stellar cluster. Due to the crowded field, I employed a PSF-fitting algorithm, resulting in color data for a large number of sources (a total of 541 for the  $L$ - and  $M$ -band, see Viehmann et al. 2005b), which allows for improved statistics, resulting in a new  $L$ -band calibration that eliminates anomalous color effects found in other surveys of the Galactic center stellar cluster (e.g. Blum et al. 1996; Clénet et al. 2001; Simons & Becklin 1996). The large field of view ( $70'' \times 70''$ ) of the ISAAC instrument allows me to compare the color properties of the immediate Galactic center cluster population with those of the stellar population further out, i.e. with separations from Sgr A\* of up to approximately half an arcminute. This comparison results in a confirmation of the new extinction values of Scoville et al. (2003). Previous (multi-band) imaging studies of the Galactic center, besides being limited in their field of view to e.g.  $13'' \times 13''$  (Clénet et al. 2001; Davidge et al. 1997), appear to have neglected the  $M$ -band ( $4.66 \mu\text{m}$ ), which shows some interesting properties, since both the emission from warm dust and that from the stellar sources that heat it can be analysed simultaneously. In particular, my analysis of the  $L - M$  colors results in a new  $M$ -band extinction value, as well as revealing new facts on the morphology of the very bright but enigmatic mid-infrared source, IRS 3 (see also Viehmann et al. 2005a,b; and Pott et al. 2005 for further information on IRS 3). More recently, high-quality  $M$ -band spectroscopy of the Galactic center has become available, which should help in understanding the nature of dusty sources located there (Moultaka et al. 2006).

In order to investigate the nature of the bright mid-infrared sources, combined photometry at near- and mid-infrared wavelengths appears to be an ideal tool, since it gives information on both the mid-infrared sources themselves and the stellar sources that could be powering them. Therefore, I combined  $N$ - and  $Q$ -band photometry of the Galactic center, which I obtained from observations with the ESO VLT, with the shorter wavelength data to provide a more complete picture (Viehmann et al. 2006). Previous studies at mid-infrared wavelengths have been severely limited in resolution (e.g. Becklin et al. 1978,  $\sim 2''$ ; Gezari et al. 1985,  $\geq 1''$ ; Stolovy et al. 1996,  $\sim 0.7''$ ); however, since the availability of the VLT Spectrometer and Imager for the Mid-Infrared (VISIR) at the ESO VLT, the Galactic center can be studied in great detail in the  $N$  and  $Q$  bands (i.e. 8-13 and 17-24  $\mu\text{m}$ ), with a resolution of  $0.3''$  to  $0.6''$  (corresponding to the diffraction limit of an 8 m class telescope), provided that the seeing is good enough. This corresponds to a linear resolution of 2500-5000 AU at the distance of 8 kpc to the Galactic center. Even higher resolution observations at mid-infrared wavelengths require the use of interferometric techniques that are still under development, e.g. VLTI (Very Large Telescope Interferometry) or the LBT (Large Binocular Telescope), see e.g. Eckart et al. (2003a, 2006b); Pott et al. (2004).

Over the last decades, evidence has been accumulating that most galaxies contain a super-massive black hole at their center. Since it is only approximately 8 kpc distant from the sun (Reid 1993; Eisenhauer et al. 2003, 2005), the center of our galaxy permits detailed

---

observations of stars that are much less than one parsec distant from the central compact nonthermal radio source Sgr A\*. Investigation of their stellar dynamics has resulted in compelling evidence for a supermassive black hole of  $3.6 \times 10^6 M_{\odot}$  at the position of Sgr A\* (Eckart & Genzel 1996; Eckart et al. 2002; Genzel et al. 1997, 2000; Ghez et al. 1998, 2000, 2003, 2005; Schödel et al. 2002, 2003; Eisenhauer et al. 2003, 2005). Additional evidence for a supermassive black hole at this position is provided by the observation of variable emission originating there, both in X-rays and recently in the near-infrared (Baganoff et al. 2001, 2002, 2003; Eckart et al. 2003c, 2004a; Porquet et al. 2003; Goldwurm et al. 2003; Genzel et al. 2003; Ghez et al. 2004b; Eisenhauer et al. 2005; Bélanger et al. 2005; Yusef-Zadeh et al. 2006).

Simultaneous observations of Sgr A\* across different wavelength regimes provide information on the emission mechanisms responsible for the radiation from the immediate vicinity of the black hole. The first observations of Sgr A\* detecting a weak ( $6 \times 10^{33}$  erg/s) X-ray flare simultaneously in the near-infrared were presented by Eckart et al. (2004a). Variability of Sgr A\* at radio through submillimeter wavelengths has been studied extensively, showing that variations occur on timescales from hours to years (Bower et al. 2002; Herrnstein et al. 2004; Zhao et al. 2003). However, the connection to variability at near-infrared and X-ray wavelengths is not really clear, and some of the radio to submm variability may be due to interstellar scintillation. A probable link between the brightest X-ray flare ever observed and flux density variations at 0.7, 1.3 and 2 cm wavelength on a timescale of less than one day was discovered by Zhao et al. (2004).

Various models have been suggested to explain the spectral energy distribution of the emission from Sgr A\*, most of which rely on radiatively inefficient accretion flow mechanisms or outflows in form of a jet or combinations of the two. Since X-ray and near-infrared flares can occur simultaneously, it appears likely that the same population of electrons causes both the X-ray and the infrared emission, making synchrotron self-Compton models obvious candidates for explaining these flares (Eckart et al. 2004a). This type of model can also be used to describe the *compact* component of the interim-quiescent (IQ) flux density state of Sgr A\*. My analysis of the *N*- and *Q*-band images provides tighter upper limits for the mid-infrared IQ flux density of Sgr A\* than before (Eckart et al. 2006a), since I show that most of the emission detected at the position of Sgr A\* is due to a dust clump. Schödel et al. (2007) argue that Sgr A\* should be easily detectable in the *N*-band in its flaring state, however.



# Chapter 2

## Physical Background

### 2.1 Basic processing of infrared images

#### 2.1.1 Sky background

The sky background is much higher in the infrared regime than e.g. in the visible regime: In the  $V$ -band, the sky brightness is about 22 mag/arcsec<sup>2</sup>, which is comparable to the limiting magnitude of many observations. In contrast, the sky brightness is typically 12 mag/arcsec<sup>2</sup> in the near-infrared  $K$ -band, and about 0 mag/arcsec<sup>2</sup> at 5  $\mu\text{m}$ . Therefore, the astrophysical information to be extracted from infrared observations tends to be a very small fraction of the sky level. This results in much more complex techniques for image acquisition and processing, in order to extract the desired scientific data in the (mid-)infrared regime, compared to the visible.

#### Flat Field

In an imaging observation, the charge collected on a pixel at position  $(i,j)$  on the detector during the integration time  $t_0$  can be written as

$$N_{obs}(i, j) = N_d(i, j, t_0) + N_S F(i, j) + N_O(i, j) F(i, j), \quad (2.1)$$

where  $N_d$  is the dark current,  $N_S$  the sky signal and  $N_O$  the signal from the astrophysical object. The sky signal is assumed to be intrinsically flat; however both the sky and the astronomical signal are modulated by a function  $F(i, j)$ , which consists of illumination functions of the telescope and other relevant instruments, and pixel-to-pixel variations in quantum efficiency and electrical gain of the detector. This function  $F(i, j)$  is called *flat field* and is generally obtained by observing a uniformly illuminated source.

In order to obtain the astronomically relevant information ( $N_O(i, j)$ ) from equation 2.1, it is therefore necessary to determine the dark current and the flat field.

In the case of a blank sky observation, equation 2.1 becomes

$$N_{sky}(i, j) = N_d(i, j, t_0) + N'_S F(i, j). \quad (2.2)$$

Since the two observations did not occur simultaneously, the background  $N'_S$  may differ slightly from  $N_S$ . Subtraction of the sky image yields

$$\frac{N_{obs}(i, j) - N_{sky}(i, j)}{F(i, j)} = N_O(i, j) + (N_S - N'_S). \quad (2.3)$$

Consequently, by subtracting two such observations (astronomical target and blank sky), the necessity to determine the dark current can be circumvented, since it is included in the sky image. The flat function  $F(i, j)$  is divided into the residual sky difference ( $N_S - N'_S$ ), which is almost always much smaller than the sky level itself. Therefore, any errors introduced by flat fielding the sky will be reduced by that ratio.

### Chopping and nodding

When observing isolated pointlike sources (uncrowded field), it is possible to estimate the sky value from the source images themselves, using small telescope offsets (so-called *jittering*), since most of the detector array is measuring sky emission at any given time.

When observing extended objects or dense star clusters (crowded field, e.g. the Galactic center region) however, this is not possible, since one cannot ensure that each pixel is detecting blank sky for a majority of the exposures. The technique employed in such cases is referred to as *chopping*. It consists of taking alternating paired on- and off-target frames with a typical offset of up to 20 arcseconds, in a sequence OSSOOSO... ('O' stands for object, 'S' for sky), typically by moving the secondary mirror of the telescope in phase with the detector readout.

Sky subtracted images (O-S) are produced from these pairs, which ensures good temporal correlation between object and sky values. These sky subtracted images consequently contain both a positive and a negative feature from each source, separated by the chopper throw. Since the optical path on the primary mirror of the telescope varies according to the chopper position, a residual background remains after subtraction of the chopped image pairs. In order to eliminate this remaining background contribution, an additional offset perpendicular to the chopping direction is introduced, which is referred to as *nodding*. This nodding is performed by changing the actual pointing of the telescope, since the timescale for the residual background fluctuations is long compared to the variation timescale of the sky background. In many cases, chopping and nodding are combined in such a way that the first ("on") chopping position of nodding position 1 corresponds to the second ("off") chopping position of nodding position 2, thus maximising the time spent observing the target. However, this specific arrangement is only practical if the source is small enough in relation to the detector array.

Ideally, the exact position of the positive and negative features on the detector varies between each image. Consequently, shifting the sky subtracted images to a common reference point (according to the *positive* features) and combining them by calculating the median will eliminate both the negative features (since they have different positions on each image due to e.g. changing direction of chop) and bad pixels and similar detector artifacts and also cosmic rays (since the position of each observed feature on the detector is varied). However, this method requires a sufficient number of images with different combinations of chopping direction and nodding status to be really effective.

#### 2.1.2 Magnitude Calibration

As in optical astronomy, infrared brightnesses are measured in magnitudes. Infrared apparent magnitudes  $m_1, m_2$  are based on the usual logarithmic scale

$$m_1 - m_2 = -2.5 \log \left( \frac{f_1}{f_2} \right) \quad (2.4)$$

$$\Leftrightarrow \frac{f_1}{f_2} = 10^{-0.4(m_1 - m_2)}, \quad (2.5)$$

where  $f_1$  and  $f_2$  are the corresponding fluxes. This definition derives from the logarithmic sensitivity of the human eye to brightness variations. For the modern magnitude scale, a brightness difference of five magnitudes is thus postulated to equal a factor of about 100 in apparent brightness<sup>1</sup>. In consequence, the magnitude of an object is defined as  $m_\star = -2.5 \log(f_\star/f_0)$ , where  $f_0$  is the monochromatic flux of a magnitude zero star<sup>2</sup>. In order to use this magnitude scale, it is therefore necessary to observe sources of known magnitude (calibration stars).

---

<sup>1</sup>See e.g. Shu (1982); Voigt (1991).

<sup>2</sup> $2.5^5 \approx 97.7 \approx 100$

## 2.2 Types of photometry

The expression *photometry* refers to measuring the brightness or the flux density of the electromagnetic radiation from an astronomical object. This section contains a brief overview of the two types of photometry principally employed during the data reduction relevant to this dissertation.

### 2.2.1 Aperture photometry

The principle of aperture photometry is to calculate the flux density (or magnitude) of a source by integrating the observed flux within a fixed radius from its center and then subtracting the sky background contribution in the vicinity of the source. This technique is not useful in crowded fields.

The optimal aperture size depends on many factors, among others the FWHM and noise levels of the data. An aperture large enough to contain *all the flux* from a star is not possible, since the wings of the PSF (point spread function) extend out very far (*arcminutes* on photographic plates according to King 1971; Kormendy 1973) due to the rapid increase in area. However, a radius exists beyond which the excluded fraction of light becomes constant. Therefore, the most practical aperture can (generally) be determined by comparing results from different apertures and selecting the radius above which the differences become constant. Typically, this occurs at four to five times the FWHM of a stellar image. Nevertheless, further practical constraints may apply, e.g. highly variable backgrounds, local crowding/confusion effects etc., which may necessitate the use of suboptimal aperture sizes.

In the IRAF software used, the sky background contribution which is to be subtracted from the flux is calculated by an annulus situated approximately one third of the radius of the aperture further outwards.

### 2.2.2 PSF-fitting photometry

For crowded fields, PSF-fitting photometry is the method of choice. The basic principle is to fit or define a point-spread-function (PSF), which is then iteratively fit and subtracted from the brightest stars in the image, until no further sources can be found. These procedures are typically performed with software packages such as IRAF/DAOPHOT or STARFINDER (Diolaiti et al. 2000), which is specially designed for reducing images obtained with adaptive optics. PSF-fitting photometry with the IRAF/DAOPHOT software consists of the following steps:

#### Detection of point sources

As a first task, a preliminary list of the point sources in the image and their approximate positions, magnitudes and shape characteristics must be obtained. In order to achieve this, the amplitude of the best-fitting Gaussian of appropriate FWHM (from user input) is calculated for each point in the image by convolving it with an appropriate Gaussian convolution kernel. The task then searches for local maxima in the convolved image with amplitudes that are (a) above the detection threshold (also from user input) and (b) greater than the amplitudes of any neighbors within a region the size of the convolution kernel. Objects with non-stellar properties (i.e. clearly extended or too narrow, e.g. cosmic rays) are rejected. This task is automated in DAOPHOT.



### Aperture photometry

In order to get starting points for the PSF fitting process, “simple” aperture photometry is performed for all the stars detected in the previous step. This results in initial values for sky brightness and magnitudes, which are later used to estimate signal-to-noise ratios and as starting values for the PSF model computation, fitting and the computation of the final sky values. The sky values are calculated from the data in an annulus of pixels around the corresponding source (see above), assuming that fluctuations in the background are mainly due to crowding. This task is also automated.

### Determining the PSF

The most involved and complicated part of photometry with DAOPHOT is the modelling of the PSF. This process requires a list of bright stars, which should be as isolated as possible and well-distributed over the image, as template stars for creating the model PSF. The DAOPHOT software package contains a routine to automatically select a user-selected number of PSF template stars based on brightness, absence of bad data and distance from brighter neighbors, and distance to the edge of the image. However, it remains essential to manually check the brightness profiles of these automatically selected stars and reject those whose PSF is deformed (e.g. by underlying weak neighbors etc.) in order to ensure that a reasonably shaped PSF can be modeled.

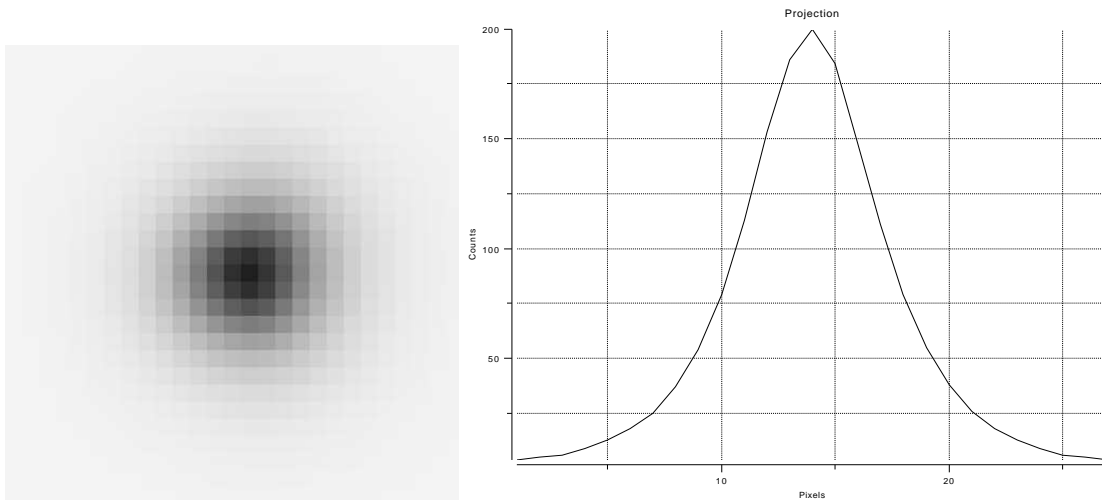


Figure 2.1: PSF and corresponding brightness profile created with IRAF/DAOPHOT for the ISAAC *L*-band image.

The actual PSF modeling process uses non-linear least-squares fitting techniques, weighting the data from the PSF template stars according to their signal-to-noise ratio. Various analytic functions are fitted, and the one yielding the smallest scatter in the fit is finally selected (in most cases, this is an elliptical Lorentz function). A look-up table is additionally created, based on the residuals of each PSF star from the best-fit analytic function, which provides an empirical component to the PSF model. Provision is also made for *saturated* stars, i.e. stars so bright that their profile

is cut off where the detector is saturated. It is obviously impossible to fit a PSF to the full brightness profile of such a star, but the PSF model can be fit to the “wings” of their profile. This is essential if many such stars are to be found in the image.

Subsequently, the neighbors of the PSF template stars are flagged as such to enable iterative “cleaning” of the PSF. This process involves subtracting the PSF template stars *together* with their neighbors, using the calculated PSF model, examining the residuals and rejecting any PSF template stars with unusual residuals or newly-revealed underlying weak neighbors. Then the neighbors *but not the PSF template stars* are subtracted from the original image and the PSF model is recalculated from this neighbor-subtracted image. This sequence is repeated until the PSF stars and their neighbors subtract out cleanly, at which point the PSF model is finalized. An example (for the ISAAC *L*-band image) can be seen in fig. 2.1.

#### Fitting and subtracting stars

Once the PSF model has been calculated, the stars are grouped into associations, fit with the PSF model (using a weighted non-linear least-squares fit) and subtracted in a dynamic process, so that the best fit stars are fitted and subtracted first, which has the advantage of preventing the ‘migration’ of weak stars or noise spikes to the position of brighter stars during the fitting process. New coordinates, sky brightnesses, and magnitudes are derived from the fit, as well as information on errors and the quality of the fit.

#### Photometry of sources missed in the previous run

In a crowded field, new sources will be revealed after fitting and subtraction of all stars detected in the first step (e.g. weak close neighbors). Consequently, the first two steps (detection of point sources and aperture photometry) must be repeated on the image from which the previously detected sources have been subtracted. The resulting initial positions, sky values and magnitudes for the newly-detected sources are then appended to those from previous iterations, and the PSF-fitting and subtraction process is finally repeated (on the original image). These steps are repeated until no new sources are revealed after subtraction.

## 2.3 Interstellar dust and extinction

### 2.3.1 Interstellar dust

The first conclusive evidence for the existence of interstellar dust was obtained through observations of the extinction of distant open stellar clusters in the first half of the twentieth century (Trumpler 1930). Although interstellar dust only represents a relatively small fraction of the total mass of our galaxy, it is nevertheless of fundamental importance for many processes that take place in the interstellar medium. This is due to its very strong interaction with electromagnetic radiation, which is referred to as *interstellar extinction*, its efficient emission of thermal energy, and also its catalytic properties, which are very important for the formation of molecules (even up to complex chemical compounds) in the interstellar medium. In the following sections, the central properties of interstellar dust, as well as the important role it plays for physical and chemical processes in the interstellar medium, are summarily described.

#### Properties

The expression “interstellar dust” generally refers to microscopically sized grains of silicates and carbon compounds, such as graphite or silicon carbide, that occur in interstellar space. These grains are typically between a few nm and a few  $\mu\text{m}$  in size, with polycyclic aromatic hydrocarbons (PAH) and fullerene-like carbon compounds representing the smaller end of the scale. Strictly speaking, these smaller grains are single molecules, however, due to their size and complexity, they exhibit properties typical of solid state particles (e.g. broad absorption bands instead of lines).

More precise information on the structure and chemical composition of the interstellar dust can only be obtained by observing radiation that was either emitted by the dust grains or interacted with the dust. Unfortunately, such observations can merely reveal properties of certain functional groups of the constituent molecules of the dust grains, and not global properties of the dust. Precise statements about the composition and structure of interstellar dust are consequently almost impossible, and models are often based merely on plausibility arguments, leading to a multitude of different models to explain the nature of interstellar dust. Nevertheless, a relatively simple mix of silicate and graphite grains with a size distribution

$$dN(r) \propto r^{-3.5} dr \quad \text{for } 10 \text{ nm} \leq r \leq 300 \text{ nm}$$

can reproduce the interstellar extinction between  $0.1 \mu\text{m}$  and  $1 \mu\text{m}$  extremely accurately (Mathis et al. 1977). Moreover, the validity of this specific extinction law can be extended fairly simply up to the far infrared regime (Draine & Lee 1984).

#### Formation and evolution

In order to form interstellar dust, sufficient quantities of the required precursor materials must be available. Combined with the necessary thermal conditions, this severely constrains the possible sources of interstellar dust. The most important areas of dust formation thus appear to be the photospheres of carbon- or oxygen-rich stars on the asymptotic giant branch (AGB). These highly evolved stellar types most probably represent the main source of interstellar dust (Mathis 1990), since the convective envelope of these stars (which is typical for this evolutionary stage) very effectively transports heavier

elements (e.g. C, O, Si) from the inner regions of the star to the photosphere and thus to the actual region of dust condensation.

Due to their high heavy element content, supernovae are also important sources of interstellar dust, although the relative rarity of such occurrences limits the expected supernova-based dust formation rate.

Other sources of interstellar dust are dwarf stars (Leinert et al. 2000), novae, and binary systems containing Wolf-Rayet stars (Marchenko et al. 1999). Due to their rarity or low dust formation efficiency, however, these objects can be disregarded as sources of significant amounts of interstellar dust.

As far as is understood to date, interstellar dust originates from giant molecules that develop (under suitable conditions) via adsorption and agglomeration, first into micro-clusters and subsequently into macroscopic dust particles (Tsuji et al. 1996). The primary dust sources contribute approximately 0.01 to 0.08  $M_{\odot}$  of dust per year to the interstellar medium of the Milky Way (Gehrz 1989).

A fundamental requirement for dust formation is that the mean time  $t_c$  for the capture of a molecule by an existing cluster (i.e. the precursor stage to a proper dust grain) be shorter than the mean time that a molecule remains in such a cluster before evaporating from it. Only then can dust formation occur, and the type of dust grains resulting from the process can be estimated as follows (Sedlmayr 1989):

1. If the mean time required for an adsorbed molecule to find an unoccupied lattice position in the cluster is shorter than the mean capture time  $t_c$ , each captured molecule will be able to find the best (i.e. lowest energy) unoccupied lattice position before further molecules are adsorbed. In this case, monocrystalline dust grains are to be expected.
2. If the mean time for an adsorbed molecule to find an unoccupied lattice position is  $\geq t_c$ , but the time during which an adsorbed molecule remains at a given position in the cluster is shorter than  $t_c$ , the adsorbed molecule is still mobile enough to relocate a few times, but will (in most cases) not find the lattice position with the lowest possible energy before further molecules are captured by the cluster. In this case, the structure will be locally, but not globally ordered, resulting in irregular, polycrystalline dust grains.
3. If the mean time during which an adsorbed molecule remains at a given position in the cluster is greater than the mean capture time  $t_c$ , the mobility of adsorbed molecules is too low to permit significant relocation before further molecules are adsorbed. In this case, amorphous dust grains are to be expected.

Interstellar dust is mainly destroyed by processes associated with star formation. The typical dust lifetime, i.e. the time between the formation of interstellar dust and its destruction during the formation of new stars can be estimated from the relation between the star formation rate and the gas density in the interstellar medium. In the local interstellar medium this dust lifetime is approximately  $3 \times 10^9$  years (Mathis 1990). Moreover, about 30% of the interstellar medium consists of molecular clouds, the mean lifetime of which is of the order of  $10^8$  years. During its lifetime, each interstellar dust grain will consequently become incorporated in molecular clouds a few times, where its physical and chemical structure will undergo considerable changes due to the temperature, density, chemical environment and possibly high radiation intensity prevalent in such environments. The

dust grains thus generally evolve from relatively small molecules that formed in stellar atmospheres to larger, more compact but also more complex structures.

### **Effect of dust on the interstellar medium**

The effects caused by dust in the interstellar medium can be divided into two groups: On the one hand, the dust interacts with photons, resulting in changes to the properties of the radiation field (besides possible changes to the dust grains themselves), on the other hand, the dust can interact with various other components of the interstellar medium, resulting in changes to the physical and chemical properties of the interstellar medium itself. The first group contains interstellar extinction (described in detail in section 2.3.2), selective polarization of a radiation field, and absorption and reemission of electromagnetic radiation. The second group contains catalysis of chemical reactions at the surface of dust grains (which thus play a very important role in the formation of molecules in the interstellar medium), and photoelectric heating of the interstellar gas. Some of these effects are described below.

**Polarization** If electromagnetic radiation crosses an area of space containing elongated, partially aligned dust grains, selective absorption of the radiation whose electric field vector has a component parallel to the longer axis of the dust grains results in a linear polarization of the radiation field. Circular polarization can be caused by an additional differential phase shift between waves whose field vector is normal or parallel to the axis of the dust grains. Since only interstellar magnetic fields are capable of aligning a significant proportion of dust grains over large areas of space, polarization observations allow to derive the strength and orientation of large-scale interstellar magnetic fields.

**Absorption and reemission of electromagnetic radiation** Interstellar dust grains are heated by the absorption of photons of ultraviolet or visible light. Following Planck's radiation law, the heated dust grains themselves emit continuum radiation at wavelengths between a few and a few hundred  $\mu\text{m}$ , depending on their temperature. (For very cool grains, the emitted radiation may even lie at sub-mm wavelengths.) Besides the properties of the radiation field (e.g. photon energy, flux density), the maximum grain temperature also depends on the optical properties of the dust (reflexivity, emissivity) and the heat capacity of the absorbing dust grains. Large grains ( $\geq 10 \mu\text{m}$ ) with a high heat capacity will thus be heated only slightly, even by the absorption of multiple photons. If the total photon energy absorbed at shorter wavelengths corresponds to the energy emitted in the infrared, such large grains will reach an equilibrium temperature of (typically) a few ten K, resulting in the emission of far-infrared radiation. On the other hand, a single absorbed ultraviolet photon is sufficient to heat a small (approximately 0.5 to 5 nm) dust grain to a temperature of a few hundred K. Such dust grains thus emit continuum radiation that peaks at shorter wavelengths, typically in the mid- or even near-infrared.

**Catalysis of chemical reactions** The low densities and temperatures prevalent in the interstellar medium make direct chemical reactions (that depend on diffusion processes) much too inefficient to account for the column densities of the observable molecules. Interstellar dust grains can play a significant role as a catalyst in the formation of these molecules, which can be quite complex. The formation of molecules can be aided actively, by lowering the activation energy of the relevant chemical reaction, as well as passively

by limiting the degrees of freedom available to the reactants that are bound to the two-dimensional surface of a dust grain. This requires an effective mechanism to separate the newly formed molecules from the surface of the dust grains in order to efficiently produce free molecules in the interstellar medium.

**Photoelectric heating of the ISM** When an ultraviolet photon encounters a dust grain, electrons are freed by the photoelectric effect. Through further encounters, these photoelectrons can deposit part of their kinetic energy in the gas component of the interstellar medium, thus effectively heating the interstellar medium. Which proportion of the absorbed photon energy is converted into kinetic energy of the photoelectron depends on the charge state of the dust grain, since the emitted electron has to overcome the Coulomb potential of the dust grain and thus loses the corresponding part of its kinetic energy. The charge state of a dust grain is mainly determined by two processes: While the photoelectric effect causes the dust grains to accumulate a positive charge, recombination with free electrons reduces this positive charge. The efficiency with which photon energy is converted to electron energy and further to heat will thus decrease with increasing energy density of the ultraviolet radiation, since the equilibrium state of the dust grains is moved to a higher positive charge. The conversion efficiency will increase with increasing electron density, since the higher recombination rate will prevent the dust grains from accumulating high positive charges. Due to the photoelectric effect, interstellar dust is one of the principal components that determine the temperature structure of the interstellar medium.

### 2.3.2 Interstellar extinction

As radiation from an astronomical source travels through the interstellar medium, its intensity is reduced by both scattering and absorption. The observable result of these two effects, i.e. the reduction in intensity of the observed source, is called “interstellar extinction”. Since the efficiency of scattering processes is highly dependant on the relation between a typical dimension of the dust grains (e.g. diameter or circumference) and the wavelength of the radiation involved, the extinction  $A_\lambda$  observed at a certain wavelength is a function of wavelength. This function  $A_\lambda(\lambda)$  is referred to as “extinction law”.

#### Basic equations

The description of extinction through interstellar dust requires the radiative transfer equations. In the simple case that emission by the dust grains and scattering into the solid angular element observed are negligible, the observed intensity as a function of the intrinsic intensity  $I_0$  is given by:

$$I_{\text{obs}} = I_0 e^{-\tau_\lambda}$$

In this case, the optical depth  $\tau_\lambda$  at the wavelength  $\lambda$  depends not only on absorption processes, but also on scattering. Introducing the extinction  $A_\lambda$  by  $\tau_\lambda = 0.4 \ln(10) A_\lambda$ , one obtains

$$I_{\text{obs}} = I_0 \cdot 10^{-0.4A_\lambda}.$$

These equations apply to the “screen case”, in which the emitting and the absorbing medium are strictly separated. In this case, each photon encounters the same column density of absorbing material on its way to the observer, independent of where exactly it was emitted. This model is applicable if the dust column density within the radiation

source is much lower than the column density in the extinguishing region between the source and the observer, and thus intrinsic extinction in the source can be neglected.

If the emitting and the absorbing medium are mixed, however, one must take into account that radiation emitted further from the observer has to cross a higher dust column density than radiation emitted closer to the observer, and thus will be more strongly extinguished. In this “mixed case”, the observed intensity is given by (Thronson et al. 1990)

$$I_{\text{obs}} = I_0 \frac{1 - e^{-\tau_\lambda}}{\tau_\lambda}.$$

In a simple model the interstellar dust grains can be described by small dielectric spheres with radius  $r$  and homogeneous dielectric constant  $\epsilon$ . The extinction coefficient required by the radiative transfer equations can then be expressed by an extinction cross section  $\sigma_e$ :

$$\kappa_\lambda = n(r)\sigma_e = n(r)s_d Q_e$$

Here,  $n(r)$  is the number density of dust particles with radius  $r$ ,  $s_d$  their geometric cross section, and  $Q_e$  the extinction efficiency, which describes the relation between extinction cross section and geometric cross section:  $Q_e = \sigma_e/s_d$ . Introducing the scattering efficiency  $Q_s = \sigma_s/s_d$  and the absorption efficiency  $Q_a = \sigma_a/s_d$ , one obtains  $Q_e = Q_s + Q_a$ . In the case that the grain size is much smaller than the wavelength (i.e.  $r \ll \lambda$ , valid for wavelengths longer than far ultraviolet radiation), the efficiencies are given by (Spitzer 1978):

$$Q_s = \frac{8}{3} \left( \frac{2\pi r}{\lambda} \right)^4 \left| \frac{\epsilon - 1}{\epsilon + 2} \right|^2$$

and

$$Q_a = -4 \frac{2\pi r}{\lambda} \Im \left( \frac{\epsilon - 1}{\epsilon + 2} \right),$$

where  $\Im(\text{argument})$  is the imaginary part of the argument. It becomes clear that both the scattering efficiency and the absorption efficiency, and thus also the optical depth  $\tau_\lambda$  and the extinction  $A_\lambda$  decrease with increasing wavelength.

### Observational properties

Due to the inhomogeneous distribution of dust in the interstellar medium, each observed astronomical source in general requires its own extinction law. This is especially true in the ultraviolet and visible spectral regions, where the extinction law is highly dependent on the specific properties of the interstellar medium along the line of sight to the source. In the infrared, however, the extinction law appears to be largely independent of the specific line of sight. Specifically at wavelengths between 0.7 and 7  $\mu\text{m}$  the extinction law is virtually independent of the line of sight and can be described by a simple power law (Draine 1989):

$$\frac{A_\lambda}{E(J - K)} = 2.4 \cdot \lambda^{-1.75},$$

where  $E(J - K)$  is the corresponding infrared color excess. Actual observations reveal deviations from this power law, the most prominent one being an increased extinction at 3.1  $\mu\text{m}$ . The increased absorption at this wavelength is probably due to water ice mantles coating the dust grains. In the mid-infrared region between 8 and 30  $\mu\text{m}$ , the interstellar extinction law is completely dominated by broad absorption bands at 9.7 and 18  $\mu\text{m}$ .

They are caused by amorphous silicates, which constitute an important component of the interstellar dust in many interstellar regions. For most astronomical sources, the extinction at wavelengths longer than  $30 \mu\text{m}$  is too low to be measured directly. Nevertheless, in this wavelength region it is possible to estimate the intrinsic emission of an astronomical source using models for the thermal emission of interstellar dust. The comparison with the observed emission of the source then allows the deduction of the interstellar extinction in the far-infrared. However, the model calculations are highly dependent on the dust temperature, which is not sufficiently well known in general, thus permitting only relatively uncertain estimates of the extinction.

### Extinction to the Galactic Center

Due to the position of the sun close to the galactic plane, the line of sight to the Galactic center passes through regions of high dust column density, resulting in a very high visual extinction, which has been quoted as high as 31 magnitudes (average over Galactic center region, see e.g. Rieke et al. 1989). More recent results indicate, however, that the extinction to the central region containing the Northern Arm of the “mini-spiral” and Sgr A\* is not quite so high:  $\approx 25$  magnitudes (Scoville et al. 2003). This lower value is confirmed by the results of the analysis in section 4.1. The higher extinction values of 35 to 50 magnitudes reported by Scoville et al. (2003) apply to the surrounding circumnuclear molecular ring. This ring, which surrounds the Galactic center at a radius of 2-4 kpc, contains the greater part of the molecular gas (CO) in the line of sight to the Galactic center, and thus also the greater part of the extinguishing interstellar dust (Sanders et al. 1985). Since it has a sharp inner edge (e.g. Latvakoski et al. 1999), and the dust column density in the HII

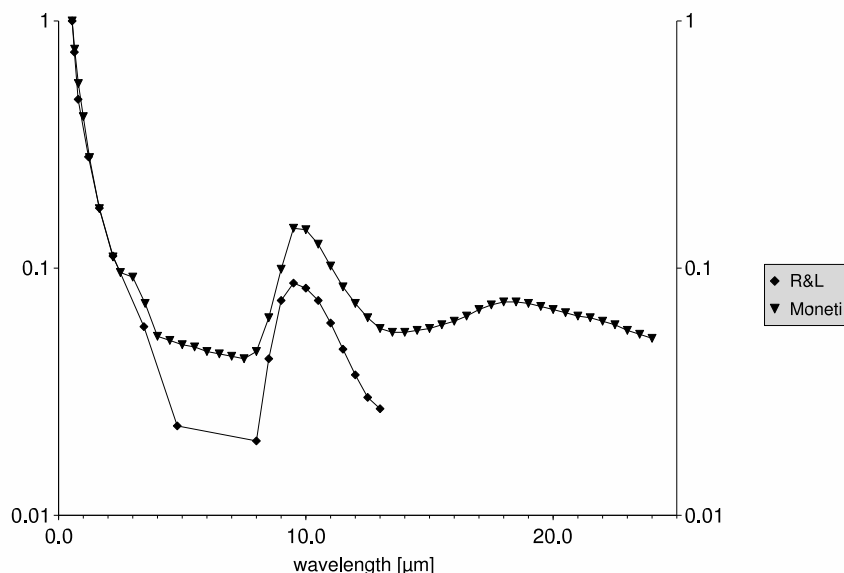


Figure 2.2: Extinction laws ( $A_\lambda/A_V$ ) as given by Rieke & Lebofsky (1985) (RL) and Moneti et al. (2001). See also table A.4.



region surrounding Sgr A\* is much lower (Becklin et al. 1982), the Galactic center appears to be a typical example of “screen case” extinction (see beginning of this section 2.3.2).

The extinction law of Rieke & Lebofsky (1985) (see table A.4 and fig. 2.2) is based on infrared photometry of sources identified as late-type stars in or near the Galactic center, and has been regarded as a “standard” extinction law for this region. From theoretical calculations and various observational results, Draine (1989) derived  $A_\lambda \propto \lambda^{-1.75}$  for wavelengths between 0.7 and 7  $\mu\text{m}$  and standard graphite-silicate mixes as extinguishing material. However, the broad minimum in the extinction between 4 and 8  $\mu\text{m}$  predicted by these extinction laws apparently does not apply to the Galactic center (see Rieke et al. 1989; Lutz et al. 1996; Lutz 1999, and section 4.1.2). These more recent findings are incorporated into the extinction law given by Moneti et al. (2001), which is also shown in table A.4 and fig. 2.2. The increased extinction at approximately 3  $\mu\text{m}$  is attributed to an ice feature at 3.1  $\mu\text{m}$  (Draine 1989) or 2.9  $\mu\text{m}$  and an amorphous carbon feature at 3.4  $\mu\text{m}$  (Moneti et al. 2001), but it remains unclear what causes increased extinction in e.g. the *M*-band, as described in section 4.1.2.

## 2.4 The Synchrotron Self-Compton (SSC) emission mechanism

Synchrotron radiation occurs when ultrarelativistic charged particles are accelerated (in curved paths or orbits) through a magnetic field. Such radiation was first detected astronomically in a jet emitted by M87 (Burbidge 1956).

Synchrotron radiation plays a significant role in explaining the variable emission from supermassive black holes, such as Sgr A\* at the center of the Milky Way. In this context, the synchrotron self-compton mechanism is important. It involves synchrotron emission (e.g. at submillimeter wavelengths) together with a high-energy component (e.g. X-rays) which is caused by Compton scattering of the low-energy photons with the emitting population of electrons, thus creating high-energy photons.

The basic formulae to describe such processes are derived by Gould (1979), but they are not practical when describing astronomical observations.

For such a case, assume a compact, spherical synchrotron source with a magnetic field that is uniform in strength but disordered in direction, together with an isotropic, power-law distribution of electrons

$$N(E) = \frac{N_0}{E^{2\alpha+1}} \quad \text{for} \quad \gamma_1 mc^2 < E < \gamma_2 mc^2.$$

If  $\Theta$  is the angular diameter of the source (in mas),  $z$  the redshift,  $\alpha$  the spectral index of the source,  $S_m$  and  $\nu_m$  the flux density (in Jy) and frequency (in GHz) at the synchrotron self-absorption turnover, and the equivalent Doppler factor

$$\delta = \frac{\sqrt{1-\beta^2}}{1-\beta \cos \phi}$$

describes possible relativistic bulk motion of the source, with  $\phi$  the angle of the velocity vector to the line of sight, we have

$$B = b(\alpha) \frac{\Theta^4 \nu_m^5}{S_m^2} \frac{\delta}{1+z}$$

in units of  $10^5$  gauss, and

$$N_0 = \frac{n(\alpha)}{D} \frac{S_m^{2(\alpha+3)}}{\Theta^{4\alpha+7} \nu_m^{4\alpha+5}} \frac{(1+z)^{2(\alpha+3)}}{\delta^{2(\alpha+2)}}.$$

From this, the first-order Compton flux density can be derived, using equations from Gould (1979). It is given by

$$S_\nu \approx d(\alpha) \ln(\nu_2/\nu_m) \frac{S_m^{2(\alpha+2)}}{\Theta^{2(2\alpha+3)} \nu_m^{3\alpha+5}} \frac{1}{E^\alpha} [(1+z)/\delta]^{2(\alpha+2)},$$

with  $S_\nu$  in  $\mu\text{Jy}$  and  $E$  in keV. The quantities  $b(\alpha)$ ,  $n(\alpha)$  and  $d(\alpha)$  are dimensionless parameters of the spectral index  $\alpha$  and are plotted for spectral indices between 0.25 and 1.00 in fig. 2.3. The upper frequency cutoff to the synchrotron spectrum is given by  $\nu_2 = 2.8 \cdot 10^6 B \gamma_2^2$ .

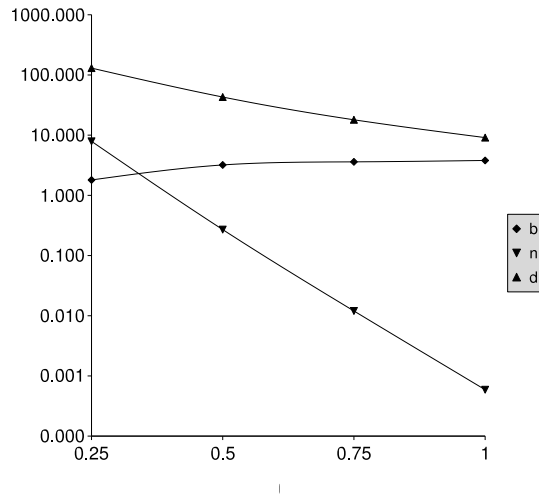


Figure 2.3: Dimensionless parameters of the spectral index  $\alpha$  as given by Marscher (1983).

The applicability limits of this formula for the Compton flux density are

$$5.5 \cdot 10^{-9} \gamma_1^2 \nu_m \leq E \leq 0.2 \frac{1}{b(\alpha)} \frac{\nu_2^2 S_m^2}{\Theta^4 \nu_m^5} [(1+z)/\delta]^2$$

(see also Marscher 1983).



## Chapter 3

# Observations and data reduction

### 3.1 ISAAC observations

ISAAC is the ESO *Imaging Spectrometer And Array Camera*, a combined infrared (1-5  $\mu\text{m}$ ) imager and spectrograph located at the Nasmyth B focus of UT1 (Unit Telescope 1, Antu) of the ESO VLT. It operates with two detectors, a Hawaii Rockwell array for shorter wavelengths (1-2.5  $\mu\text{m}$ ) and an InSb Aladdin array from Santa Barbara Research Center (mainly for longer wavelengths, i.e. 3-5  $\mu\text{m}$ ). Both detectors provide  $1024 \times 1024$  elements with pixel scales of 0.148''/pixel, as well as 0.071''/pixel for the Aladdin array, resulting in fields of view of  $151'' \times 151''$  and  $73'' \times 73''$ , respectively (Cuby et al. 2002). Background subtraction is performed via chopping and nodding.

On May 23rd – 30th 2002, *L*- and *M*-band (3.78  $\mu\text{m}$  and 4.66  $\mu\text{m}$ ) imaging observations of the Galactic center were obtained with ISAAC as part of a joint infrared/X-ray monitoring program of Sgr A\* (Eckart et al. 2003c; Baganoff et al. 2003). The seeing-limited images were taken in ISAAC's higher resolution mode (0.071''/pixel, field of view  $73'' \times 73''$ ). Seeing conditions varied considerably during the campaign, resulting in angular resolutions between 0.4'' and 1.2''. The observations were made in batches of 25 to 40 pairs of frames (with chopping and nodding), with an integration time of 0.99 s per frame, each batch covering approximately 35 minutes in one band.

#### 3.1.1 Data reduction

All image processing was performed using routines from the IRAF software package. The data reduction procedures employed were standard: After flat field correction, the paired on- and off-target frames were subtracted from each other, resulting in sky subtracted images containing positive and negative features for each source. Subsequently, the sky subtracted images from each batch were shifted to a common reference frame (corresponding to the positive features) using a cross-correlation algorithm and then combined by calculating the median, which also effectively removed cosmic rays and bad pixels. The final images were then created by coaddition of the median images with the best effective seeing, i.e. better than 0.6'', resulting in total integration times of 229.7 s for the *L*-band image and 162.4 s for the *M*-band image. The final images are shown in Figs. B.1 and B.2. Finally, PSF-fitting photometry was performed on the final images using the IRAF/DAOPHOT software package (see sections 2.2 and 3.6).

### 3.2 NAOS/CONICA observations

NAOS/CONICA consists of the *Nasmyth Adaptive Optics System* and the *High-Resolution Near IR Camera*. They are located at the Nasmyth B focus of UT4 (Unit Telescope 4, Yepun) of the ESO VLT.

NAOS provides a turbulence-compensated beam to CONICA by means of a tip-tilt plane mirror which compensates for overall wavefront tip and tilt (the largest disturbances created by atmospheric turbulence), and a deformable mirror which compensates for higher order aberrations, including static aberrations caused by the instruments (NAOS and CONICA) themselves. These compensators are controlled by one of the two wavefront sensors that NAOS provides, a visible and a near-infrared one, both of which consist of Shack-Hartmann sensors. The active wavefront sensor receives light that is split from the optical path to CONICA by a dichroic, and is locked on a reference star (natural guide star, preferably bright and isolated) situated within  $55''$  of the intended target of the observation.

CONICA is an infrared ( $1\text{--}5\ \mu\text{m}$ ) imager and spectrograph. Its detector is an InSb Aladdin 3 array from Santa Barbara Research Center (since May 2004, previously Aladdin 2 array) with  $1024 \times 1024$  effective pixels. Various pixel scales ranging from  $0.055''/\text{pixel}$  to  $0.0132''/\text{pixel}$  are available, resulting in fields of view between  $56'' \times 56''$  and  $14'' \times 14''$  (see e.g. Ageorges et al. 2005). Background subtraction is performed via jittering, or alternatively chopping and nodding for thermal infrared observations (at wavelengths greater than  $3\ \mu\text{m}$ ).

#### Commissioning observations of the Galactic Center

On 30 August 2002, during the science verification phase of the commissioning and observatory preparation of NAOS/CONICA,  $H$ - and  $K_s$ -band ( $1.6\ \mu\text{m}$  and  $2.1\ \mu\text{m}$ , respectively) images of the Galactic center were obtained, with a FWHM of 43 and 56 milliarcseconds, and a pixel scale of  $0.0132''/\text{pixel}$  (Schödel et al. 2002, 2003). In these observations, the infrared wavefront sensor of NAOS was used to lock the adaptive optics loop on the near-infrared bright (K-band magnitude  $\approx 6.5$ ) supergiant IRS 7, located about  $5.6''$  north of Sgr A\*. The total integration times were 1500 s and 1200 s, respectively. Since the  $K - K_s$  color difference is an order of magnitude smaller than the photometric accuracy that is reached, the distinction between  $K$  ( $2.2\ \mu\text{m}$ ) and  $K_s$  will be ignored in this dissertation. Since the purpose of the NAOS/CONICA images in this context is to gain additional color information for analysing the seeing-limited ISAAC  $L$ - and  $M$ -band images, the pixel scale of the NAOS/CONICA images was reduced to the corresponding  $0.071''/\text{pixel}$  via re-binning. The resulting images are shown in fig. B.3.

#### Monitoring of Sgr A\* in 2004

Near-infrared observations of the Galactic center were carried out with NAOS/CONICA during the nights between 05 July and 08 July 2004. As in the commissioning observations, the infrared wavefront sensor was used to lock the adaptive optics loop on IRS 7 as guide star. The start and stop times of the near-infrared observations are listed in table 3.1. Details on integration times and approximate seeing during the observations are listed in table 3.2. As can be seen, the atmospheric conditions (and consequently the AO correction) were fairly variable during some of the observation blocks.

Telescope Observing ID	Instrument	Energy/ $\lambda$	UT Start Time	UT Stop Time
<i>Chandra</i>	ACIS-I	2-8 keV	05 JUL 2004 22:38:26	06 JUL 2004 12:56:59
<i>Chandra</i>	ACIS-I	2-8 keV	06 JUL 2004 22:35:12	07 JUL 2004 12:53:45
1 VLT UT 4	NAOS/CONICA	1.7 $\mu\text{m}$	06 JUL 2004 02:47:11	06 JUL 2004 03:26:48
2 VLT UT 4	NAOS/CONICA	2.2 $\mu\text{m}$	06 JUL 2004 03:48:53	06 JUL 2004 07:05:59
3 VLT UT 4	NAOS/CONICA	3.8 $\mu\text{m}$	06 JUL 2004 07:17:10	06 JUL 2004 08:42:52
4 VLT UT 4	NAOS/CONICA	2.2 $\mu\text{m}$	06 JUL 2004 23:19:39	07 JUL 2004 04:16:37
5 VLT UT 4	NAOS/CONICA	3.8 $\mu\text{m}$	07 JUL 2004 23:54:48	08 JUL 2004 00:45:44
6 VLT UT 4	NAOS/CONICA	2.2 $\mu\text{m}$	08 JUL 2004 00:53:32	08 JUL 2004 06:53:46
SMA-A	340 Pol	890 $\mu\text{m}$	05 JUL 2004 06:59:30	05 JUL 2004 12:24:18
SMA-B	340 Pol	890 $\mu\text{m}$	06 JUL 2004 06:03:17	06 JUL 2004 12:26:48
SMA-C	340 Pol	890 $\mu\text{m}$	07 JUL 2004 05:47:12	07 JUL 2004 12:28:58
VLA-A	...	7 mm	06 JUL 2004 04:41:24	06 JUL 2004 09:09:06
VLA-B	...	7 mm	07 JUL 2004 04:37:46	07 JUL 2004 09:02:26
VLA-C	...	7 mm	08 JUL 2004 04:39:16	08 JUL 2004 08:58:27

Table 3.1: Observation log of July 2004 Sgr A\* observations.

Observations of a dark cloud – a region practically devoid of stars – a few arcminutes to the north-west of Sgr A\* were interspersed with the observations at 1.7  $\mu\text{m}$  and 2.2  $\mu\text{m}$  in order to obtain sky measurements.

All observations were dithered in order to cover a larger area of the Galactic center by mosaic imaging. In case of the observations at 3.8  $\mu\text{m}$ , the sky background was extracted from the median of stacks of dithered exposures. Here the procedure is different from that at 1.7  $\mu\text{m}$  and 2.2  $\mu\text{m}$  since thermal emission from dust as well as a brighter and variable sky has to be taken into account.

Observing ID	central wavelength	DIT	NDIT	N	pixel scale	seeing
1	1.7 $\mu\text{m}$	15 s	2	50	0.013''	$\sim 1.1''$
2	2.2 $\mu\text{m}$	15 s	2	217	0.027''	$\sim 1.0\text{-}1.5''$
3	3.8 $\mu\text{m}$	0.2 s	150	100	0.027''	$\sim 1.3\text{-}1.8''$
4	2.2 $\mu\text{m}$	30 s	1	330	0.027''	$\sim 1.0\text{-}1.8''$
5	3.8 $\mu\text{m}$	0.2 s	150	60	0.027''	$\sim 0.7''$
6	2.2 $\mu\text{m}$	30 s	1	391	0.027''	$\sim 0.7''$

Table 3.2: Details of July 2004 near-infrared observations. ‘‘Observing ID’’ refers to the number of the data set in table 3.1. DIT is the detector integration time in seconds, NDIT is the number of exposures of integration time DIT that were averaged on-line by the instrument, while N is the number of images taken. The total integration time amounts to  $\text{DIT} \times \text{NDIT} \times \text{N}$ . The seeing given here is the value measured by the *Differential Image Motion Monitor* (DIMM) on Paranal at visible wavelengths. It provides a rough impression of the atmospheric conditions during the observations.

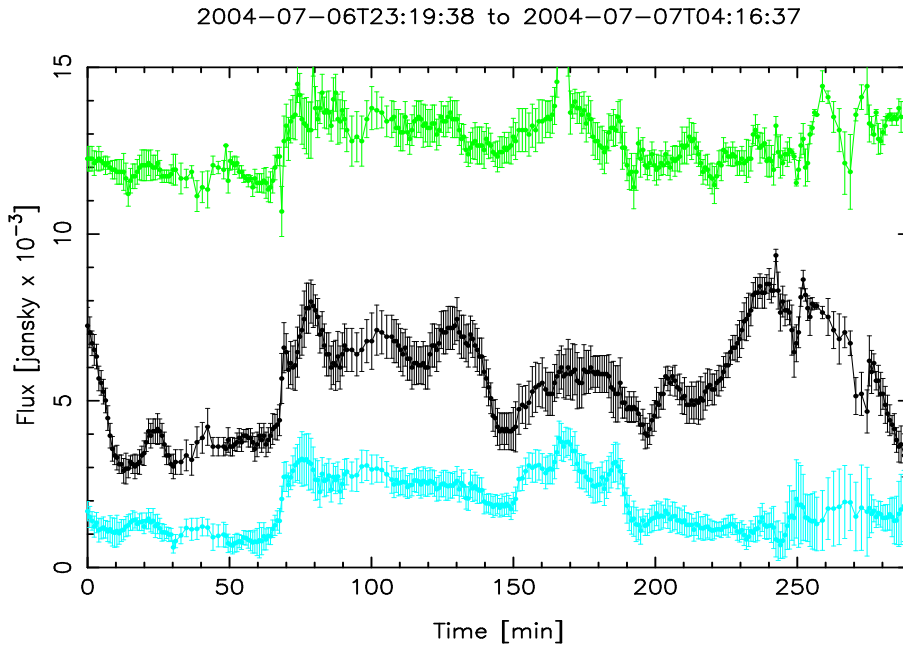


Figure 3.1: Light curve of the  $K$ -band observations from July 07 (see fig. B.11). The plot shows the light curves of S1 (top), Sgr A\* (middle), and the background flux (bottom).

### 3.2.1 Data reduction of 2004 images

All exposures were sky subtracted, flat-fielded, and corrected for dead or bad pixels. In order to enhance the signal-to-noise ratio of the imaging data, median images were created, comprising 9 single exposures each. Subsequently, PSFs were extracted from these images with *StarFinder* (Diolaiti et al. 2000). The images were deconvolved with the Lucy-Richardson (LR) and linear Wiener filter (LIN) algorithms. Beam restoration was carried out with a Gaussian beam of FWHM corresponding to the respective wavelength. Therefore the final resolution at 1.7, 2.2, and 3.8  $\mu\text{m}$  is 46, 60, and 104 milliarcseconds (mas), respectively.

The flux densities of the sources were measured by aperture photometry with circular apertures of 52 mas radius and corrected for extinction, using  $A_H = 4.3$ ,  $A_K = 2.8$ , and  $A_L = 1.8$ . Calibration of the photometry and astrometry was done with the help of the known fluxes and positions of 9 sources within 1.6" of Sgr A\*. Uncertainties were obtained by comparing the results of the photometry on the LR and LIN deconvolved images. The background flux was obtained by averaging the measurements at five random locations in a field about 0.6" west of Sgr A\* that is free of obvious stellar sources. The average positions and fluxes of Sgr A\* obtained from the near-infrared observations are listed in tab. 3.3. Fig. B.11 shows a plot of the flux versus time for Sgr A\*, S1, and the background. As can be seen, the background is fairly variable. These background fluctuations are present in the light curves of Sgr A\* and S1 as well, as can be seen in the figure. It is therefore reasonable to subtract the background flux from the light curves. The result is shown in fig. 3.1. The source S1 now shows an almost constant flux density as expected.



Observing ID	$\lambda$	RA ["]	DEC ["]	Flux density [mJy]
1	1.7 $\mu\text{m}$	0.004 $\pm$ 0.004	0.009 $\pm$ 0.005	$\leq$ 3.1
2	2.2 $\mu\text{m}$	0.011 $\pm$ 0.007	0.012 $\pm$ 0.013	$\leq$ 3.9
3	3.8 $\mu\text{m}$	0.017 $\pm$ 0.009	-0.017 $\pm$ 0.004	$\leq$ 34
4	2.2 $\mu\text{m}$	0.004 $\pm$ 0.003	0.005 $\pm$ 0.004	5.2 $\pm$ 1.8
5	3.8 $\mu\text{m}$	-0.022 $\pm$ 0.004	-0.009 $\pm$ 0.005	17 $\pm$ 4
6	2.2 $\mu\text{m}$	0.003 $\pm$ 0.004	0.002 $\pm$ 0.003	2.8 $\pm$ 1.1

Table 3.3: Average position and flux density of Sgr A\* as obtained from the near-infrared data. The first column lists the observation ID (see table 3.1), third and fourth columns the position of Sgr A\* (average of all exposures) relative to its nominal position (Eisenhauer et al. 2003), and the fifth column the measured overall flux density and standard deviation of Sgr A\* during the particular observing session. The data were obtained by aperture measurements with a  $\sim$ 50 mas radius aperture on the nominal position of Sgr A\* and are corrected for extinction (see text). For data set 2, the average values are extracted from the first 120 exposures only, because the exposures obtained later were of very low quality.

### 3.3 VISIR observations

VISIR is the *VLT mid-Infrared Spectrometer and Imager for the infraRed*, which is located at the Cassegrain focus of UT3 (Unit Telescope 3, Melipal) of the ESO VLT. It operates in the mid-infrared *N*- and *Q*-bands, i.e. at wavelengths of 8 to 13  $\mu\text{m}$  and 17 to 24  $\mu\text{m}$ . The detectors are two 256 $\times$ 256 pixel SiAs Blocked Impurity Band (BIB) arrays from DRS Technologies. The pixel scales provided are 0.075"/pixel and 0.127"/pixel, resulting in fields of view of 19.2"  $\times$  19.2" and 32.5"  $\times$  32.5", respectively. Background subtraction is performed via chopping and nodding.

During the commissioning of the VISIR mid-infrared imager/spectrograph at the ESO VLT (UT3, Melipal), the Galactic center was observed on May 7th – 11th 2004. Many narrowband filters spanning the whole *N*-band (8-13  $\mu\text{m}$ ), as well as the 18.7  $\mu\text{m}$  and 19.5  $\mu\text{m}$  ( $\Delta\lambda = 0.88$  and 0.40  $\mu\text{m}$ ) filters in the *Q*-band were used. In this paper concentrates on the 8.6, 11.3, and 12.8  $\mu\text{m}$  ( $\Delta\lambda = 0.42$ , 0.59, and 0.21  $\mu\text{m}$ ) filters in the *N*-band, since the highest number of images (and thus the longest integration times) were produced with these filters. The images cover a field of view of approximately 32"  $\times$  32" at a pixel scale of 0.127" per pixel (see e.g. Lagage et al. 2003 for further details on VISIR). The resulting angular resolution (due to seeing and the diffraction limit) varies between 0.3" at 8.6  $\mu\text{m}$  and approximately 0.6" in the *Q*-band, as measured from compact sources on the frames (e.g. IRS 7). Each of the images supplied by the VISIR pipeline consists of the average of (typically) seven chopped (chopper frequency 0.25 Hz, amplitude 12.5", position angle 0 $^\circ$ ) and flat-fielded exposures, with a typical integration time of 14 s per averaged image.

### 3.3.1 Data reduction

The chopped and flat-fielded exposures supplied by the pipeline were selected based on image quality (FWHM and signal-to-noise ratio) and coadded, resulting in total integration times of 168, 182, 140, 70 and 140 seconds at 8.6, 11.3, 12.8, 18.7 and 19.5  $\mu\text{m}$ , respectively. The final 19.5  $\mu\text{m}$  image is shown in fig. B.7, while a three-color composite of the  $N$ -band images is shown in fig. B.6.

ID	date	time	flux density [mJy]	seeing FWHM [pixel]
001	2004-05-08	09:07:47	25.2	0.27
002	2004-05-08	09:09:52	23.2	0.27
003	2004-05-08	09:10:27	24.2	0.27
004	2004-05-08	09:12:35	23.3	0.25
005	2004-05-08	09:13:10	24.8	0.25
006	2004-05-08	09:21:12	21.6	0.27
007	2004-05-08	09:23:15	24.5	0.28
008	2004-05-08	09:23:51	24.2	0.23
009	2004-05-08	09:25:56	24.5	0.25
010	2004-05-08	09:46:54	25.6	0.24
011	2004-05-08	09:51:53	31.4	0.28
012	2004-05-08	09:53:57	32.0	0.29
013	2004-05-08	09:54:34	20.6	0.27
014	2004-05-08	09:56:40	32.3	0.30
015	2004-05-08	09:57:15	27.3	0.27
016	2004-05-09	08:16:59	30.8	0.33
017	2004-05-09	08:19:08	47.4	0.43
018	2004-05-09	08:19:46	46.4	0.37
019	2004-05-09	08:21:52	56.9	0.38
020	2004-05-09	08:22:26	56.7	0.38
021	2004-05-10	05:59:04	23.7	0.38

Table 3.4: 8.6  $\mu\text{m}$  flux densities at the position of Sgr A\*. The flux densities are dereddened using  $A_{8.6\mu\text{m}}=1.75$ . The calibration is described in the text.

Flux densities at the position of Sgr A\* and the S-cluster (combined, due to the resolution of 0.3-0.4") were extracted from these images, using IRS 21 as a flux calibrator. Tanner et al. (2002) report 8.8  $\mu\text{m}$  flux densities of 1.34 Jy (1" aperture, background subtracted), 3.21 Jy (1" aperture, non-background-subtracted) and 3.6 Jy (2" aperture, non-subtracted) for this source. After adjusting for the different wavelength used (both wavelengths lie on the flank of the 9.7  $\mu\text{m}$  silicate absorption feature, c.f. Lutz et al. 1996), a background-subtracted flux density of 5.11 Jy for IRS 21 in a 2" aperture is obtained. These flux densities also agree well with the 8.7  $\mu\text{m}$  flux densities for the bright IRS sources measured by Stolovy et al. (1996), who found 5.6 Jy for IRS 21 (2" aperture, background not subtracted). Recent results (Scoville et al. 2003; Viehmann et al. 2005a) suggest a

lower extinction than the traditionally used  $A_V=27-30$  magnitudes towards the Galactic center. Consequently,  $A_V=25$  magnitudes and thus  $A_{8.6\mu\text{m}}=1.75$  was adopted, following the extinction law of Lutz et al. (1996), which results in an extinction-corrected flux density of 4.56 Jy for IRS 21 at 8.6  $\mu\text{m}$  in a 1" aperture, which we used for calibration. The final flux density values at the position of SgrA\* were obtained in a 1" diameter aperture. As reference sources to determine the relative positioning between the near- and mid-infrared frames, the bright and compact sources IRS 3, 7, 21, 10W and in addition at 8.6 $\mu\text{m}$  wavelength IRS 9, 6E, and 29 were used. In this way, a final positional uncertainty of  $\pm 0.2''$  was obtained. At both wavelengths the flux density is dominated by an extended source centered about  $0.2''-0.3''$  west of SgrA\*. This source was also noted by Stolovy et al. (1996).

In table 3.4 the flux densities obtained for the available 0.3-0.4" angular resolution VISIR data are listed. At 8.6 $\mu\text{m}$  wavelength the mean flux density is  $30\pm 10$  mJy ( $1\sigma$ ), with a tendency for larger flux density values during times of poorer seeing. The main differences are between data sets taken on different days and there are no signs of a strong (i.e. several  $\sigma$ ) deviation. Therefore, a dereddened flux density at 8.6 $\mu\text{m}$  wavelength of 50 mJy is adopted as a safe upper limit. A flux density of  $320\pm 80$  mJy in a 1" diameter aperture at the position of SgrA\* is obtained at 19.5 $\mu\text{m}$ , following the same calibration procedure and assuming  $A_V=25$ ,  $A_{8.6\mu\text{m}}=1.75$  and using 20.8 $\mu\text{m}$  flux densities for IRS 21 from Tanner et al. (2002).

### 3.4 Additional near-infrared data

The field of view of the NAOS/CONICA images (approximately  $17.8'' \times 17.8''$ ) is much smaller than the ISAAC field of view. In order to check the properties of sources outside this inner region, additional *H*- and *K*-band images were analysed.

#### ISAAC *K*-band image

During the 1999 ISAAC spectroscopy campaign (Eckart et al. 1999), a *K*-band image of the Galactic center was obtained, using ISAAC's lower resolution mode (pixel scale 0.148", field of view approximately  $150'' \times 150''$ , see Cuby et al. 2002).

#### Gemini data

For *H*-band, publicly released Gemini data from the 2000 Galactic center Demonstration Science Data Set (using the Quirc camera and the Hokupa'a adaptive optics system, see Cotera & Rigaut 2001) was also used.

In order to limit the amount of work required, photometry on these datasets was performed only for the brighter sources in the *L*-band image ( $m_L < 9.5$ ) and an exemplary selection of approximately 15 fainter sources in order to verify that the faint stars do not show systematically different color properties than the bright stars. The images were calibrated relative to the NAOS/CONICA data.

## 3.5 Observations in other wavelength regimes

### 3.5.1 *Chandra* X-Ray Observations

In parallel to the 2004 near-infrared observations, Sgr A\* was observed with *Chandra* using the imaging array of the Advanced CCD Imaging Spectrometer (ACIS-I; Weisskopf et al. 2002) for two blocks of approximately 50 ks on 05 to 07 July 2004 (UT). The start and stop times are listed in table 3.1. The instrument was operated in timed exposure mode with detectors I0 - 3 turned on. The time between CCD frames was 3.141 s. The event data were telemetered in faint format. The background was stable throughout the observation, and there were no gaps in the telemetry.

The data was reduced and analysed using the CIAO v2.3<sup>1</sup> software with *Chandra* CALDB v2.22<sup>2</sup>. Following Baganoff et al. (2003), the level 1 data was reprocessed in order to remove the 0.25" randomization of event positions applied during standard pipeline processing and to retain events flagged as possible cosmic-ray after-glows, since the strong diffuse emission in the Galactic center causes the algorithm to flag a significant fraction of genuine X-rays. The data were filtered on the standard ASCA grades.

The X-ray and optical positions of three Tycho-2 sources were correlated (Høg et al. 2000) to register the ACIS field on the Hipparcos coordinate frame to an accuracy of 0.10" (on axis); then the position of the X-ray source at Sgr A\* was measured. The X-ray position [ $\alpha_{J2000.0} = 17^{\text{h}}45^{\text{m}}40.030^{\text{s}}$ ,  $\delta_{J2000.0} = -29^{\circ}00'28.23''$ ] is consistent with the radio position of Sgr A\* (Reid et al. 1999) to within  $0.18'' \pm 0.18''$  ( $1\sigma$ ).

Counts were extracted within radii of 0.5", 1.0", and 1.5" around Sgr A\* in the 2–8 keV band. Background counts were extracted from an annulus around Sgr A\* with inner and outer radii of 2" and 10", respectively, excluding regions around discrete sources and bright structures (Baganoff et al. 2003). The mean (total) count rates within the inner radius subdivided into the peak count rates during a flare and the corresponding IQ-values

<sup>1</sup>Chandra Interactive Analysis of Observations (CIAO), <http://cxc.harvard.edu/ciao>

<sup>2</sup><http://cxc.harvard.edu/caldb>

X-ray flare ID	Start time	Stop time	FWZP (min)	FHWM	Extraction Radius ["]	Total	Flare	IQ state
$\phi 1$	06 JUL 02:22:00	06 JUL 03:12:00	50±10	-	1.5	14 ± 7	8 ± 7	5.9 ± 1.0
$\phi 2$	06 JUL 23:09:00	06 JUL 23:34:00	25±10	-	1.5	18 ± 7	11 ± 7	7.0 ± 1.0
$\phi 3$	07 JUL 02:57:24	07 JUL 03:40:00	42±5	10±5	1.5	86 ± 7	79 ± 7	7.0 ± 1.0
$\phi 4$	07 JUL 03:40:00	07 JUL 04:00:00	20±5	-	1.5	20 ± 7	13 ± 7	7.0 ± 1.0

Table 3.5: X-ray flare count rates: Given are the peak times and peak ACIS-I count rates in  $10^{-3}/s$  in the 2 - 8 keV band of the total flare emission and the flare emission corrected for the count rate during the IQ state. The estimated start and stop times as well as the full width at zero power (FWZP) and full width at half maximum (FHWM) values are also listed, as well as the peak and IQ flux densities. The candidate X-ray flare events  $\phi 2$  and  $\phi 4$  coincide with significant near-infrared flares (labeled I and IV in tab. 6.1). The candidate X-ray flux density increase  $\phi 1$  is similar to  $\phi 2$ . For the weak candidate flare events  $\phi 1$ ,  $\phi 2$ , and  $\phi 4$  the FWZP values are estimated.

are listed in table 3.5. The background rates were scaled to the area of the source region. The mean source rate in the 1.5" aperture is notably consistent with the mean quiescent source rates from previous observations (Baganoff et al. 2001, 2003). The PSF encircled energy within each aperture increases from  $\approx 50\%$  for the smallest radius to  $\approx 90\%$  for the largest, while the estimated fraction of counts from the background increases with radius from  $\approx 5\%$  to  $\approx 11\%$ . Thus, the 1.0" aperture provides the best compromise between maximizing source signal and rejecting background.

### 3.5.2 SMA Observations

The *Submillimeter Array*<sup>3</sup> (SMA) is an interferometer operating at wavelengths between 1.3 mm and 450  $\mu\text{m}$  on Mauna Kea, Hawaii (Ho et al. 2004). SMA observations of SgrA\* were made at 890  $\mu\text{m}$  for three consecutive nights, 05–07 July 2004 (UT), with the latter two nights timed to coincide with the *Chandra* observing periods. On both July 6 and 7 more than 6 hours of simultaneous X-ray/submillimeter coverage was obtained (table 3.1); however, the longitudinal separation (nearly  $90^\circ$ ) between the VLT and the SMA limits the period of combined IR/X-ray/submillimeter coverage to approximately 2.5 hours. The weather degraded over the course of the three nights, from a zenith opacity at 890  $\mu\text{m}$  of 0.11 on July 5 to 0.15 and 0.29 on July 6 and 7, respectively, which is reflected in the larger time bins and scatter in the later light curves.

The SgrA\* observations were obtained as part of an ongoing SMA study of the submillimeter polarization of this source (Marrone et al., in preparation). Because these observations were obtained with circularly polarized feeds, rather than the linearly polarized feeds usually employed at these wavelengths, these data do not have the ambiguity between total intensity variations and modulation from linear polarization that afflict previous (sub)millimeter monitoring (e.g. Zhao et al. 2003). This technique does mix the total intensity with the source circular polarization, but measurements at 1.3 mm (Bower et al. 2003, 2005) show no reliable circular polarization at the percent level. In SMA polarimetric observations, only one out of every 16 consecutive integrations on SgrA\* is obtained with all antennas observing the same polarization (left or right circular) simultaneously, while the remaining integrations sample a combination of aligned and crossed polarizations on each baseline. For the light curves presented here (fig. 3.2), only those 50% of integrations on each baseline that were obtained with both antennas in the same polarization state were used, as cross-polar integrations sample the linear polarization rather than the total intensity. This unusual time sampling should not however affect the resulting light curves, as each point is an average of at least one cycle of 16 integrations.

The nearby quasars 1741–038 and 1749+096 were used for phase and gain calibration. On July 5 and 6, the observing cycle was 3.5 minutes on each of two quasars, followed by 14 minutes on SgrA\*. On July 7 a shorter cycle and stronger quasars were used due to poorer weather; 3.5 minutes on either 1741–038 or 1921–293 followed by 7 minutes on SgrA\*, with the two quasars interleaved near the end of the observations. Although 7 or 8 antennas were used in each track, only the same 5 antennas with the best gain stability were used to form light curves, resulting in a typical synthesized beam of 1.5"  $\times$  3.0". The poor performance of the other antennas was most likely caused by pointing errors.

<sup>3</sup>The Submillimeter Array is a joint project between the Smithsonian Astrophysical Observatory and the Academia Sinica Institute of Astronomy and Astrophysics, and is funded by the Smithsonian Institution and the Academia Sinica.

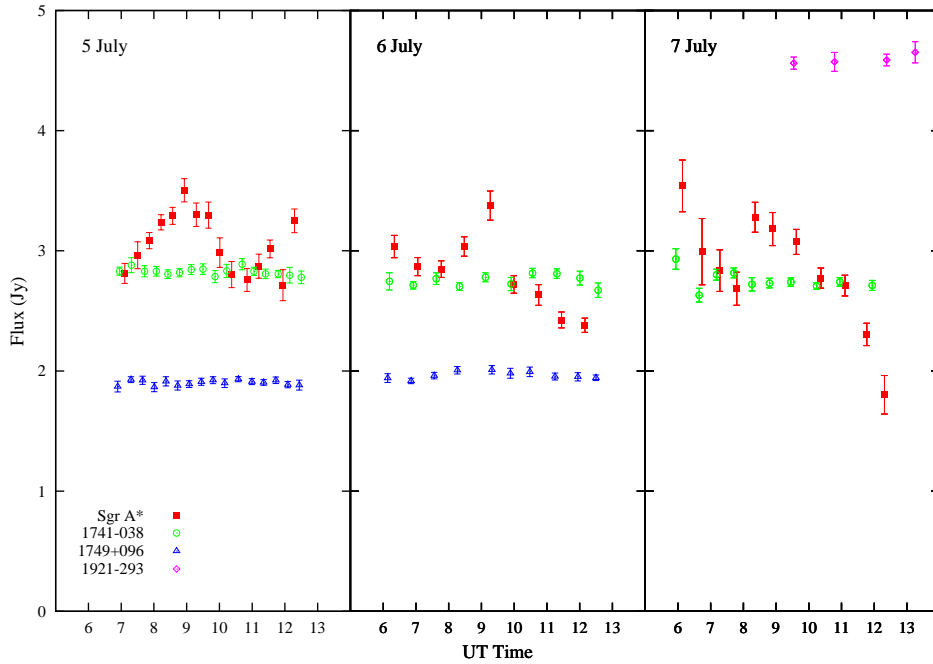


Figure 3.2: 890  $\mu\text{m}$  light curves from July 05-07. The light curves of the quasar calibrators, 1741–038, 1749+096, and 1921–293, are also shown. For each source Stokes I, i.e. the total intensity, is plotted. Due to poorer weather on July 06 and 07, two cycles have been averaged between Sgr A\* and the quasar calibrators for each data point for these days (see text), while the July 05 data is shown at full time resolution.

Images of the full three-day data set show very little emission away from SgrA\*, with peak emission around 3% of the amplitude of the central point source. To reduce sensitivity to the largest angular scales that are sampled, the two baselines that project to less than  $24 \text{ k}\lambda$  (angular scales  $>9''$ ) during the SgrA\* observations were excluded. A comparison of the variations in the three daily light curves versus hour angle shows no conclusive common variations above the 10% level, however, the presence of differential variations of 30% or larger will mask smaller systematic changes. It can be concluded that the surrounding emission is not responsible for changes larger than  $\sim 10\%$ , and may in fact be significantly less important.

The SgrA\* data was phase self-calibrated after the application of the quasar gains in order to remove short-timescale phase variations, then imaged and cleaned. Finally, the flux density was extracted from a point source that was fit at the center of the image, with the error taken from the noise in the residual image. The overall flux scale was set by observations of Neptune, with an uncertainty of approximately 25%. The complete data sets from each night show some systematic day-to-day flux variations across sources at the 15% level. These have been removed here by assuming that the mean of the quasar flux densities remain constant from day to day. Because multiple sources were used to remove this inter-day variation, this part of the absolute calibration is estimated to be accurate to about 10%. These uncertainties, however, do not affect the errors within each day’s

light curve.

### 3.5.3 VLA 7 mm Observations

Sgr A\* was observed with the *Very Large Array* (VLA) for  $\approx 5$  hours on 06 to 08 July 2004. The observations covered roughly the UT time range 04:40 to 09:00 (see also table 3.1), which is a subset of the Chandra observing time on 06 and 07 July. Observations on 06 July also overlapped with near-infrared observations. The VLA was in D configuration and achieved a resolution of  $2.5'' \times 0.9''$  at the observing wavelength of 7 mm. Fast-switching was employed to eliminate short-term atmospheric phase fluctuations and provide accurate short-term amplitude calibration. For every 1.5 minutes on Sgr A\*, 1 minute was spent on the nearby calibrator J1744-312. Antenna-based amplitude and phase gain solutions were obtained through self-calibration of J1744-312 assuming a constant flux density. Absolute amplitude calibration was set by observations of 3C 286. Flux densities were determined for Sgr A\* and J1744-312 through fitting of visibilities at  $(u, v)$  distances greater than  $50 \text{ k}\lambda$ . This  $(u, v)$ -cutoff removed contamination from extended structure in the Galactic center. The flux density of the two components of a transient source  $2.7''$  south of Sgr A\* (Bower et al. 2005) is fit simultaneously. The corresponding light curves of Sgr A\* for 6, 7 and 8 July 2004 are shown in fig. B.12 (see also table 3.1).

## 3.6 Photometry

### 3.6.1 Photometry of ISAAC and 2002 NAOS/CONICA images

The observing conditions for both the ISAAC and the 2002 NAOS/CONICA observations were generally photometric and adequate for relative photometry. For the ISAAC  $L$ - and  $M$ -band images, the calibration of the IRAF/DAOPHOT PSF-fitting results was linked to observed flux density reference stars. For the  $H$ - and  $K$ -band, data was taken from the literature (Clénet et al. 2001; Depoy 1990).

#### $L$ - and $M$ -Band magnitude calibration

For calibration purposes, the standard stars HD 130163 ( $m_L = 6.856$ ,  $m_L - m_M \approx 0$ , van der Bliik et al. 1996) and HR 5249 ( $m_M = 4.53$ , van der Bliik et al. 1996) were imaged together with science observations on May 28th 2002, using identical techniques. The airmass difference was small (maximum 0.2), resulting in corrections smaller than 0.04 magnitudes, which are insignificant given the much greater uncertainties in the photometry. First, the standard stars were measured with aperture photometry, using apertures of 1.14" radius and a sky subtraction annulus of 1.5" radius and computing the differences  $\Delta_1 = M_{\text{std}} - M_{\text{aperture}}$  between their published magnitudes and those measured. Then, approximately 30 isolated stars were measured in a single  $L$ - and  $M$ -band image each (c.f. section 3.1) of comparable seeing, using the same technique. For these stars, the differences  $\Delta_2 = M_{\text{aperture}} - M_{\text{DAOPHOT}}$  between their magnitudes as measured by aperture photometry and the magnitudes calculated by DAOPHOT from the final images were averaged and added to the above differences. These values  $\Delta = \Delta_1 + \bar{\Delta}_2$  were then subtracted from the DAOPHOT magnitudes to calibrate the final  $L$ - and  $M$ -band images.

#### Offset to other frequently applied $L$ -band calibrations

Since the applied  $L$ -band calibration introduces an offset of approximately 0.5 mag to the frequently used calibration of Blum et al. (1996), some comments are necessary.

Calibrating the  $L$ -band image with reference magnitudes taken from Clénet et al. (2001), as for the NAOS/CONICA  $K$ -band image (see below), resulted in  $(K - L)_{\text{obs}}$  colors which were *at least* 0.3 magnitudes too blue. An examination of the color-color-diagrams showed this effect to be systematic, since *the whole population* was blueshifted in  $K - L$ , whereas the  $H - K$  colors lie within the expected range for stellar sources. It is therefore unlikely that the  $K$ -band calibration is wrong, especially considering that it is based on stars shown to be non-variable (Ott et al. 1999; Clénet et al. 2001). Directly calibrating the  $L$ -band image with the observed calibration star instead of adjusting the zero-point with already published photometry does not show this effect. It is to be emphasized that Clénet et al. (2001) also found unusually blue  $K - L$  values, which they attributed to a lower  $K$ -band extinction. If the extinction law remains unchanged, this implicitly suggests a lower extinction  $A_V$ , which the observations and analysis of this dissertation can confirm (see section 4.1).

The  $L$ -band data and thus the calibration given by Blum et al. (1996), which is widely used and almost regarded as "standard", are taken from Depoy & Sharp (1991). Their calibration (which is not discussed in detail in their 1991 publication) was fixed with the star IRS 7, for which Blum et al. (1996); Tamura et al. (1996) and Ott et al. (1999) have shown that it is variable with an amplitude of of approximately one magnitude in the



*K*-band. This appears to be the main reason for the offset between the two calibrations. It seems that the offset to the other frequently applied calibration by Simons & Becklin (1996) is also due to their use of the variable source IRS 7 as flux calibrator. The new *L*-band calibration employed here, however, provides a clear improvement to this point, especially since it does not rely on any (non-)variability assumptions for the observed sources and does not result in unexpected *K* – *L* color effects. It should finally be noted that a higher extinction than the assumed  $A_V=25$  mag would result in even bluer *K* – *L* colors, requiring an even larger offset to the *L*-band calibrations mentioned above.

### ***K*-Band Magnitude Calibration**

Reference *K*-band magnitudes for some of the bright IRS sources were taken from Clénet et al. (2001), who fixed their zero-point with the photometry of Ott et al. (1999). The differences between the magnitudes calculated by the DAOPHOT software and the values of Clénet et al. (2001) were averaged, resulting in a calibration value which was subtracted from the DAOPHOT magnitudes. Saturated sources were excluded from the determination of the calibration magnitudes.

### ***H*-Band Magnitude Calibration**

Calibrating the *H*-band data proved difficult due to saturation — all *H*-band sources for which magnitudes have been published previously (e.g. Depoy (1990)) are bright and consequently saturated in the NAOS/CONICA image, whereas no magnitudes for the weaker unsaturated sources could be found in the literature.

As a solution to this problem, a secondary calibration was performed using an *H*-band mosaic made from images taken with the SHARP speckle imager in 1992 (Eckart et al. 1992). This image was flux calibrated using data for the brighter IRS sources (Depoy 1990). Subsequently, the NAOS/CONICA image was calibrated with the flux densities from weaker, isolated (i.e. clearly separated from their neighbors) sources in the SHARP mosaic image.

### **Uncertainties**

The total uncertainty of these photometry results is estimated as 0.25 magnitudes in the *H*- and *K*-band and 0.15 magnitudes in the *L*- and *M*-band. The difference is due to the different calibration procedures and the different shape of the respective point spread functions of the ISAAC and NAOS/CONICA images, resulting in less accurate fit results for the latter. The limiting magnitudes of this analysis are 12.73 (*M*-band), 14.47 (*L*-band), 17.66 (*K*-band) and 20.34 (*H*-band).

#### **3.6.2 Photometry of VISIR images**

Flux densities for the midinfrared sources were obtained using aperture photometry with an aperture of approximately 1" radius. Additional flux densities were obtained with apertures of 2" and 0.5" in order to correct for confusion effects for closely separated sources, and to optimise the background subtraction. For the purpose of local background subtraction, which is performed automatically by the aperture photometry task in the IRAF software package (PHOT), the sky contribution is fitted to an annulus situated between radii of 1.6" and 2.1" (from the center of the aperture) in the case of the 1" aperture, and

between 2.6" and 3.1" or between 1" and 1.5" for the 2" and 0.5" apertures, respectively.

This subtraction of the local background proved to be quite problematic, since the images have a variable remaining background contribution. This is due to the size of the Galactic center in relation to the size of the detector array, which makes the "standard" combined use of chopping and nodding as described in section 2.1.1 impossible. This fairly variable background combined with the large amount of extended emission of the minispiral at midinfrared wavelengths, which is often situated close to the pointlike sources studied here, made the automatically calculated sky contribution values for each source unreliable. It was therefore necessary to manually check the local background levels for each source and correct the subtracted sky contributions where these deviated significantly from the values in the image.

Since *no* calibration observations were made, it was necessary to flux calibrate the VISIR images using previously published photometry. However, this proved difficult, since very few *N*- or *Q*-band magnitudes or flux densities of Galactic center sources have been published to date. Since it is the *N*-band source studied in greatest detail up to now (e.g. Gezari et al. 1985; Tanner et al. 2002), IRS 21 was selected as flux calibration source. The flux densities for IRS 21 at 8.8, 12.5, 20.8, and 24.5  $\mu\text{m}$  given by Tanner et al. (2002) were interpolated (or extrapolated, where appropriate) from, assuming that the emission from IRS 21 follows the general shape of the integrated Galactic center spectrum as measured by ISO (Lutz et al. 1996). At 8.6  $\mu\text{m}$ , the flux density at 8.7  $\mu\text{m}$  published by Stolovy et al. (1996) was also taken into account. Corrections for the different aperture sizes and background subtraction were then applied. For extinction correction,  $A_V=25$  (Scoville et al. 2003; Viehmann et al. 2005a) was assumed (see also section 4.1.1), adopting the extinction law of Moneti et al. (2001) for the *N*- and *Q*-bands.

The total uncertainty (i.e. statistical and systematic) of the photometry results is estimated as  $\pm 30\%$ , rising to  $\geq \pm 50\%$  for the faintest sources ( $\leq 0.5$  Jy). The dominating uncertainty here is that of the background subtraction (for the fainter sources) and also the flux density calibration.

## Chapter 4

# Colour analysis of stellar sources in the Galactic Center

In this chapter the results of my analysis of the ISAAC and the 2002 NAOS/CONICA images are discussed (see also Viehmann et al. 2005a,b). The large number of sources for which near- and mid-infrared color data were obtained permit conclusions about the extinction to the central region, specifically in the  $M$ -band, and about the color properties of the stellar population in this region (limited to the brighter stars due to the resolution and sensitivity of ISAAC). I also discuss the morphology of the bright and enigmatic (mid-) infrared source IRS 3, since it shows some intriguing properties.

### 4.1 Extinction to the Galactic Center

For de-reddening purposes, the extinction law of Rieke & Lebofsky (1985) for the Galactic center was adopted, i.e.  $A_H = 0.175A_V$ ,  $A_K = 0.112A_V$ ,  $A_L = 0.058A_V$  and (initially)  $A_M = 0.023A_V$ . However, since recent work by Scoville et al. (2003) indicates that the extinction toward the Galactic center exhibits a broad minimum over the area of the IRS 16 Cluster and the Northern Arm, their value of  $A_V = 25$  magnitudes was assumed, instead of the “traditional” average value of  $A_V = 27$  or even 30 magnitudes (Rieke 1987). This choice is supported by the colors of the stars observed, especially the  $K - L$  colors (see section 3.6.1), since they would otherwise appear unnaturally blue.

In the  $HKL$  color-color diagram (fig. B.4), the majority of sources form a cluster in the area typically populated by stars (for intrinsic colors see Koornneef 1983), with a fairly sharp boundary towards bluer colors. This result is satisfactory, since the majority of sources exhibit colors that lie in the possible color range for stellar sources, and only *very few* objects, which can be seen as exceptions, show bluer colors. Quite a few objects appear to be strongly reddened, especially within the inner area covered by the NAOS/CONICA images (fig. B.3), which is not surprising, since the dust and gas of the ‘mini-spiral’ passes through this region.

The conclusion to be drawn here is that the newer findings concerning extinction (Scoville et al. 2003), together with this new  $L$ -band calibration, provide a consistent picture without requiring modifications of the extinction law at this point, in particular in the  $K$ -band.

#### 4.1.1 Comparison of outer and inner field

With the exception of some highly reddened sources (e.g. IRS 1W, IRS 3, IRS 10, IRS 21) found almost exclusively within the inner field (i.e. the  $18'' \times 18''$  of the NAOS/CONICA field of view), the stars from the inner and outer regions cluster in the same area of the two-color diagrams, with the clustering much more pronounced for the stars from the outer region. The highly reddened sources from the inner field are apparently obscured/reddened by gas and dust from the mini-spiral (either directly or by a bow-shock type interaction). The  $H - K$  and  $K - L$  colors obtained from the data analyzed here confirm the results of Scoville et al. (2003) for the lower extinction ( $A_V=25$  mag is assumed) towards the IRS 16 cluster and the Northern Arm of the mini-spiral, since these colors – after dereddening – agree with the intrinsic colors of stars given by Koornneef (1983). This is especially true if one excludes unusual stars such as Wolf-Rayet stars etc. Any higher extinction would lead to significantly bluer intrinsic colors, which cannot be explained in a straightforward manner. The data obtained indicates that this relatively low extinction applies to the complete region covered by the (higher-resolution) ISAAC images, i.e. the inner  $70'' \times 70''$ . This can be inferred from the two-color diagrams (Figs. B.4 and B.5), since the populations of both the inner and outer region cluster in the same area of these diagrams. If the extinction were to increase significantly within the ISAAC high resolution field of view, the ‘outer’ population (or at least a significant part of it) should show systematically redder colors than the main part of the ‘inner’ population, which is clearly not the case. The higher extinctions of 35 to 50 mag reported by Scoville et al. (2003) thus probably apply to areas outside the inner 70 arcseconds. This is consistent with the location of the circumnuclear molecular ring, which has a sharp inner edge (Latvakoski et al. 1999).

#### 4.1.2 $M$ -band extinction

The  $M$ -band calibration achieved here, using two calibration stars of significantly different magnitude (see section 3.6.1), provides rather surprising results: the stars appear too blue by about 0.7 mag in  $L - M$ , if one applies the reddening law of Rieke & Lebofsky (1985) for the Galactic center, i.e.  $A_M = 0.023A_V$ . However, the ISO/SWS Galactic center extinction measurements of Lutz et al. (1996) and Lutz (1999), while generally in agreement with the extinction law of Rieke & Lebofsky (1985), permit considerably higher (or even lower) extinctions in the 4-5  $\mu\text{m}$  regime within their uncertainties. This is especially true if one considers that their extinction values increase again longward of 5  $\mu\text{m}$ . Visual inspection of the distribution of  $L - M$  colors in the color-color diagram (fig. B.5) suggests that  $A_M \approx A_L$ , since the bulk of the  $L - M$  colors observed then agree with the expected  $L - M$  colors for stellar sources (Koornneef 1983).

The extensive  $L - M$  color data obtained, available for a total of 541 sources (see table A.2 for data of the sources outside the NAOS/CONICA field of view of approximately  $18'' \times 18''$ ), permits a more precise quantification of the  $M$ -band extinction, assuming that the theoretical intrinsic colors given by Koornneef (1983) are valid. From the mean observed and theoretical intrinsic  $L - M$  colors, averaged over all types of stars, the  $M$ -band extinction can be calculated via:

$$\frac{A_M}{A_V} = \frac{1}{A_V} (\langle L - M \rangle_{\text{Koornneef}} - \langle L - M \rangle_{\text{obs}} + A_L) = 0.056 \pm 0.006,$$

quoting a  $3\sigma$  uncertainty. This result is plotted in fig. 4.1 and agrees very well with the above estimate of  $A_M \approx A_L$ , with  $A_L = 0.058A_V$  following Rieke & Lebofsky (1985).

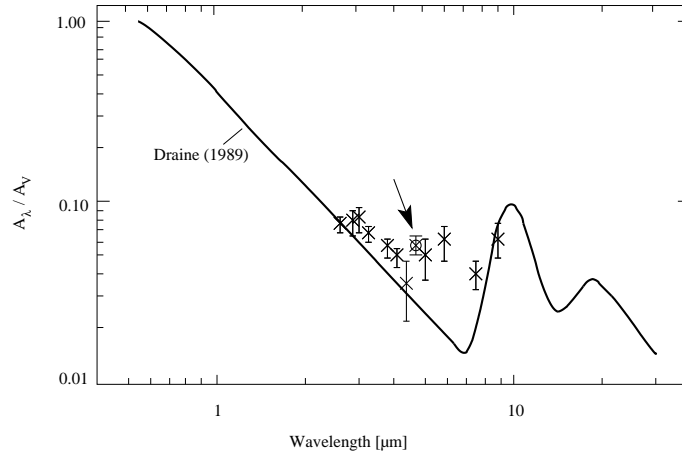


Figure 4.1: Extinction towards Sgr A\* according to Lutz et al. (1996). The data points are derived from SWS H recombination line data, while the solid curve is the extinction law of Draine (1989) for standard graphite-silicate mixes. The data point marked by an arrow is the new  $M$ -band result.

Any possible luminosity-induced bias (i.e. the observed stars are bright) is  $< 0.003$  and therefore totally insignificant given the uncertainties.

Assuming a Gaussian distribution of the  $L - M$  values for simplicity, the corresponding standard deviation is  $\sigma_{L-M} = 0.51$ , which allows the calculation of the contribution  $\sigma_{\text{ext}}$  of screening and source intrinsic effects to the  $L - M$  distribution. The uncertainties of the distribution are given by

$$\sigma_{L-M}^2 = \sigma_L^2 + \sigma_M^2 + \sigma_{\text{Koornneef}}^2 + \sigma_{\text{ext}}^2$$

where  $\sigma_{\text{Koornneef}} = 0.16$  represents the scattering of theoretical intrinsic colors over the whole range of stellar types as listed by Koornneef (1983). Here  $\sigma_L$  and  $\sigma_M$  are the uncertainties in the  $L$ - and  $M$ -band magnitudes. The result obtained is  $\sigma_{\text{ext}} = 0.44$ , which implies that the *main* contribution to the width of the  $L - M$  color distribution is due to screening effects and source-intrinsic reddening (i.e. local dust concentrations etc.). The main caveat here is that the  $L - M$  color distribution is not Gaussian (there are two principal stellar types with different intrinsic colors, i.e. red giants and young, massive emission-line stars). However, the width of the distribution due to different stellar type components is considerably smaller than the scattering observed. Nevertheless, this analysis is useful as a preliminary estimate, and further  $M$ -band studies of the Galactic center would be extremely helpful to clarify the situation.

## 4.2 Colours of He-emission-line stars and red giants

A comparison of the  $L - M$  colors of the named sources of known type (i.e. He-stars or cool red giants/AGB) shows a fairly clear color separation, with the cool stars significantly *bluer* than the hot ones (see table A.1 and fig. B.5). This seemingly astonishing result is in general agreement with the colors given by Koornneef (1983): Hot stars have on average an  $(L - M)_{\text{intrinsic}}$  color of  $\approx -0.05$ , while cool giants have  $(L - M)_{\text{intrinsic}}$  values

of typically  $-0.2$  to  $-0.3$ . In this sample, the average observed  $(L - M)_{\text{obs}}$  values are  $0.46 \pm 0.17$  for the emission-line stars and  $-0.05 \pm 0.27$  for the cool stars (ten of each, see table A.1), with the standard deviation as uncertainty. Therefore, the  $L - M$  color, and more particularly the  $H - K$  versus  $L - M$  color-color diagram is a reasonably good diagnostic tool for preliminary identification of these stellar types. Applying this  $L - M$  criterion to the observed data, the emission-line stars are found clearly concentrated in the inner region, with only about ten emission-line-star candidates in the area outside the  $18'' \times 18''$  NAOS/CONICA field of view (containing 166 objects with full  $H$ - to  $M$ -band photometry data), as opposed to at least forty such objects in the inner region (which contains 197 objects in total).

$K - L$  colors are much less useful in this context, since the  $K - L$  color separation is comparatively low. Naturally, spectroscopic evidence is required for a definite classification. An additional comment can be made on the dereddened (i.e. intrinsic)  $(K - L)_{\text{intrinsic}}$  and  $(L - M)_{\text{intrinsic}}$  colors of the He-stars. These appear to be slightly but systematically redder ( $\approx 0.2$  mag) than expected for hot stars, whose  $(K - L)_{\text{intrinsic}}$  and  $(L - M)_{\text{intrinsic}}$  colors are approximately 0 to  $-0.1$ . This indicates the presence of an infrared excess. A possible explanation for such an excess could be that the He-stars all show signs of an interaction with the dusty interstellar medium at the Galactic center. This excess could be of a similar nature but much less pronounced than the bow shock sources along the mini-spiral (Tanner et al. 2002, 2003; Rigaut et al. 2003; Eckart et al. 2004b; Clénet et al. 2004a). This result is in general agreement with the findings of Davidge et al. (1997), who indicate that the  $K - L$  colors of the He-stars are clearly redder than those of known emission line stars in the Large Magellanic Cloud.

### 4.3 Structure of IRS 3 in the $L$ - and $M$ -band

One of the most intriguing mid-infrared sources in the Galactic center region is IRS 3. In the  $L$ - and  $M$ -band, this is the most extended source observed here, and also one of the brightest ( $m_M = 3.4$ ). It is much fainter in the  $K$ -band, hardly visible in the  $H$ -band ( $m_K = 10.6$ ,  $m_H = 15.0$ ), and also hardly extended at these shorter wavelengths (see

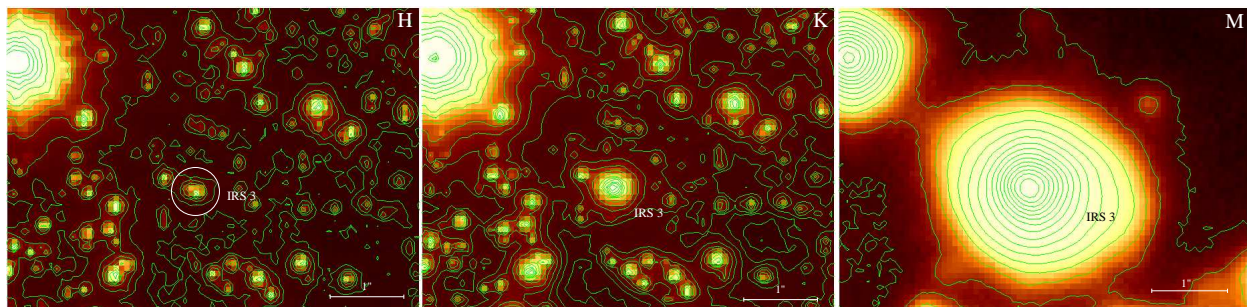


Figure 4.2:  $H$ -,  $K$ - and  $M$ -band view of IRS 3 (encircled in the  $H$ -band view). The bright source to the northeast (upper left) is the supergiant IRS 7. A histogram equalization color scale is used, while the contour lines follow a logarithmic scale in order to show the IRS 3 source structure as clearly as possible.

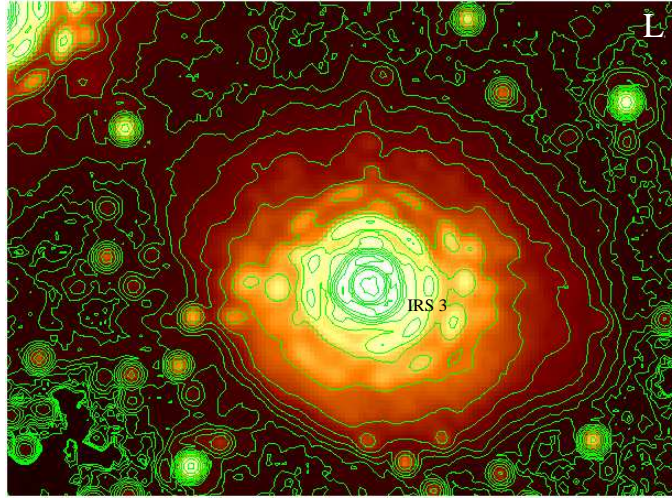


Figure 4.3: *L*-band view of IRS 3 with NAOS/CONICA (Eckart et al. 2004b). The circular structures surrounding the bright sources are due to the adaptive optics. Note the asymmetry in the lower contour lines producing a bow-shock-like effect at the southern edge of the extended emission.

figs. 4.2 and 4.3). Consequently, IRS 3 appears to be dominated by dust emission. According to Krabbe et al. (1995), IRS 3 has an almost featureless, red continuum *K*-band spectrum. IRS 3 also emits strongly at  $10\ \mu\text{m}$  (e.g. Gezari et al. 1985, and section 5.1). In this analysis, the *M*-band photocenter of IRS 3 is shifted to the northwest by  $\sim 0.16''$  with respect to the *H*-, *K*- and *L*-band positions. This angular separation is clearly higher than the relative positional uncertainty of  $0.035''$  that was estimated above and thus not a mere artifact. A visual inspection of the maps clearly shows, however, that the two sources detected by the PSF-fitting algorithm are not distinct sources, but a consequence of the extended flux density distribution. This shift of the photocenter of the extended *M*-band emission relative to the photocenter at shorter wavelengths, combined with the clearly visible asymmetry of the lower contour lines in the NAOS/CONICA *L*-band image (fig. 4.3) results in a bow-shock-like appearance, similar to the sources discussed by Tanner et al. (2003), although much less distinct than the remarkable source mentioned by Clénet et al. (2004a). The asymmetry is the consequence of a compression of the extended emission at its southern edge, resulting in a steeper flux density gradient (“bunched” contour lines). A possible explanation for this unusual appearance is that IRS 3 consists of a mass-losing star, e.g. a young, dust-embedded O star (Krabbe et al. 1995) or a dusty protostar or Wolf-Rayet star (Tanner et al. 2003; Horrobin et al. 2004), or possibly even a red supergiant or extreme AGB star (Pott et al. 2005), surrounded by a very thick, extended dust shell, which is pushed northwest by wind from the direction of the IRS 16 cluster and Sgr A\*. Gezari et al. (1985) give a temperature of  $\approx 400\ \text{K}$  for this strong *L*-band source. The *H*- and *K*-band emission appears to be dominated by the stellar source and is therefore not extended. The dust shell must be very thick, however, since IRS 3 is a faint source in the *K*- and especially *H*-band. The shift in the *M*-band emission is due to part of the dust shell being extended to the northwest. It should be possible to clarify the nature of IRS 3 through *L*- and *M*-band and even longer wavelength studies

at higher resolution, i.e. using adaptive optics or interferometric methods that are now becoming available for infrared observations (e.g. VLTI or the upcoming LBT, see Eckart et al. 2003a).



## Chapter 5

# Compact $N$ - and $Q$ -band sources in the Galactic Center

In this chapter, I present the results of my analysis of the VISIR commissioning observations of the Galactic center (Viehmann et al. 2006). I have obtained photometry for a total of 35 sources at  $19.5 \mu\text{m}$  rising to 64 sources at  $8.6 \mu\text{m}$ . This is probably the largest number of Galactic center sources investigated in the  $N$ - and  $Q$ -bands up to now and includes the first detection of the Galactic center Helium-emission-line stars IRS 16NE, IRS 16NW and AF/AHH, as well as the red giants IRS 12N, IRS 14NE and IRS 14SW in the  $N$ -band, as shown in fig. B.8. Additionally, it is now possible to separate the WC9 star IRS 6E (Blum et al. 1996) from the bright extended emission associated with IRS 6W. The corresponding data can be found in table A.3.

### 5.1 Classification of sources by SED

Combining the VISIR data with shorter wavelength data enables the construction of an unprecedented (for the Galactic center) number of spectral energy distributions (SEDs) across the whole  $1.6$  to  $19.5 \mu\text{m}$  spectral range. These are shown in figs. B.9 and B.10. Preliminary analysis of all of the most typical cases indicates that these SEDs can provide interesting information on the source characteristics, since different source types have SEDs of considerably different shape. This could possibly allow for preliminary classification of presently unclassified sources. The different types of SED found in this sample are as follows:

#### I. Northern Arm embedded sources

These are luminous sources that are embedded in the “Northern Arm” stream of gas and dust, and also in the bar area of the minispiral. IRS 1W, 2L, 5, 10W and 21 belong to this group, which shows very red and fairly featureless SEDs, with their maximum in the  $N$ -band, indicating fairly low temperatures (approximately 300 K according to Gezari et al. 1985). These objects are now successfully described as bow shock sources (Tanner et al. 2002, 2003, 2005; Rigaut et al. 2003; Eckart et al. 2004b; Geballe et al. 2004). The source complex IRS 13E, which is situated in the bar area of the minispiral, shows very similar characteristics, although it is clearly hotter (Gezari et al. 1996), with the embedded source identified as a cluster of massive young stars (e.g. Krabbe et al. 1995; Najjarro et al. 1997; Eckart et al. 2004b; Maillard et al. 2004).

## II. Lower luminosity bow shock sources

These sources are less luminous and often situated close to the edge of the minispiral. In almost all cases, they are identified as bow-shock sources by their morphology, the bow-shock structure being visible in high-resolution *L*- or *M*-band images obtained with adaptive optics (see e.g. Genzel et al. 2003; Clénet et al. 2004b, for such images). A striking example (source 41 in this sample) is presented by Clénet et al. (2004a). These sources show very red SEDs with their maxima longwards of 12  $\mu\text{m}$ . Their characteristics at shorter wavelengths are diverse: some show a fairly flat SED between 1.6 and 11.3  $\mu\text{m}$ , while others exhibit a minimum around 8.6  $\mu\text{m}$ . These differences are probably due to differences between the type of stars powering the bow-shocks (see below), and due to the presence and density of the dusty medium that surrounds them and with which they interact. Therefore, IRS 2S, which has been classified as a cool red giant by Blum et al. (1996), probably belongs to this type of source, since it shows a flat SED from 1.6 to 11.3  $\mu\text{m}$  and brightens considerably at longer wavelengths.

## III. Cool stars

The SEDs of these sources all have their maximum in the 2 to 5  $\mu\text{m}$  region. The SEDs then fall off to the *N*-band, where they appear to flatten out. In those cases which are still detectable at wavelengths longer than 8.6  $\mu\text{m}$  (despite decreasing resolution and sensitivity), the *N*- and *Q*-band flux densities of this type of source appear to be more or less constant for each source. This effect is probably due to circumstellar dust emission, which is to be expected, since the brightest cool red giants at the Galactic center have been identified as AGB stars (Ott et al. 1999; Clénet et al. 2001) and are thus situated in a mass-loss phase, creating dust envelopes. A *weak* bow-shock type interaction with the surrounding medium is also possible in the case of AGB stars, since they have fairly strong stellar winds.

## IV. Hot stars

These sources exhibit SEDs that fall off steeply (i.e. steeper than those of cool stars) between 5 and 8  $\mu\text{m}$ . Therefore, the *M* – *N* color (more particularly *M* –  $m_{8.6\mu\text{m}}$ ) might be useful as a criterion for distinguishing hot and cool stars, if spectroscopic information is not available. The clearly identified hot stars in this sample fall into two distinctive subgroups: The Galactic center He-stars IRS 16NE, IRS 16NW and AF/AHH, which are frequently classified as LBV or Ofpe/WN9 (e.g. Clénet et al. 2001), are brightest at short wavelengths with SEDs that fall monotonically towards longer wavelengths. The dominant source of infrared emission in these cases is thus probably photospheric, with a wind (or faint bow shock) contribution in the *L*- and *M*-band (see Viehmann et al. 2005a). On the other hand, IRS 29 and IRS 6E, which have been classified as WC9 Wolf-Rayet stars (e.g. Blum et al. 1996), exhibit SEDs which peak in the *L*- and *M*-bands, while their *H*- and *K*-band flux densities are considerably lower. The corresponding interpretation is that these stars are surrounded by a (most probably) self-generated dust shell, which partly extinguishes the shorter wavelength emission and itself emits strongly at 3 - 5  $\mu\text{m}$  (see also Moutaka et al. 2004a).

## V. IRS 3

This source clearly stands apart from all other Galactic center mid-infrared sources. While Horrobin et al. (2004) classified IRS 3 as a WC5/6 star, Pott et al. (2005) and R. Genzel (2005, private communication) have pointed out that this identification probably

applies to a different, fainter source situated approximately  $0.12''$  to the east of IRS 3. This does not rule out that IRS 3 may be a massive Wolf-Rayet star, but Pott et al. (2005) have also shown that it may be an extreme AGB star. The true nature of IRS 3 therefore remains unclear. Among the bright  $N$ -band sources, it is the most compact (see new interferometric MIDI VLTI results by Pott et al. 2005), apart from IRS 7 (Gezari et al. 1985). It is also the brightest source in the  $M$ -band and one of the brightest over the whole mid-infrared region covered here ( $L$ - to  $Q$ -band), while it appears unremarkable in the  $K$ -band and very faint at shorter wavelengths. The shape of the SED of IRS 3 is thus unlike any of the typical cases discussed at present: IRS 3 is much fainter than the luminous bow-shock sources in the near-infrared, while clearly hotter (approximately 400 to 600 K, see Gezari et al. 1985, 1996) and thus showing maximum emission at a shorter wavelength ( $M$ -band versus  $10\ \mu\text{m}$ ). Compared to luminous cool stars (IRS 7, IRS 10E\*), IRS 3 is clearly fainter at near-infrared wavelengths and much brighter in the  $N$ - and  $Q$ -bands. The same applies to the comparison of IRS 3 with the hot stars in this sample. However, a certain similarity to the SED of IRS 29 (WC9 type) is discernible: The source is faint and obviously extinguished in the  $H$ -band, has a maximum at short mid-infrared wavelengths ( $L$ - and  $M$ -band) and shows a fairly clear absorption feature at approximately  $10\ \mu\text{m}$  (see section 5.2). The reason for this similarity is that the emission from both objects comes from thick, probably self-generated dust shells (compare Viehmann et al. 2005a).

## 5.2 Intrinsic silicate absorption

The spectral region between  $8.6\ \mu\text{m}$  and  $12\ \mu\text{m}$  is especially interesting, since there is a broad interstellar silicate absorption feature at  $9.7\ \mu\text{m}$  (Lutz et al. 1996). The data obtained at  $11.3\ \mu\text{m}$  lie on the flank of this absorption; consequently, sources that are underluminous at this wavelength appear to show additional, and therefore *intrinsic* silicate absorption, i.e. absorption in excess of that found in the overall ISO spectrum (Lutz et al. 1996). IRS 3 and IRS 6W clearly show this effect, which is also visible in fig. B.6 (lack of green), as do IRS 34 (both components) and source 24. The most likely explanation is that these stars are surrounded by (possibly self-generated) dust shells containing additional silicate dust. The cool star IRS 10E\* and the hot stars IRS 6E and IRS 29, which have been identified as WC9 Wolf-Rayet stars (e.g. Blum et al. 1996), might also show signs of such absorption, although the steepening of their SED is slight and may therefore be insignificant. In the case of the WC9 stars (*carbon rich!*), intrinsic *silicate* absorption is difficult to explain; however, one possibility is that the absorption is due to collected material that was not originally produced by the stars themselves. Enhanced, patchy foreground extinction over the whole IRS 3 to IRS 6W area is a possible alternative explanation.

In contrast, none of the luminous, bow-shock dominated sources shows intrinsic silicate absorption. Therefore they appear yellow in the color image shown in fig. B.6. It seems that the lower luminosity bow-shock sources also do not show such an absorption effect.

## 5.3 Excess emission at $12.8\ \mu\text{m}$

Due to the shape of the Galactic center spectrum (e.g. Lutz et al. 1996), slightly higher flux densities are to be expected at  $12.8\ \mu\text{m}$ , which is clearly visible in the obtained SEDs. However, some sources show a larger excess, which appears to indicate additional intrinsic

emission at  $12.8 \mu\text{m}$  and must be explained.

While Willner (1978) state that the  $12.8 \mu\text{m}$  Ne II line emission at the Galactic center is extended and not associated with compact mid-infrared sources, Lacy et al. (1979, 1980) find that part of the Ne II emission comes from compact regions of ionized gas which are indeed associated with mid-infrared continuum sources. Consequently, Ne II line emission is a possible explanation for at least some of these excesses.

In the case of IRS 10E\* (and IRS 9 if the small  $12.8 \mu\text{m}$  excess of this source is significant), the  $12.8 \mu\text{m}$  excess is attributed to a narrow streamer of enhanced emission running approximately southwards from IRS 5, which probably resulted in an insufficient background subtraction (see section 3.6.2). The excess  $12.8 \mu\text{m}$  emission of IRS 2, 6W and 13 could also be the result of insufficient background subtraction due to the clumpy nature of the extended emission from this part of the minispiral, which shows quite a complex structure. The excess  $12.8 \mu\text{m}$  emission clearly visible in the SEDs of IRS 3, 7 and possibly 29 (and also visible in fig. B.6), however, cannot be explained in this fashion. Since Lacy et al. (1980) state that IRS 3 and IRS 7 do not have associated gas clouds, it appears highly unlikely that the excess of these sources is due to Ne II line emission. It is therefore suggested that the excess of these sources at  $12.8 \mu\text{m}$  is due to continuum emission caused by a faint bowshock-like interaction of the stellar winds of these stars with the surrounding medium. Since this is a small effect, the corresponding excess that is to be expected at  $11.3 \mu\text{m}$  could be masked by intrinsic silicate absorption (see above). The absence of a clearly visible excess at  $18.7 \mu\text{m}$  in these sources does not rule out such an explanation, since the known bow-shock sources (types I and II in section 5.1) show diverse characteristics in the *Q*-band (the fainter sources have their maxima there, the brighter ones have their maxima in the *N*-band).

## 5.4 Unusual sources east of IRS 5

Among the most intriguing mid-infrared sources at the Galactic center are four bright pointlike sources located to the east of the bright Northern Arm source IRS 5. The nature of these sources, which are referred to as IRS 5NE, IRS 5E, IRS 5S, and IRS 5SE (see fig. B.8), is currently unclear. They are remarkable in that they are almost as bright as IRS 7 in the *N*-band, while they appear much less prominent at shorter wavelengths, although they remain bright in the *L*- and *M*-bands. Detailed inspection reveals that IRS 5SE, which appears *slightly* extended at longer wavelengths, is in fact double, consisting of a blue point source to the east (IRS 5SE2, dominant component in *K*-band images) and a fainter source to the west, which shows a tail like structure and is the main source of emission at longer wavelengths (IRS 5SE1, dominant component in *N*- and *Q*-band). This represents an intriguing case of possible interaction, either of the two sources with each other – if they lie close together along the line of sight – or of the western component with the surrounding Galactic center interstellar medium. A further possibility is that a bow shock generated by the eastern component is superimposed on the western one, however, their separation makes this unlikely.

All of these sources except IRS 5SE2 show SEDs that are either flat between  $3.8$  and  $20 \mu\text{m}$  (IRS 5NE) or increase dramatically towards longer wavelengths. Therefore, these sources show similar characteristics to identified lower-luminosity bow-shock sources (e.g. IRS 9N, see section 5.1), however, their appearance on high-resolution NAOS/CONICA *K*- and *L*-band images does not indicate such a structure, which is normally visible for this type of source (IRS 5SE1 is the obvious exception here). It therefore appears that a reliable

classification and understanding of these sources can only be achieved with spectroscopic methods or possibly interferometry using VLTI.



## Chapter 6

# Flare Activity and midinfrared Properties of Sgr A\*

In this chapter, I present the results of the 2004 coordinated multi-wavelength observing campaign concerning the flare activity of Sgr A\*, and especially the derivation of new, tighter constraints for its spectrum in the mid-infrared regime, where my analysis of the VISIR commissioning data provides tight upper flux density limits (see also Eckart et al. 2006a).

### 6.1 Light Curves of flaring events of Sgr A\*

Obs. ID	IR flare ID	$\lambda$ [ $\mu\text{m}$ ]	Start	Stop	FWZP [min]	FWHM [min]	peak flux [mJy]	IQ flux [mJy]
1		1.7					<4.1	$2.60 \pm 0.5$
2		2.2						$3.20 \pm 0.7$
3		3.8						$23.0 \pm 11.0$
4	I	2.2	< 06 July 23:19:39	06 July 23:32:00	>12	>6	$\geq 5.7$	$3.00 \pm 1.0$
4	II	2.2	07 July 00:29:00	07 July 02:39:00	130	>70	$\sim 3.0$	$3.00 \pm 1.0$
4	III	2.2	07 July 02:59:00	07 July 03:39:00	45	25-35	$6.0 \pm 1.5$	$3.00 \pm 1.0$
4	IV	2.2	07 July 02:39:00	07 July 03:59:00	20	$\sim 10$	$5.0 \pm 1.5$	$3.00 \pm 1.0$
5		3.8						$17.0 \pm 4.0$
6	V	2.2	08 July 02:33:00	08 July 04:03:00	95	40-55	$4.0 \pm 1.0$	$3.00 \pm 1.0$

Table 6.1: Emission properties of the near-infrared flare events from the infrared counterpart of Sgr A\*. For each observing session the estimated IQ flux density is given. This corresponds to the mean flux density during its low flux density state during that observing session. The peak flux densities are corrected for the IQ state flux density. The flux densities are dereddened using  $A_H = 4.3$ ,  $A_K = 2.8$ , and  $A_{L'} = 1.8$ . In case of a flare event detection, the full zero start and stop times, the full zero width at the corresponding zero points (FWZP) and the full width at half maximum of the flare events are listed. The time period given with the infrared flare event II corresponds to a time of slightly increased source activity.

The light curves obtained (see sections 3.2 and 3.5.1) show several flare events. In the

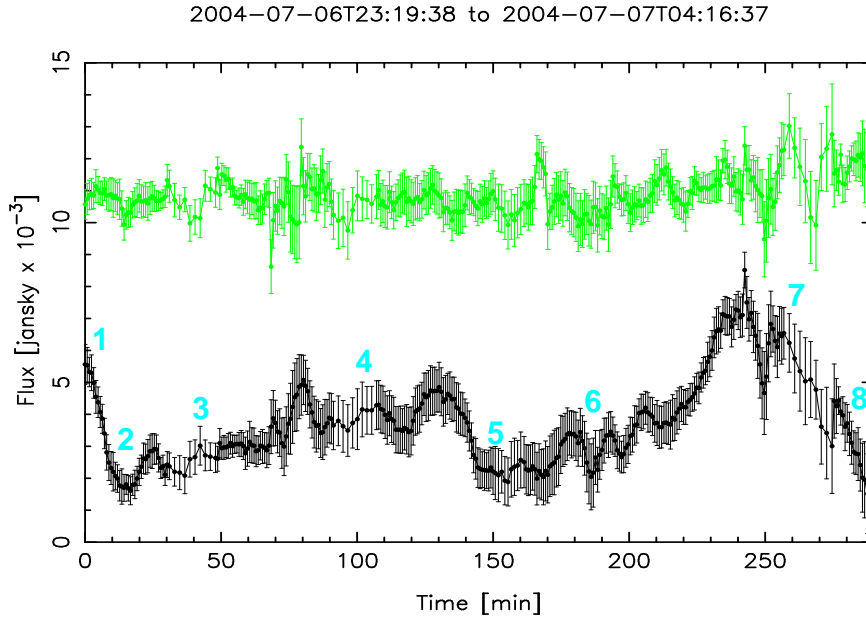


Figure 6.1: Light curve of the  $K$ -band observations from July 07 (see fig. B.11). The plot shows the light curves of S1 (top) and SgrA\* (bottom). The background level has been subtracted from both plots. The numbers near the light curve of Sgr A\* mark the approximate times for which images are shown in fig. 6.4.

following the identification of individual flares is based on their significant detection in at least one of the observed wavelength bands. Significant detections of five near-infrared flare events (labeled I to V in table 6.1, see also fig. 6.2) and one bright X-ray flare (labeled  $\phi 3$  in table 3.5, see also fig. 6.3) were obtained in total. For four of the five near-infrared events, simultaneous data coverage in both of these wavelength domains is available. In figs. 6.1 and 3.1, the light curve of the  $K$ -band imaging from 7 July is shown separately. Four near-infrared flare events (I - IV) can be seen, all of which were covered by simultaneous *Chandra* observations. In fig. 6.4, images corresponding to the time points marked in fig. 3.1 are shown. These images illustrate the “on” (i.e. flaring) and “off” (IQ) states of Sgr A\*.

In the X-ray regime the weak flux density increases labeled  $\phi 2$  and  $\phi 4$  in table 3.5 (see also fig. 6.5), which coincide with the significant near-infrared flares labeled I and IV in table 6.1 and fig. 6.3, and one weak X-ray flux density increase  $\phi 1$ , which is similar to  $\phi 2$ , should be emphasized. These events are considered as weak flare candidates in the following discussion. The interest in the weak events  $\phi 2$  and  $\phi 4$  is strengthened by the cross-correlation with the corresponding near-infrared flares (see fig. B.13). Fig. 6.5 shows that the weak X-ray flare  $\phi 1$  did not have a detectable  $H$ -band counterpart. The  $H$ -band observations started almost exactly at the time of the peak X-ray emission.



X-ray flare ID	NIR flare ID	X-ray flux density [nJy]	NIR flux density [mJy]	NIR band	spectral index $\alpha_{NIR/X-ray}$
$\phi 1$		$22 \pm 27$	$2.6 \pm 0.5$	<i>H</i>	$-1.34 \pm 0.2$
$\phi 2$	I	$31 \pm 27$	$\geq 5.7$	<i>K</i>	$-1.35 \pm 0.2$
	II	$< 20$	$\sim 3.0$	<i>K</i>	$< -1.34$
$\phi 3$	III	$223 \pm 27$	$6 \pm 1.5$	<i>K</i>	$-1.12 \pm 0.05$
$\phi 4$	IV	$37 \pm 27$	$5 \pm 1.5$	<i>K</i>	$-1.35 \pm 0.2$
	V	-	$4 \pm 1.0$	<i>K</i>	-

Table 6.2: NIR/X-ray flare flux densities. Given are the peak flux densities of the flares detected in the individual wavelength bands. The spectral index is calculated assuming band centers of  $2.2 \mu\text{m}$  and  $1.6 \mu\text{m}$  in the near-infrared and 4 keV in the X-ray domain. The X-ray flares  $\phi 2$ ,  $\phi 3$ , and  $\phi 4$  have been detected simultaneously in the near-infrared. For flare  $\phi 1$  only an upper limit in the *H*-band is available. For flare V no X-ray data exist. See comments to the candidate X-ray flare events  $\phi 1$ ,  $\phi 2$  and  $\phi 4$  in the text and in table 3.5.

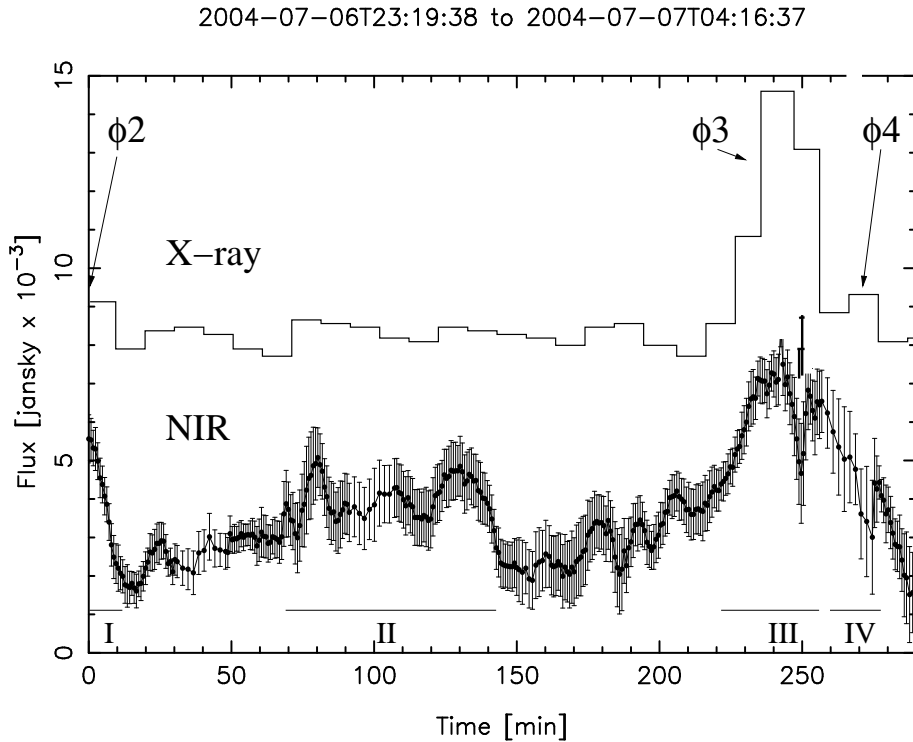


Figure 6.2: The X-ray and near-infrared light curves plotted with a common time axis. (C.f. text and captions of previous figures.) Straight solid lines in the inserted box represent 0.00, 0.01, and 0.02 counts per second levels. The straight dashed line represents the X-ray IQ-state flux density level.

As shown in fig. 6.3 the candidate (but insignificant by itself) weak X-ray flare  $\phi 2$  was covered by near-infrared  $K$ -band measurements starting at its X-ray peak emission and covering the decaying part of the event. This event  $\phi 2$  occurs simultaneously to the significant near-infrared event II, thus justifying its further discussion. The moderately bright X-ray flares  $\phi 3$  and  $\phi 4$  were fully covered in the near-infrared domain as well (see Figs. 6.3 and 6.2). Flare  $\phi 4$  follows immediately after  $\phi 3$  and is similar in total strength and spectral index to  $\phi 2$ . The cross-correlation (fig. B.13) between the X-ray and near-infrared flare emission results in an upper limit for a time lag between both events of about 10 minutes. The graph shows a clear maximum close to zero minutes delay, indicating that both data sets are well correlated within the binning sizes. Between the X-ray/near-infrared flares  $\phi 2$ /I and  $\phi 3$ /III, a lower level near-infrared flaring event, which has no significant counterpart in the X-ray domain, is detected. Finally, the near-infrared flare V (see fig. B.11 lower right corner) was not covered by X-ray data. In table 6.2, a summary of the observed flux densities and spectral indices of all considered events is displayed.

The times at which the flare emission was negligible, i.e. equal to the low level variability IQ-state emission in the X-ray and near-infrared domain, can be estimated. The corresponding full width at zero power (FWZP) and FWHM start and stop times are given in tables 3.5 and 6.1. For the weak candidate flare events  $\phi 1$ ,  $\phi 2$ , and  $\phi 4$  the given FWZP is only estimated. In summary the statistical analysis of the combined X-ray and

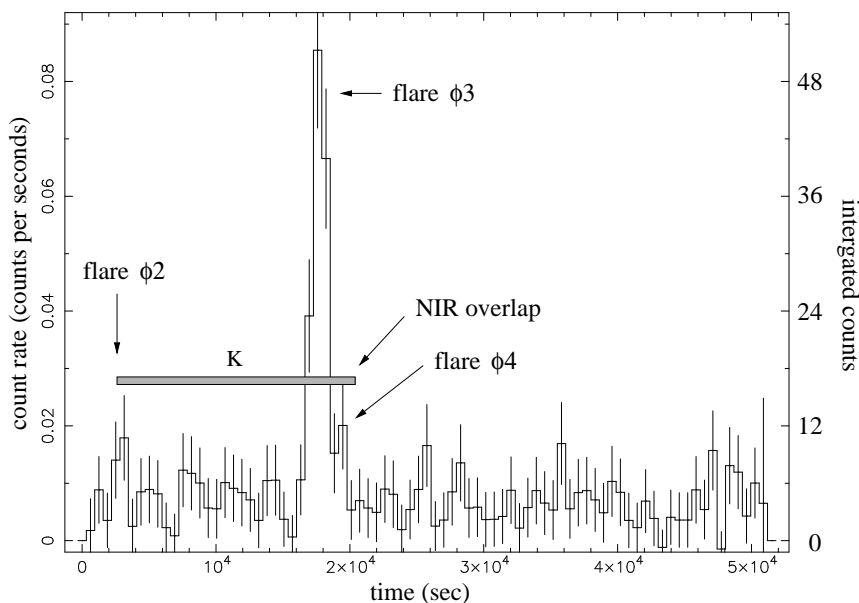


Figure 6.3: Chandra X-ray light curve for 6th/7th July 2005. The overlap with the near-infrared data is also indicated. Start time is 2004 July 6, 22:35:11.8; stop time is 2004 July 7, 12:53:44.9.

near-infrared data for the 2004 observations shows that Sgr A\* underwent at least one significant flare event simultaneously in both wavelength regimes.

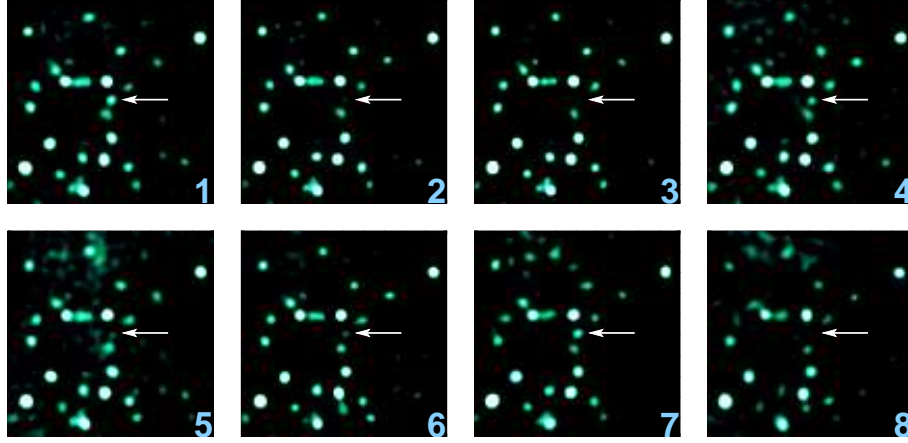


Figure 6.4: *K*-band images of the stellar cluster in the immediate vicinity of Sgr A\*. The numbers correspond to the time points indicated in fig. 3.1. The images result from the average of five individual exposures, corresponding to 150 seconds total integration time. Lucy-Richardson deconvolution and restoration with a Gaussian beam was applied. The color scale is linear. North is up, east to the left. The position of SgrA\* is indicated by the white arrows.

The 890  $\mu\text{m}$  SMA submillimeter light curve (fig. 3.2) does not show any obvious constant flux level, but is instead continuously varying (which is probably the case for the near-infrared emission as well). Several flux density variations of 10 – 20% are visible over the three observing nights, with the variations typically occurring on 1 – 2 hour timescales, although there are also abrupt changes, such as the drop around 09:30 UT on July 6 (SMA 3 in table 6.3). These slow variations occur on somewhat longer timescales than the X-ray and infrared variations. This could be an indication of the 890  $\mu\text{m}$  emission extending out to regions tens of Schwarzschild radii away from the black hole, where causality slows the observed changes in the total flux density integrated over the whole source. However, measurements at 7 mm by Bower et al. (2004) suggest that the source is only 20–30 Schwarzschild radii in diameter, corresponding to only about 10 minutes of light travel time. Consequently, these slow variations are probably not due to propagation effects.

The only period of coincident observations in the infrared and submillimeter domains, 2.5 hours on July 6th, is rather featureless in the submillimeter. Unfortunately, this portion of the infrared observations is not very reliable because very short atmospheric coherence times resulted in poor performance of the adaptive optics (see fig. B.11, upper right from minute 134 onward, and middle left).

A comparison of the submillimeter and X-ray light curves shows that on July 7th the decaying 43 GHz excess is accompanied by a  $\sim 1$  Jy decay of submillimeter flux density (SMA 4 in table 6.3). After a small increase by about 0.5 Jy (SMA 5 in table 6.3), this decay continues over the entire observing period on July 7th (see red squares in the right

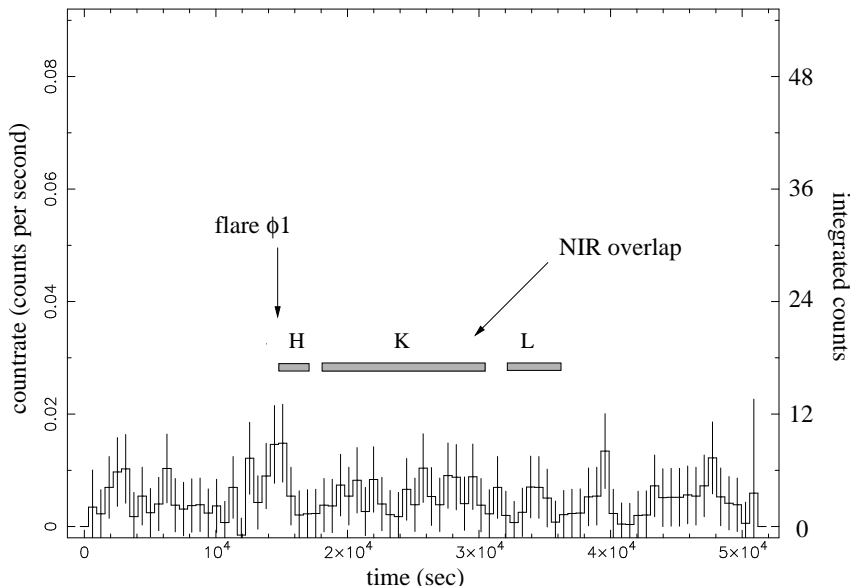


Figure 6.5: Chandra light curve for 5th/6th July 2005. The overlap with the near-infrared data is also indicated. Start time is 2004 July 5, 22:38:25.7; stop time is 2004 July 6, 12:56:58.8.

panel of fig. 3.2) and amounts to a total decrease in flux density of about 2 Jy. Since the observing interval started about 2.3 hours after the X-ray flare  $\phi_3$ /near-infrared flare III, the submillimeter decay may be linked to adiabatic expansion of the emitting plasma, as is speculated in section 6.5.1.

Furthermore the comparison with the X-ray light curve shows that one prominent submillimeter feature, a slow rise over 1.5 hours punctuated by a sharp drop in flux density at 09:30 UT on July 6 (SMA 3 in table 6.3), is coincident with a very small increase in the X-ray flux at 39.4 ks in fig. 6.5. This may indicate that flares observed at shorter wavelengths are preceded by a slow rise in submillimeter emission. Such a slow rise could best manifest itself in the submillimeter domain if the infrared and X-ray regimes are dominated by synchrotron self-compton (SSC) emission, which varies non-linearly with the synchrotron emission. However, the increase in the X-ray count rate discussed here is not very statistically significant.

The 7 mm VLA radio light curves show relatively small variations on July 6th and 8th, with characteristic amplitudes of  $\sim 10\%$ . On July 7th however, the flux density starts higher than on the previous day by about 0.5 Jy, which corresponds to  $\sim 40\%$  of the mean flux density on July 6 (table 6.3). The flux density then declines steadily over the next three hours, reaching a minimum of 1.6 Jy. The mean flux density on July 7th is  $\sim 0.4$  Jy in excess of the average flux density on July 6th and 8th. The July 7th observations covered the time interval about 1.5 to 5 hours after the the peak of X-ray flare  $\phi_3$ /near-infrared

Observing ID	IR Flare ID	$\lambda$	Start	Stop	FWZP [min]	FWHM [min]	peak flux [Jy]
SMA-A	SMA1	890 $\mu\text{m}$	05 JUL 07:00	05 JUL 10:30	210	120	3.5
SMA-A	SMA2	890 $\mu\text{m}$	05 JUL 11:00	$\geq$ 05 JUL 12:10	-	-	$\geq$ 3.2
SMA-B	SMA3	890 $\mu\text{m}$	06 JUL 07:45	06 JUL 10:00	135	$<$ 60	3.4
SMA-C	SMA4	890 $\mu\text{m}$	$<$ 07 JUL 06:00	07 JUL 08:00	-	-	$\geq$ 3.5
SMA-C	SMA5	890 $\mu\text{m}$	07 JUL 08:00	$\geq$ 07 JUL 12:00	-	-	3.3
VLA-B	VLA1	7 mm	$<$ 07 JUL 04:40	$>$ 07 JUL 08:50			$>$ 0.5

Table 6.3: Emission properties of the radio flare events from SgrA\*. In case of detection of a flare event, the estimated peak flux density, the full zero start and stop times, the full zero width at the corresponding zero points (FWZP) and the full width at half maximum of the flare events are given, while the values given for the VLA comprise the excess flux density over the mean flux density measured on July 6th and 8th.

flare III. Given the lack of simultaneous radio observations with the flare peak, the precise relationship between the rise in the radio flux density and the X-ray/near-infrared flare (see section 6.5.1) can only be guessed at. Whether the radio flux density rise precedes or follows the X-ray flare can therefore not be constrained, nor even whether it is related to any hypothetical X-ray flare that may have occurred during the 10 hours between the two Chandra observations.

## 6.2 Flux Densities and Spectral Indices

Consistent with previous *Chandra* observations (Baganoff et al. 2001, 2003; Eckart et al. 2004a) the IQ state X-ray count rate in a 1.5" radius aperture is  $5.3 \pm 0.5 \times 10^{-3}$  counts/s during the monitoring period, corresponding to a 2 - 8 keV luminosity of  $2.2 \times 10^{33}$  erg/s or a flux density of 0.015  $\mu\text{Jy}$ . The excess X-ray flux density observed during the strongest simultaneous flare event  $\phi_3$  was  $0.223 \pm 27$   $\mu\text{Jy}$ , which is about a factor of 15 higher than the IQ state and corresponds to a 2 - 8 keV luminosity of about  $33 \times 10^{33}$  erg/s. For the other three events  $\phi_1$ ,  $\phi_2$ , and  $\phi_4$  the excess flux was only a factor of 1.5 to 2 above the flux of the IQ state. In the infrared the 2.2  $\mu\text{m}$  extinction corrected flux density of the low level variability IQ-state Sgr A\* counterpart was found to be of the order of 3 mJy and the excess flux density observed during the flares was only of the order of 5 mJy.

For the stronger flare  $\phi_3$  a spectral index of  $\alpha_{\text{X/NIR}} \sim 1.12$  (with  $S_\nu \propto \nu^{-\alpha}$ ) is obtained between the near-infrared regime (in this case 2.2  $\mu\text{m}$ ) and the X-ray domain (in this case centered approximately at an energy of 4 keV). For the three weaker flares ( $\phi_1$ ,  $\phi_2$ , and  $\phi_4$ ),  $\alpha_{\text{X/NIR}} \sim 1.35$  is found, which is comparable to the value given for the event reported by Eckart et al. (2004a) (see also table 6.2). This shows that the amplitude range of the X-ray flare emission is larger than that observed in the infrared and that the infrared and X-ray flare strengths are not necessarily proportional to each other. It also suggests that stronger flare events may have a flatter overall spectrum. The fact that the near-infrared spectral indices measured by Eisenhauer et al. (2005) and Ghez et al. (2005) are usually much steeper than the overall X-ray/near-infrared spectral indices is discussed in detail in section 6.5.

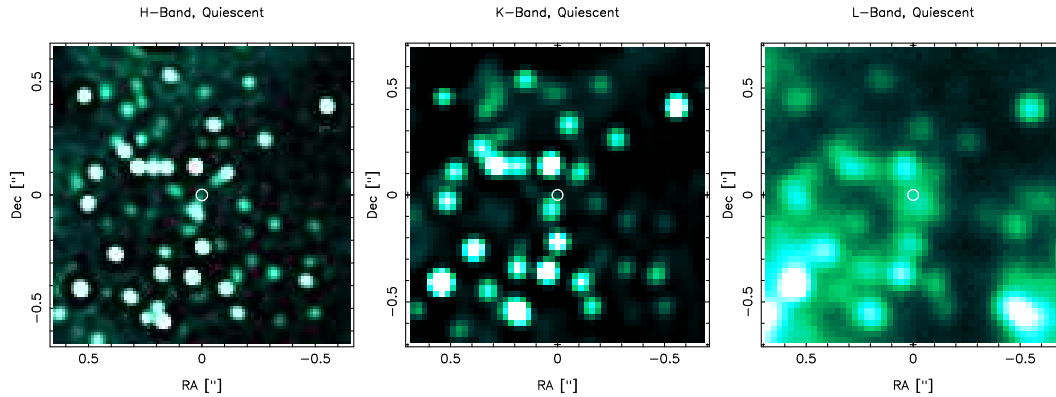


Figure 6.6: Images of the stellar cluster in the immediate vicinity of Sgr A\* during the IQ, low near-infrared flux density state of Sgr A\*. The images result from the average of several individual exposures, corresponding to a total integration time of 40 minutes for  $H$ -band, 100 minutes for  $K$ -band, and 80 minutes for  $L'$ -band. Lucy-Richardson deconvolution and restoration with a Gaussian beam was applied. The color scale is linear. North is up, east to the left. The field of view shown in each image is  $1.3'' \times 1.3''$ . The white circles indicate the position of Sgr A\*. All images were taken on July 6th 2004. The positional accuracy of the images is of the order of 0.5 pixels, i.e.  $\sim 7$  mas in the  $H$ -band and  $\sim 14$  mas in the  $K$ - and  $L'$ -bands.

### 6.3 Constraining the near- and mid-infrared spectrum of Sgr A\*

On July 6th the central region was covered in the near-infrared  $H$ -,  $K$ -, and  $L'$ -bands during a quiescent period with no detectable near-infrared flare emission, with the exception of a short and weak decaying X-ray flare at the beginning of the  $H$ -band exposure (near-infrared flare event I in table 6.1). In fig. 6.6 the corresponding images obtained during this phase in all three near-infrared bands ( $H$ -,  $K$ -, and  $L'$ -band) are presented. These images show that very little emission originates from potential sources at the position of SgrA\*. Both in the  $H$ - and  $K$ -band the flux density may be severely influenced or even dominated by emission due to the stellar background.

The near-infrared spectral energy distribution of the flaring states of Sgr A\* appears to be very red. Using the new integral field spectrometer SINFONI at the VLT, Eisenhauer et al. (2005) obtained simultaneous near-infrared spectral energy distributions ( $\nu L_\nu = \nu^{-\epsilon}$ ) of three flares. They find that the slopes vary and have values ranging from  $\epsilon = 2.2 \pm 0.3$  to  $\epsilon = 3.7 \pm 0.9$  during weak flares of Sgr A\*. This corresponds to a spectral index ( $S_\nu \propto \nu^{-\alpha}$ ) range of about  $\alpha = 3 - 5$ . It is assumed here that the subtraction of spectral data cubes before the flare events by these authors *did* only correct for scattered light/spillover and foreground/background stellar emission along the line of sight toward Sgr A\*, and that the possible contribution of the flare emission to the flux density obtained at these times *before* the flare event is negligible. Under these circumstances, the differential spectral shapes can be regarded as true spectra of the near-infrared flares.

In recent narrow-band measurements with the Keck telescope, Ghez et al. (2005, and

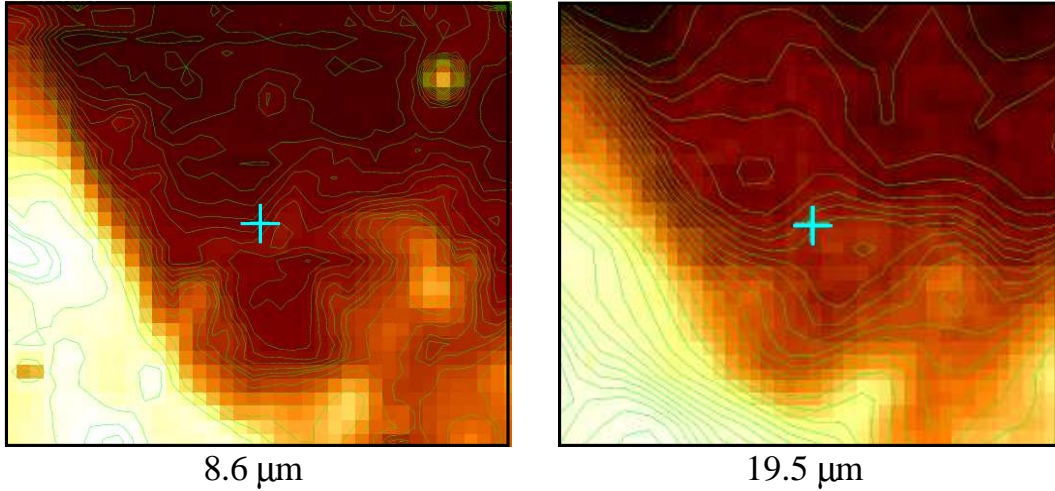


Figure 6.7: 8.6  $\mu\text{m}$  (left) and 19.5  $\mu\text{m}$  (right) image of the central  $5.0'' \times 4.4''$  as observed with VISIR on 8 May 2004. The emission at the position of Sgr A\* is consistent with dust emission similar to what is measured towards other faint components within the central 5-10''. The cross marks the position of Sgr A\* and the positional uncertainty of  $\pm 0.2''$ . As reference sources to determine the relative positioning between the near-infrared and mid-infrared frame the following bright and compact sources were used: IRS 3, 7, 21, 10W and additionally IRS 9, 6E and 29 at 8.6  $\mu\text{m}$ .

private communication) also found a red intrinsic flare spectrum. These measurements, however, indicate a considerably flatter spectrum with a slope of  $\alpha = 0.5 \pm 0.3$ .

### 6.3.1 Contamination by Mid-Infrared Dust Emission

The images at wavelengths longer than 2.2  $\mu\text{m}$  show the existence of a flux density contribution from a weak and extended source D1 with a separation ranging between  $\sim 0.03''$  and  $\sim 0.15''$  from Sgr A\* (i.e.  $0.08'' \pm 0.05''$ , see figs. B.14 and 6.7; see also Ghez et al. 2004a, 2005). The FWHM diameter of this source D1 is of the order of 1400 AU at the distance of 8 kpc. In addition to the overall contribution of the minispiral to the dust emission there are several other red features of this kind (labeled D2 to D8 in fig. B.14) within the central  $2.6'' \times 2.6''$  region. At 8.6  $\mu\text{m}$ , source D1 appears to be part of a larger ridge structure tracing lower temperature dust (see also Stolovy et al. 1996) at a position angle similar to a feature along an extension of dust emission from the minispiral towards the central cluster of high velocity stars (see fig. B.14). This ridge continues further to the northwest and it seems therefore likely that the emission component close to Sgr A\* is part of this extension. This component is thus probably due to continuum emission of warm dust. Deriving the flux density of this extended source D1 is difficult, as it is located in a crowded field and will therefore be confused with the  $L'$ -band counterpart of Sgr A\*. Using an  $L'$ -band magnitude of  $m_{L'} = 12.78$  for S2 (Ghez et al. 2005; Clénet et al. 2005) and following the approach of Ghez et al. (2005) of subtracting all neighboring

point sources, the location, extent, and overall shape of this extended component can be confirmed (fig. B.15). Since no activity of Sgr A\* was indicated by the  $H$  and  $K$  band exposures before and the X-ray exposure during the  $L'$ -band imaging on July 6th (see table 3.1), it is likely that Sgr A\* was in a low state. On July 6th the  $L'$ -band brightness of Sgr A\* was  $m_{L'} = 14.1 \pm 0.2$  (about 3.7 mJy dereddened), which is about half a magnitude brighter than what is reported by Ghez et al. (2005) and is consistent with Sgr A\* having been in a low flux density state during the  $L'$ -band exposures. Within the uncertainties in subtracting the neighboring sources (including Sgr A\*) the data is consistent with an integrated  $L'$ -band magnitude of  $m_{L'} \sim 12.8$  for the extended dust component, which is about 0.9 magnitudes brighter than that given by Ghez et al. (2005), i.e. the extended source D1 is almost as bright as the star S2. This would be consistent with a structure that is extended on scales larger than 100 milliarcseconds (see  $L'$  band magnitudes given in the caption of fig. B.15), to which the VLT telescope beam – with adaptive optics – couples slightly better than the beam of the Keck telescope. A brightness of  $m_{L'} = 12.8 \pm 0.2$  corresponds to a dereddened ( $m_{\text{ext}} = 1.8$ ) flux density of about  $12 \pm 3$  mJy.

If the extended component D1 is associated with a gas and dust feature of the Galactic center interstellar medium, the  $8.6 \mu\text{m}$  flux density limit is most likely also contaminated by emission from this extended dust feature. Assuming that this feature is not associated with Sgr A\* and that it has physical properties similar to the other dust emission components in the central parsec, its contribution to the  $8.6 \mu\text{m}$  emission can be approximated by using its flux density value obtained in the  $L'$ -band and a mean flux density ratio between  $8.6 \mu\text{m}$  and  $3.8 \mu\text{m}$  obtained for the  $\sim 200 - 400$  K warm dust (Cotera et al. 1999). From the available  $L'$ - and  $N$ -band images this flux density ratio is derived as approximately 3 on individual warmer sources (such as IRS 21) and approximately  $12 \pm 4$  on the overall region (derived from the data and consistent with the ISO spectrum shown by Lutz et al. 1996) which is dominated by the flux density contribution of the extended mini-spiral. From the  $L'$ -band flux density estimate of this component it becomes clear that it can easily account for most of the  $8.6 \mu\text{m}$  flux density at the position of Sgr A\* within the uncertainties. Similarly, a flux density ratio between  $19.5 \mu\text{m}$  and  $8.6 \mu\text{m}$  of about  $7 \pm 2$  is measured on the mini-spiral, which is also consistent with Lutz et al. (1996). The flux densities obtained at the position of Sgr A\* at  $8.6 \mu\text{m}$  and  $19.5 \mu\text{m}$  are consistent with the emission being due to dust with similar properties to that found in the mini-spiral.

In figs. B.16 and B.17 the flux densities – or their upper limits – towards Sgr A\* are shown, expressed via the energy output  $\nu L_\nu$  as a function of frequency  $\nu$ . The plots cover the wavelength range between  $30 \mu\text{m}$  and  $1.6 \mu\text{m}$ . In the mid-infrared ( $\lambda \geq 8.6 \mu\text{m}$ ) only upper flux density limits are available. For the near-infrared  $K$ -band the envelope of the spectral data obtained by Eisenhauer et al. (2005); Ghez et al. (2005) has been plotted. For the  $L'$ -band, the obtained value of the low level variability (IQ) flux densities is compared to the corresponding data intervals given by Genzel et al. (2003) and Ghez et al. (2004b, 2005) (see caption of fig. B.16).

It seems likely that the  $L'$ -band IQ state continuum emission obtained for Sgr A\* is also effected to a small extent by a contribution from the weak, extended emission component (see figs. B.14 and 6.7). This contribution depends critically on the aperture used and the precise location of the red emission component with respect to Sgr A\*. For the high angular resolution  $L'$ -band images it is estimated that this contribution cannot be larger than a few mJy. For the  $8.6 \mu\text{m}$  band the flux density limit obtained from the VISIR commissioning data is lower than the (dereddened) value of  $\sim 100$  mJy derived by Stolovy et al. (1996). The values obtained by Telesco et al. (1996) and Serabyn et al. (1997) most



likely also include continuum emission contributions associated with dust components in the central parsec.

Extrapolating the SINFONI spectral slopes towards lower frequencies, their predicted flux densities lie within or above the quiescent state fluxes obtained in the  $L'$ -band by Genzel et al. (2003); Ghez et al. (2004b) and the value reported in this paper. Given that the data at longer wavelengths, including those at  $8.6 \mu\text{m}$ , only represent upper limits of the flux densities of Sgr A\*, the predicted values obtained by an extrapolation of the steep  $K$ -band spectra lie well above these limits and thus the expected intrinsic energy output of Sgr A\*. This is especially true if a flux density level equivalent to the quiescent state were to be added back to the flare spectroscopy data. While it is not known whether the mid-infrared data were obtained during a low level flux density (IQ) or a flare state, and the possibility exists in principle that Sgr A\* becomes very bright in the mid-infrared regime during a flare, Sgr A\* has been observed frequently during the past two decades and strong flare activity has never been reported to date at mid-infrared wavelengths. In total, the combination of the very steep flare spectra and the low flux density limits of Sgr A\*, especially at  $8.6 \mu\text{m}$  and longward, imply that the intrinsic spectral energy distribution of Sgr A\* flattens significantly for wavelengths longer than approximately  $4 \mu\text{m}$ .

## 6.4 Near-infrared and X-Ray Flares

The durations of the flares found in the observations presented here are in agreement with current statistics: Baganoff et al. (2001); Eckart et al. (2004a); Porquet et al. (2003) report on X-ray events of 45 to 170 minutes, while Eckart et al. (2004a); Ghez et al. (2004b); Genzel et al. (2003) report on near-infrared flare events lasting 50 to 80 minutes, respectively. Simultaneous observations indicate that the near-infrared and X-ray flare events are well correlated in duration.

In the following it will be assumed as a working hypothesis that the activity of Sgr A\* consists of consecutive flare events of variable strength that have a characteristic duration of the order of 100 minutes. It is further assumed that both the flare event rate, i.e. the number of flares of a given strength per day, and the flare event strength can be described by a power-law. (Deviations from this assumption are discussed towards the end of this section.)

From the flare statistics and the near-infrared flux density monitoring that has been compiled over the past decade one can assume a power-law representation that allows the prediction of the flare event rate. It is natural to assume that this power-law will be truncated at both ends. At the high end this can be justified by the fact that infrared flares much stronger than the neighboring high velocity “S-stars” have never been observed, and that an accretion process within a characteristic time scale must have a limited radiative efficiency. A truncation at the low end can be justified by the (currently) continuous supply of stellar wind material from the He-stars within the central 0.2 pc of the stellar cluster.

Based on the measurements of 2003, the estimated infrared flaring rate is very high: four infrared flare events were found within a total of 25 hours of observations, resulting in about two to six events per day when assuming Poisson statistics (Genzel et al. 2003). The recent observations presented here cover a total of 0.71 days, revealing four infrared flare events, two of which are above 5 mJy. The rate of near-infrared (i.e. mostly  $K$ -band) flares with a strength of approximately  $10 \pm 5 \text{ mJy}$  of  $4 \pm 2$  per day can therefore be confirmed. This leads to a rate of flares that are weaker than about 5 mJy of  $10.4 \pm 2$  per

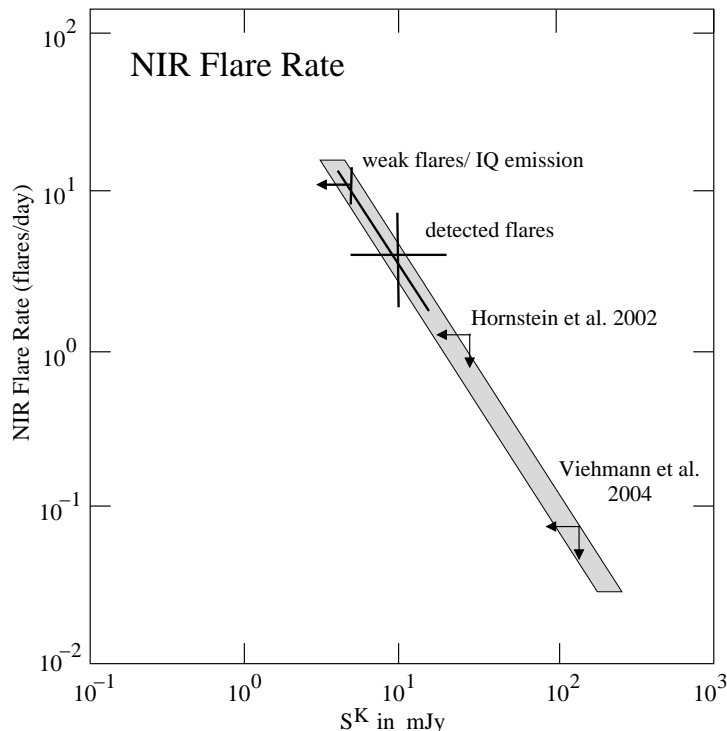


Figure 6.8: Flare amplitude as a function of flare rate for the near-infrared emission from Sgr A\*, assuming that the characteristic flare duration is of the order of 100 minutes.

day (obtained by dividing the remainder of 24 h that was not covered by  $> 5$  mJy flares by the characteristic flare duration). Here the IQ state is included, assuming that it can be represented by weak, consecutive flares of the same average length of 100 minutes.

As for stronger flares, Hornstein et al. (2002) find from the analysis of high angular resolution  $K$ -band imaging obtained with the Keck telescope that the probability that an infrared flare event of 3 hour duration has occurred with a flux density in excess of 19 mJy is *at most* 9%, corresponding to an equivalent flare rate of  $\leq 0.7$  events of 3 hour duration per day or  $\leq 1.3$  flares per day assuming a flare duration of 100 minutes. For the shorter duration, the detection flux level is increased by  $\sqrt{2}$  to 27 mJy. Performing a similar analysis for ISAAC data, Viehmann et al. (2004); Eckart et al. (2003c) find a likelihood of 0.5% for 3 hour flares with a flux density of more than 100 mJy. The equivalent flare rates for this case are  $3.6 \times 10^{-2}$  for 3 hour flares and  $7.2 \times 10^{-2}$  for 100 minute flares, per day. As before, the detection flux level is increased by  $\sqrt{2}$  to 141 mJy for the shorter assumed flare length of 100 minutes. These quantities are plotted in fig. 6.8. The data can be described by a power-law of the form  $N = \kappa_0(A)^{-\zeta} \kappa_1 \kappa_2$ . Here the quantities  $\kappa_0$  and  $N$  are in units of flare events per 24 hours, and  $\kappa_1 = \exp(-\frac{A}{A_{\text{high}}})$  and  $\kappa_2 = \exp(-\frac{A_{\text{low}}}{A})$  allow for a truncation of the power-law towards strong and weak flare events.  $A_{\text{high}}$  and  $A_{\text{low}}$  are cutoff flux densities at the high and low end of the power-law, respectively. Treating the limits as real measurements reveals  $\zeta = -1.4 \pm 0.2$  and  $\kappa_0 = 100 \pm 30$ . If the assumption that the flare length is independent of the flare amplitude has to be modified, it should be noted that the following statements apply: If the overall characteristic flare duration is shorter or longer than 100 minutes then the power-law will be largely unaffected. It

would still pass through the point given by the detected flares. Since the flare rate would be higher and the flare fluxes lower, changing the flare duration would correspond to a shift along the power-law line. If the flare duration were shorter only for weaker flares then the power-law could be extended towards the top. If stronger flares were to become longer, their rate would go down resulting in a steeper slope of the power-law. Similarly if the flare duration were shorter for stronger flares then the slope would be shallower. An alternative to the truncated power-law representation that can currently not be ruled out is that the involved quantities like flare event rate, length, and strength are represented by peaked functions like a Gaussian.

It is highly improbable that the observed variability is due to stellar sources because of the extremely short time scales of the flares and because of the astrometric positions of the flares, which are within less than 10 milliarcseconds of Sgr A\* at all times (see also table 3.3): a star close to Sgr A\* would have moved by  $\sim 20 - 50$  milliarcseconds during the time interval covered by e.g. the four flares reported by Genzel et al. (2003). A star at greater distances from Sgr A\* would have an extremely low probability of being located so close in projection to Sgr A\*.

Concerning the relation between the near-infrared flares and the X-ray variability of Sgr A\*, the durations, rise, and decay times are similar (see e.g. Baganoff et al. 2001; Porquet et al. 2003). During the *Chandra* monitoring in 2002, however, the near-infrared flare rate was almost twice as high as the X-ray flare rate. The range in spectral luminosities of the X-ray flares also appears to be larger than in the near-infrared (including the brightest X-ray flares). X-ray flares that are a factor of  $>10$  stronger than the quiescent emission occur at a rate of  $0.53 \pm 0.27$  per day, while weaker flares are seen at a rate of  $1.2 \pm 0.4$  (Baganoff et al. 2003). Flares in the X-ray domain have been observed since 2000 (Baganoff et al. 2001, 2003; Eckart et al. 2003c, 2004a; Porquet et al. 2003) and only since 2003 in the near-infrared domain (Genzel et al. 2003; Ghez et al. 2004b; Eckart et al. 2004a). Consequently, further simultaneous observations are necessary to determine the relation between the X-ray and near-infrared flares.

## 6.5 Interpretation

The new simultaneous X-ray/near-infrared flare detections of the Sgr A\* counterpart presented here support the finding by Eckart et al. (2004a) that it is the same population of electrons that is responsible for both the infrared and the X-ray emission (at least for the observed flares). The short flare duration indicates that the flare emission most likely originates from compact source components. The spectral energy distribution of Sgr A\* is currently explained by models invoking *radiatively inefficient accretion flow* processes (RIAF: Quataert 2003; Yuan et al. 2002, 2003, 2004), including advection dominated accretion flows (ADAF: Narayan et al. 1995), convection dominated accretion flows (CDAF: Ball et al. 2001; Quataert & Gruzinov 2000; Narayan et al. 2002; Igumenshchev 2002), advection-dominated inflow-outflow solutions (ADIOS: Blandford & Begelman 1999), jet models (Markoff et al. 2001), and Bondi-Hoyle models (Melia & Falcke 2001). Combinations of such models, such as an accretion flow plus an outflow in form of a jet are also considered (e.g. Yuan et al. 2002).

### 6.5.1 Description and Properties of the SSC Model

Current models (Markoff et al. 2001; Yuan et al. 2002, 2003, 2004; Liu et al. 2006) predict that during a flare a few percent of the electrons near the event horizon of the central black hole are accelerated. These models give a description of the entire electromagnetic spectrum of Sgr A\* from the radio to the X-ray domain. In contrast, this analysis is limited to modeling the near-infrared to X-ray spectrum of the most compact source component at the location of Sgr A\*. A simple synchrotron self-compton (SSC) model was employed to describe the observed radio to X-ray properties of Sgr A\* using the nomenclature given by Gould (1979); Marscher (1983). Inverse Compton scattering models provide an explanation for both the compact near-infrared and the X-ray emission by up-scattering submillimeter-wavelength photons into these spectral domains. Most of the recent modeling approaches consider the possibility of such models, which therefore may provide important insights into some fundamental model requirements. These models do not explain the entire low frequency radio spectrum or the IQ state X-ray emission, however, they deliver a description of the *compact* IQ state and flare emission originating from the immediate vicinity of the central black hole. A more detailed explanation is given by Eckart et al. (2004a).

We assume a synchrotron source of angular extent  $\theta$ . The source size is of the order of a few Schwarzschild radii  $R_s = 2GM/c^2$  with  $R_s \sim 10^{10}$  m for a  $3.6 \times 10^6 M_\odot$  black hole. One  $R_s$  then corresponds to an angular diameter of  $\approx 8$  microarcseconds at a distance to the Galactic center of 8 kpc (Reid 1993; Eisenhauer et al. 2003). The emitting source becomes optically thick at a frequency  $\nu_m$  with a flux density  $S_m$ , and has an optically thin spectral index  $\alpha$  following the law  $S_\nu \propto \nu^{-\alpha}$ . This allows us to calculate the magnetic field strength  $B$  and the inverse Compton scattered flux density  $S_{\text{SSC}}$  as a function of the X-ray photon energy  $E_{\text{keV}}$ . The synchrotron self-Compton spectrum has the same spectral index as the synchrotron spectrum that is up-scattered i.e.  $S_{\text{SSC}} \propto E_{\text{keV}}^{-\alpha}$ , and is valid within the limits  $E_{\text{min}}$  and  $E_{\text{max}}$  corresponding to the wavelengths  $\lambda_{\text{max}}$  and  $\lambda_{\text{min}}$  (see section 2.4 or Marscher 1983 for further details). We find that Lorentz factors  $\gamma_e$  for the emitting electrons of the order of typically  $10^3$  are required to produce a sufficient SSC flux in the observed X-ray domain. A possible relativistic bulk motion of the emitting source results in a Doppler boosting factor  $\delta = \Gamma^{-1}(1 - \beta \cos \phi)^{-1}$ . Here  $\phi$  is the angle of the velocity vector to the line of sight,  $\beta$  the velocity  $v$  in units of the speed of light  $c$ , and Lorentz factor  $\Gamma = (1 - \beta^2)^{-1/2}$  for the bulk motion. Relativistic bulk motion is not a necessity to produce sufficient SSC flux density but we have used modest values for  $\Gamma = 1.2 - 2$  and  $\delta$  ranging between 1.3 and 2.0 (i.e. angles  $\phi$  between about  $10^\circ$  and  $45^\circ$ ) since they will occur in case of relativistically orbiting gas as well as relativistic outflows – both of which are likely to be relevant in the case of Sgr A\*.

An additional feature of the model is that it allows to provide an estimate of the extent of the pure synchrotron part of the spectrum by giving the upper cutoff frequency  $\nu_2$  of that spectrum as a function of source parameters including the maximum  $\gamma_e$  of the relativistic electrons. Explaining the X-ray flare emission by a pure synchrotron model requires a high energy cutoff in the electron energy distribution with large Lorentz factors for the emitting electrons of  $\gamma_e > 10^5$  and magnetic field strengths of the order of 10-100 G (Baganoff et al. 2001; Markoff et al. 2001; Yuan et al. 2004). This corresponds to short cooling time scales of less than a few hundred seconds, which would then require *repeated* injections or accelerations of such energetic particles (Baganoff et al. 2001; Markoff et al. 2001; Yuan et al. 2004). It therefore appears more likely that with  $\gamma_e \sim 10^3$ , the cutoff frequency  $\nu_2$

comes to lie within or just shortward of the near-infrared bands, such that a considerable part of the near-infrared spectrum can be explained directly by synchrotron emission, and the X-ray emission by inverse Compton emission. This assumption is supported by SSC models presented by Markoff et al. (2001); Yuan et al. (2003), which result in a significant amount of direct synchrotron emission in the infrared (see also synchrotron models in Yuan et al. 2004 and discussion in Eckart et al. 2004a).

### 6.5.2 Modeling Results

In the following it is assumed that the dominant submillimeter-emitting source component responsible for the observed flares has a size of the order of one to a few Schwarzschild radii and a turnover frequency  $\nu_m$  ranging from about 100 GHz to 1000 GHz. Eckart et al. (2004a) have shown that (at least) the weaker flares can be described via a contribution of pure SSC emission both at near-infrared and X-ray wavelengths. The corresponding magnetic field strengths are of the order of 0.3 to 40 Gauss, which is within the range of magnetic fields expected for RIAF models (e.g. Markoff et al. 2001; Yuan et al. 2003, 2004). The required flux densities  $S_m$  at the turnover frequency  $\nu_m$  also lie well within the range of the observed variability of Sgr A\* in the mm-domain (Zhao et al. 2004, 2003). In this section, a few models consisting of a mixed contribution of simple synchrotron and SSC emission are presented. With these models it is possible to describe both the low near-infrared/X-ray flux density state (IQ state) as well as the very red near-infrared flare spectra.

#### Newly observed near-infrared/X-ray flares

While near-infrared *in-band* spectra of the flare events reported here are not available, the available information on the *K*-band spectral indices must be taken into account. Red and variable near-infrared spectra are expected from most model calculations (e.g. Markoff et al. 2001; Yuan et al. 2004), and they are also compatible with the interpretation in the framework of a simple SSC model as described above (see Eckart et al. 2004a). According to Eisenhauer et al. (2005), Sgr A\* apparently has very red near-infrared in-band spectra during the flaring phases. Combined with the low flux density limits at wavelengths longwards of the *L'*-band this implies a significant flattening of the spectrum of Sgr A\* in the 4 to 10  $\mu\text{m}$  range during these infrared flare events. It is assumed here that the mid-infrared flux densities are valid independently of whether or not Sgr A\* is in a flaring state or not. This implied spectral flattening suggests that a synchrotron component that experiences an exponential cutoff in the near- to mid-infrared wavelength range is responsible for a significant proportion of the flare state luminosity of Sgr A\*.

Two plausible, representative flare state models are listed in table 6.4 and plotted in fig. B.17. In both models synchrotron radiation is produced up to frequencies of 200 THz, i.e. just shortward of the near-infrared *H*-band. It is assumed that this cutoff is caused by an exponential cutoff in the energy spectrum of the relativistic electrons. This will result in a modulation of the intrinsically flat spectra (i.e.  $\alpha = 0.8 - 1.3$ ) with an exponential cutoff proportional to  $\exp[-(\nu/\nu_0)^{0.5}]$  (see e.g. Bregman 1985; Bogdan & Schlickeiser 1985) and a cutoff frequency  $\nu_0$  that lies in the 4 - 20  $\mu\text{m}$  wavelength range. Such a cutoff could be caused by synchrotron losses at the high end of the relativistic electron spectrum. Small variations in such an exponential damping of the radiation provide *variable*, red flare spectra. Within the uncertainties, models like F1 or F2 reproduce the near-infrared/X-ray properties of the observed flare  $\phi 1/\text{III}$  (see table 6.4) very well. Both model F1 and

model ID	$S_{\text{NIR synchr.}}$ [mJy]	$S_{\text{NIR SSC}}$ [mJy]	$S_{\text{X-ray}}$ [nJy]	B [G]	$\nu_{\text{max}}^{\text{obs}}$ [GHz]	$S_{\text{max}}^{\text{obs}}$ [Jy]	$\theta$ [ $\mu\text{as}$ ]	$\alpha_{\text{NIR/X-ray}}$	$c/\nu_0$ [ $\mu\text{m}$ ]
IQ1	0.8	2.0	<18	17	820	3.9	7.9	1.3	-
IQ2	-	3.0	<27	5	820	7.7	8.1	1.3	-
IQ3	(25) 1	0.1	<17	80	1000	16.0	17.5	1.0	15
IQ4	2.0	0.02	<15	38	1500	0.33	1.5	0.8	-
F1	(18) 6	1.13	65	68	1640	11.5	8.5	1.1	5
F2	(300) 6	0.1	230	100	1640	5.7	8.5	0.4	90

Table 6.4: Parameters for representative models in agreement with the IQ (IQ1-IQ4) and flare states (F1 and F2) observed towards Sgr A\*. These models are plotted in figs. B.16 and B.17. Listed are the near-infrared flux density contributions from the synchrotron and SSC part of the spectrum as well as the SSC X-ray flux density (columns 2 to 4). The following columns list the magnetic field strength  $B$ , observed cutoff frequency  $\nu_{\text{max}}^{\text{obs}}$  and flux density  $S_{\text{max}}^{\text{obs}}$  of the synchrotron spectrum, size  $\theta$  of the source component and the spectral index  $\alpha$  of the synchrotron component. All models except IQ2 provide synchrotron emission for frequencies up to  $\nu_2 \sim 200$  THz. It is assumed that the cutoff in the energy spectrum of the relativistic electrons can be represented via an exponential cutoff in the observed synchrotron spectrum, proportional to  $\exp[-(\nu/\nu_0)^{0.5}]$  with the effective cutoff frequency  $\nu_0$ . If applicable, the near-infrared flux densities in the first column are given without (in brackets) and with modulation by this exponential cutoff.

the pure SSC model presented in Eckart et al. (2004a) could represent flare  $\phi 2$  and  $\phi 4$ . Flare  $\phi 1$ , which was not detected in the  $H$ -band, is consistent with flares  $\phi 2$  and  $\phi 4$ , and with the indication that the flare emission is intrinsically very red (Eisenhauer et al. 2005). Ghez et al. (2005) suggest that the near-infrared spectral index is a function of near-infrared flare brightness, with weak flares ( $\sim 2$  mJy or less at  $2.2 \mu\text{m}$  – comparable to  $\phi 1$ ) having steep intrinsic near-infrared spectra ( $\alpha \sim 4$ ), and brighter flares ( $\geq 6$  mJy at  $2.2 \mu\text{m}$  – comparable to  $\phi 3$ ) having *flatter* intrinsic near-infrared spectra ( $\alpha \sim 0.5$ ). In this context an exponential cutoff as described above would be required for weak flares, while the intrinsic spectral indices for brighter flares in the models (see table 6.4) are much closer to the spectral index derived by Ghez et al. (2005).

The model results show that synchrotron spectra that are intrinsically very flat (i.e.  $\alpha \leq 0.5$ ) result in a large discrepancy between the measured and the predicted X-ray and near-infrared flux densities and large magnetic fields, unless a spectral cutoff in the 50 - 100  $\mu\text{m}$  range is introduced, which makes the spectra significantly steeper again in the near-infrared regime. Smaller source sizes and higher turnover frequencies  $\nu_m$  of a few 1000 GHz also result in very large ( $>100$  G) magnetic fields.

### Low flux density IQ state of Sgr A\*

The X-ray flux density over the central  $0.6''$  radius is due to extended thermal bremsstrahlung from the outer regions of an accretion flow ( $R > 10^3 R_S$ ; see Baganoff et al. 2001, 2003; Quataert 2003). The *compact* X-ray emission in the “interim-quiescent” (IQ) low-level flux density states of Sgr A\* can be explained by an SSC model that allows for substantial contributions from both the self-compton upscattered and the pure synchrotron part of the modeled spectrum. In these models the X-ray emission of the point source is well below 20 - 30 nJy and contributes much less than half of the X-ray flux density during the weak flare event reported by Eckart et al. (2004a). The flux densities at  $2.2 \mu\text{m}$  wavelength are of the order of the observed values of 1 to 3 mJy during the IQ state, which is in full agreement with a state of low level flux density variation. Representative models for the low flux state are listed in table 6.4 and plotted in fig. B.16. For models IQ1 to IQ3 the source component has a size of the order of one to two Schwarzschild radii with an optically thin radio/sub-mm spectral index  $\alpha_{\text{NIR/X-ray}}$  ranging approximately from 1.0 to 1.3, a value similar to that observed between the near-infrared and the X-ray domain. For models IQ1 and IQ2 (see table 6.4), the upper cutoff frequency  $\nu_2$  of the synchrotron spectrum lies just within or just shortward of the observed near-infrared bands. These SSC IQ state models here represent lower bounds to the measured flux density limits at the position of Sgr A\*. Model IQ3 shows that a longer wavelength cutoff in the mid-infrared results in steep near-infrared spectra like those observed by Eisenhauer et al. (2005) and Ghez et al. (2005). Model IQ3 is also in agreement with the low  $L'$ -band flux densities reported by Ghez et al. (2005) and in this thesis.

Model IQ4, in which no near-infrared/X-ray cutoff is involved, shows that relatively blue spectra may also occur for the low flux state. In this model, the flare radiation originates predominantly from a pure synchrotron component that is smaller than a fraction of a Schwarzschild radius.

### Modeling of the millimeter and submillimeter radio data

The observations of simultaneous near-infrared and X-ray flare emission suggest a source size of the order of one Schwarzschild radius  $R_S$  for the flares, while the measured source

size at radio wavelengths is of the order of 20 - 30  $R_S$ , corresponding to 160 - 240 microarcseconds at 43 GHz (Bower et al. 2004). It cannot be excluded that this is purely due to some opacity structure that makes the source size much larger at longer wavelengths, however, it may also be consistent with the assumption that the source responsible for the near-infrared emission expands as it cools. Such a scenario is actually supported by the quasi-simultaneous mm to X-ray observations of bright flare emission presented here. If the assumption that the X-ray flare  $\phi 3$  and the near-infrared flare III are physically associated with the decaying radio and submm flux density excess detected 1-2 hours later with the VLA and the SMA is valid, the corresponding radio decay timescale of a few hours and its amplitude should be accounted for by a consistent model (like the one presented below).

The models in table 6.4 produce very little ( $< 10$  mJy at 43 GHz) instantaneous flux density at frequencies below the peak frequency of the flare. Motivated by the overall shape of the spectrum of Sgr A\*, the following assumptions are made: A THz peaked flare model like F1 or F2, a self-absorbed synchrotron spectrum at lower frequencies, and adiabatic expansion of the synchrotron emitting flare component via (van der Laan 1966)

$$S(\nu_2) = S(\nu_1)[\nu_1/\nu_2]^{-(7\gamma_e+3)/(4\gamma_e+6)}.$$

The radio flux density will then first rise and later drop as the source evolves, as indicated by the radio data following  $\phi 3$  and  $\phi 4$  on July 7th (in comparison to the radio data of the previous day). Here  $\gamma_e$  is given via the spectral index of the optically thin part of the synchrotron spectrum:  $\alpha = (\gamma_e - 1)/2$ . Then with  $\alpha \approx -1.0$  the peak flux density of  $S(\nu_1) = 11$  Jy at  $\nu_1 = 1.0$  to 1.6 THz relates to a peak flux density of about  $S(\nu_2) = 0.1$  to 0.2 Jy at  $\nu_2 = 43$  GHz and  $S(\nu_2) = 1.5$  to 2.6 Jy at  $\nu_2 = 340$  GHz (i.e. 890  $\mu\text{m}$ ). At  $\nu_2 = 340$  GHz the flux density should then drop by about 0.5 Jy, which is very comparable to what has been observed with the SMA. These flux density contributions represent a major proportion of the observed radio and submm excess emission on July 7th. Adiabatic expansion would also result in a slower decay rate and a longer flare timescale at lower frequencies, as has been observed: less than an hour at near-infrared/X-ray wavelengths and more than 3.6 hours in the radio domain.

As the source of the flare expands it cools in accordance with the synchrotron cooling time scale. This can be calculated via

$$t_s \sim 3 \times 10^7 \Gamma \delta^{0.5} \nu_9^{-0.5} B^{-3/2},$$

where  $t_s$  is in seconds,  $B$  is in Gauss,  $\nu_9$  is in GHz, and  $\gamma$  and  $\Gamma$  are the relativistic factors for the bulk motion of the material (Blandford & Konigl 1979). The corresponding synchrotron cooling times at 1.6 THz, 340 GHz, and 43 GHz for  $B = 68$  G with  $\Gamma \sim \delta \sim 1.5$  are about 1, 1.8, and 4 hours, respectively, which matches well to the observed flux densities and decay time scales.

If the emission originates from relativistically orbiting material, then the source may expand, starting as a compact 8.5 microarcseconds angular radius source, over the entire orbit with a  $\sim 200$   $\mu\text{as}$  angular radius. This will probably occur at a velocity close to sound speed  $c/\sqrt{3}$  (Blandford & McKee 1977), implying a time scale of approximately 2 hours. Visualizing the emitting source as a component in a freely expanding jet, the expansion from a source of 8.5 microarcseconds angular radius to 240 microarcseconds angular radius at a speed  $c/\sqrt{3}$  will take approximately 14 minutes. Within the given



assumptions the model of relativistically orbiting material gives a more suitable representation of the observed flux densities and decay time scales – *unless* the possible jet is foreshortened due to being pointed at the observer.

The comparison of models F1 and F2 with the near-infrared data also indicates that the very steep spectral slopes found by Eisenhauer et al. (2005) are most probably linked to flare events that do not produce a significant amount of SSC radiation in the near-infrared. These flares, which would probably be caused by a less energetic population of relativistic electrons, would then be dominated by the exponentially decaying direct synchrotron component, rather than a contribution of inverse Compton radiation (which is due to a more energetic population of relativistic electrons).



# Appendix A

## Long Tables

Table A.1: Photometry of sources detected in NAOS/CONICA and ISAAC images. The classifications are from Blum et al. (1996), with “cool” referring to red giants or supergiants and “red” signifying objects with featureless  $K$ -band spectra and a strong IR excess. The zero-point for the positions is 17:45:42.93 RA -29:00:29.91 DEC (IRS 16NE) in the J2000 coordinate system, with an offset of 2.83” (RA) and  $-0.91$ ” (DEC) from Sgr A\*.

ID	Name	$\Delta\alpha$ (")	$\Delta\delta$ (")	$H$	$K$	$L$	$M$	$H - K$	$K - L$	$L - M$	Notes
50	IRS 30E	-8.59	4.81	13.12	10.33	8.84	9.12	2.80	1.48	-0.28	
102	IRS 9	2.67	-7.51	11.78	9.41	6.89	6.90	2.38	2.52	-0.02	cool
179		-0.56	-1.25	14.54	12.40	9.08	8.09	2.14	3.32	0.99	
181	IRS 30W	-9.40	5.17	12.86	10.21	8.76	8.87	2.65	1.45	-0.12	
187	IRS 29	-4.51	0.50	14.16	10.36	6.90	6.31	3.81	3.45	0.59	WC9
197		1.69	-4.53	13.15	11.30	10.17	9.99	1.85	1.13	0.18	
200		-7.53	-9.83	14.46	12.09	10.65	>12.73	2.37	1.44	-3.08	
202	IRS 14SW	-3.33	-10.02	11.83	9.56	8.23	8.54	2.27	1.33	-0.31	cool
277	IRS 16C	-1.79	-0.49	11.70	9.64	8.07	7.78	2.06	1.57	0.29	He I
373		-11.42	6.48	13.02	>17.66	8.97	9.24	-5.64	9.69	-0.27	
376		-1.45	-2.44	13.76	10.84	8.92	8.23	2.92	1.92	0.69	
382		0.04	-6.83	>20.34	14.21	8.35	7.70	7.13	5.86	0.65	
383	IRS 12N	-6.38	-7.87	11.73	9.25	6.63	6.43	2.48	2.63	0.19	cool
385	IRS 14S	-2.37	-10.44	13.02	10.90	9.71	9.80	2.12	1.18	-0.08	
417		-6.82	4.09	14.25	11.73	10.08	9.37	2.52	1.65	0.72	
418	IRS 16CC	-0.87	-0.49	12.13	10.19	8.50	7.92	1.94	1.69	0.57	He I
421		0.28	5.28	14.66	11.99	10.65	>12.73	2.66	1.34	-3.08	
422		3.23	5.90	15.06	12.59	10.89	>12.73	2.47	1.70	-2.84	
423	IRS 10E	5.87	2.97	12.63	10.50	8.84	8.92	2.13	1.65	-0.08	cool
426		-10.01	2.82	14.28	12.02	11.39	9.93	2.26	0.63	1.46	
427		0.70	-3.38	13.41	10.90	9.58	>12.73	2.50	1.32	-4.15	
428	IRS 16NW	-2.86	0.26	11.66	9.84	8.38	8.24	1.82	1.46	0.14	He I
430	IRS 29S	-4.82	0.01	12.33	10.34	9.81	>12.73	2.00	0.53	-3.92	cool
432		-11.72	-2.36	14.26	11.85	10.30	>12.73	2.41	1.55	-3.43	
433		-10.34	-2.53	14.73	12.34	9.38	8.43	2.39	2.96	0.95	
435		-10.72	-4.41	13.27	11.29	9.66	9.23	1.98	1.63	0.43	
437		5.08	-6.75	14.66	12.41	10.85	>12.73	2.25	1.56	-2.88	
438		-9.96	-8.32	13.89	11.81	10.78	>12.73	2.07	1.04	-2.95	
439		-10.25	-8.80	13.09	11.50	10.28	10.11	1.59	1.22	0.17	

Table A.1: continued

ID	Name	$\Delta\alpha(^{\circ})$	$\Delta\delta(^{\circ})$	$H$	$K$	$L$	$M$	$H - K$	$K - L$	$L - M$	Notes
440		-10.66	-8.35	14.01	11.93	10.81	>12.73	2.08	1.12	-2.92	
441	IRS 14NE	-2.20	-9.19	11.84	9.43	7.71	7.87	2.41	1.72	-0.16	cool
461		-4.20	1.85	14.02	11.44	9.47	9.77	2.58	1.97	-0.30	
462		-0.83	-4.95	15.90	13.66	9.48	10.27	2.23	4.18	-0.79	
464		3.89	-7.63	15.32	13.14	10.85	>12.73	2.18	2.29	-2.88	
465		-8.47	-10.46	>12.73	11.63	10.43	10.85	2.11	1.20	-0.42	
488	IRS 1C	4.05	-0.22	12.62	10.42	8.50	8.54	2.20	1.92	-0.04	
490		-9.24	3.69	14.48	12.03	10.58	10.59	2.45	1.45	-0.02	
491		-2.37	-1.44	15.16	12.88	10.38	>12.73	2.28	2.50	-3.35	
492	IRS 21	-0.58	-3.80	14.01	10.41	6.29	5.47	3.61	4.12	0.82	red
498		-8.91	-4.03	14.16	11.43	10.05	9.56	2.73	1.38	0.49	
500		-9.48	-8.30	14.00	12.09	11.33	11.34	1.91	0.77	-0.02	
501		-3.21	-8.25	14.20	12.17	10.64	>12.73	2.03	1.53	-3.09	
502		-3.59	-8.36	13.71	11.26	10.21	10.98	2.45	1.05	-0.77	
503		-5.05	-10.21	12.93	10.65	9.03	9.32	2.28	1.62	-0.29	
523		-6.76	0.58	>20.34	15.07	9.66	8.80	6.27	5.41	0.87	
524		-6.08	0.67	15.09	12.93	9.80	>12.73	2.17	3.13	-3.93	
525	IRS 29NE	-3.90	1.15	14.61	11.57	8.91	8.53	3.04	2.66	0.38	
527		-11.21	-3.72	14.33	12.03	10.74	11.35	2.31	1.29	-0.61	
528		-11.96	-4.24	13.71	11.91	10.51	10.34	1.80	1.40	0.17	
529		1.85	-6.73	13.80	11.80	9.92	>12.73	2.00	1.89	-3.81	
530		2.50	-7.03	13.62	11.65	8.34	7.51	1.96	3.31	0.84	
531		1.71	-9.29	14.96	12.86	10.07	>12.73	2.10	2.79	-3.66	
532		-11.74	-6.16	14.52	12.55	11.03	10.45	1.96	1.52	0.58	
533		-12.10	-6.58	12.37	10.57	9.25	9.05	1.80	1.32	0.20	
534	IRS 12S	-6.57	-9.54	12.07	10.03	8.31	8.91	2.04	1.73	-0.61	cool
535		2.21	-10.53	14.97	12.83	10.64	>12.73	2.14	2.19	-3.09	
549		-11.94	-10.03	14.76	12.77	10.35	10.56	1.98	2.42	-0.21	
567		-5.29	5.10	15.24	12.90	11.31	10.02	2.34	1.58	1.29	
568		1.44	2.20	14.93	12.99	10.06	>12.73	1.94	2.93	-3.67	
569	IRS 35	0.07	-2.23	14.55	11.80	8.63	9.00	2.75	3.17	-0.37	
570		4.06	-1.31	12.95	10.45	8.53	8.91	2.49	1.93	-0.39	
571	IRS 1SE	4.65	-1.59	12.47	10.48	8.78	>12.73	1.99	1.71	-4.95	cool
574		5.25	4.63	15.35	13.20	10.96	>12.73	2.14	2.24	-2.76	
580		6.14	-0.71	>20.34	12.65	9.95	9.14	8.70	2.70	0.81	
581		6.63	-0.89	>20.34	12.47	10.62	9.86	8.87	1.85	0.76	
582		-2.86	-4.37	15.98	13.71	9.85	>12.73	2.27	3.86	-3.88	
584		2.62	-9.35	13.81	11.36	9.40	8.62	2.45	1.96	0.77	
588		-6.64	-8.51	12.58	10.61	9.04	9.04	1.97	1.58	-0.01	
610		-11.49	-7.01	13.39	11.67	10.49	10.18	1.72	1.18	0.31	
612		-5.35	-9.60	13.78	11.74	10.93	11.10	2.04	0.80	-0.16	
617		-2.93	-10.87	15.79	12.80	10.51	11.04	2.99	2.29	-0.53	
626		2.24	3.59	>20.34	13.05	9.05	8.16	8.30	4.00	0.89	
628	IRS 1NEE	4.87	0.45	12.76	10.56	9.23	9.57	2.19	1.34	-0.34	
629		-6.61	0.97	14.28	11.81	8.87	8.32	2.48	2.94	0.55	
630	IRS 34	-7.01	0.77	14.64	11.32	8.23	7.62	3.32	3.09	0.61	He I
631	IRS 33SE	-2.33	-4.13	11.97	9.95	8.17	8.03	2.02	1.78	0.13	
633		-2.23	-5.09	13.87	11.94	10.38	>12.73	1.92	1.57	-3.35	
635		1.07	-5.84	14.16	11.81	10.20	>12.73	2.35	1.61	-3.53	
636		-1.22	-7.39	12.90	10.79	9.63	10.25	2.11	1.16	-0.62	
637	AF/AHH	-9.68	-7.81	12.46	10.43	8.70	8.10	2.03	1.72	0.60	He I

Table A.1: continued

ID	Name	$\Delta\alpha(^{\circ})$	$\Delta\delta(^{\circ})$	$H$	$K$	$L$	$M$	$H - K$	$K - L$	$L - M$	Notes
638		-0.50	-8.80	14.37	11.90	10.53	>12.73	2.46	1.38	-3.20	
647	IRS 7	-2.80	4.63	10.32	8.77	4.48	4.30	1.56	4.28	0.18	M2 I
650	IRS 6E	-8.16	-0.07	12.57	9.58	6.34	5.71	3.00	3.24	0.62	WC9
651	IRS 6W	-10.75	0.61	12.33	10.19	7.83	6.84	2.14	2.36	0.98	
655	IRS 1NE	4.22	0.73	12.59	10.28	8.52	8.72	2.31	1.76	-0.20	cool
658		4.65	4.99	16.53	14.10	10.71	>12.73	2.42	3.39	-3.02	
661		-1.25	-1.62	14.93	12.83	8.86	8.42	2.10	3.96	0.45	
662	IRS 16SWE	-1.08	-2.17	13.45	10.67	7.70	7.12	2.78	2.97	0.57	
663		-1.51	-8.26	14.02	12.03	10.43	>12.73	1.99	1.60	-3.30	
669		4.67	1.73	15.63	13.41	11.31	9.87	2.21	2.10	1.45	
670		-2.88	-1.06	15.56	12.93	10.62	>12.73	2.63	2.31	-3.11	
671		-1.69	-2.92	12.52	10.34	8.54	7.94	2.18	1.80	0.60	
672		-1.33	-3.91	14.08	11.84	9.54	>12.73	2.24	2.30	-4.19	
674		0.28	-3.77	15.00	12.43	10.72	>12.73	2.56	1.71	-3.01	
675		0.17	-5.96	14.22	12.09	8.64	8.37	2.13	3.45	0.27	
676		1.31	-8.36	16.17	13.90	9.10	7.91	2.27	4.80	1.19	
677		-4.83	-7.43	13.61	11.36	9.72	10.05	2.24	1.64	-0.33	
679		2.91	5.08	17.54	13.92	10.39	>12.73	3.61	3.53	-3.34	
680		5.43	3.25	13.48	11.29	9.72	>12.73	2.19	1.57	-4.01	
681	IRS 1SW	3.50	-0.84	12.73	10.43	7.33	6.54	2.30	3.10	0.79	
690		-3.38	-3.06	17.28	14.68	8.95	8.54	2.61	5.73	0.40	
691		0.68	-7.04	17.28	>17.66	9.20	8.40	-1.37	9.46	0.81	
694		-2.87	3.34	16.79	14.05	9.39	>12.73	2.74	4.66	-4.34	
697	IRS 1W	2.43	-0.50	11.73	8.90	4.92	4.02	2.83	3.98	0.90	red
698	IRS 16NE	0.00	0.00	10.68	9.18	7.16	6.87	1.49	2.03	0.29	He I
702	IRS 10W	3.75	4.07	12.95	9.86	6.25	5.02	3.09	3.61	1.23	
704		1.60	4.26	13.60	11.34	9.11	>12.73	2.26	2.23	-4.62	
705		-9.65	2.04	17.36	14.52	9.75	>12.73	2.84	4.77	-3.98	
710		-0.06	-1.12	14.77	12.34	9.11	>12.73	2.42	3.23	-4.62	
711	IRS 33SW	-3.35	-4.20	12.73	10.69	8.61	8.65	2.05	2.08	-0.04	
715		-2.75	5.53	15.77	14.50	10.66	>12.73	1.27	3.84	-3.07	
716		-0.27	-5.51	17.44	>17.66	10.05	8.66	-1.22	8.61	1.39	
718		0.83	-8.37	13.85	11.69	9.15	8.40	2.16	2.53	0.75	
720		-7.01	-6.46	14.38	11.60	7.63	6.54	2.78	3.97	1.10	
721		0.70	-6.36	17.47	15.65	9.24	>12.73	1.82	6.41	-4.49	
723	IRS 7SE	-0.61	3.52	13.38	11.20	10.32	10.22	2.18	0.88	0.10	
724		2.94	1.13	14.29	12.07	9.91	>12.73	2.22	2.16	-3.82	
725		2.98	-1.05	13.77	11.16	7.34	6.91	2.60	3.82	0.43	
728		-9.00	-1.92	16.49	14.16	9.80	8.94	2.32	4.36	0.86	
729		-10.41	-0.68	15.45	13.27	10.12	>12.73	2.18	3.15	-3.61	
730		0.84	5.61	15.56	13.64	11.10	9.77	1.92	2.54	1.33	
731		-4.56	-1.45	14.23	12.32	9.94	9.22	1.91	2.38	0.72	
733		-2.25	-2.60	13.03	11.10	8.56	>12.73	1.94	2.54	-5.17	
737		-1.41	3.69	14.42	11.55	9.87	10.44	2.87	1.68	-0.57	
739		-3.85	6.78	13.08	11.37	9.65	9.50	1.71	1.72	0.15	
741		-3.81	-2.53	13.46	11.24	9.25	9.03	2.23	1.99	0.21	
742		-6.70	-4.24	18.79	15.40	8.00	>12.73	3.39	7.41	-5.73	
743		-3.25	-7.10	13.10	10.80	9.26	9.10	2.29	1.54	0.16	
744		2.21	-8.21	13.61	11.64	9.92	9.45	1.96	1.72	0.48	
745		1.00	6.24	>20.34	11.02	8.91	7.94	10.33	2.10	0.97	
748		4.64	3.92	16.00	13.50	10.07	>12.73	2.50	3.43	-3.66	

Table A.1: continued

ID	Name	$\Delta\alpha(^{\circ})$	$\Delta\delta(^{\circ})$	$H$	$K$	$L$	$M$	$H - K$	$K - L$	$L - M$	Notes
751		-7.07	-2.98	13.68	10.89	7.97	8.00	2.78	2.92	-0.03	
752		4.34	5.72	15.22	13.39	10.90	>12.73	1.83	2.49	-2.83	
753		-1.87	4.89	13.74	11.17	9.48	10.02	2.56	1.69	-0.54	
754		1.64	0.69	16.12	14.20	9.85	>12.73	1.92	4.34	-3.87	
755		-4.57	-3.82	13.52	11.57	9.32	9.66	1.95	2.25	-0.34	
757		1.22	-9.13	14.82	12.40	9.70	>12.73	2.42	2.70	-4.03	
759		-5.80	4.61	14.80	12.41	10.48	>12.73	2.39	1.93	-3.25	
760		-3.83	-1.96	15.76	13.42	10.77	>12.73	2.34	2.64	-2.95	
761		0.49	-1.57	15.26	12.97	9.62	>12.73	2.29	3.36	-4.11	
763		1.13	-7.82	15.08	13.23	9.33	>12.73	1.86	3.90	-4.40	
769		-6.06	-1.82	16.69	13.61	7.36	6.55	3.08	6.24	0.82	
772		0.17	2.45	15.37	12.26	9.77	>12.73	3.11	2.49	-3.96	
774		-4.29	-1.21	14.07	12.19	10.23	9.80	1.88	1.96	0.42	
775		-6.35	-3.78	18.20	15.06	7.57	7.19	3.15	7.49	0.38	
776		-7.51	-7.51	17.26	15.08	9.81	>12.73	2.17	5.27	-3.92	
778		-1.25	5.56	15.84	12.87	11.03	11.16	2.96	1.85	-0.13	
779		-5.23	1.94	18.21	14.82	8.95	>12.73	3.39	5.87	-4.77	
781	IRS 2S	-6.75	-5.61	12.83	10.18	7.92	7.53	2.65	2.26	0.38	cool
782	IRS 20	-3.92	-6.23	12.54	10.57	8.70	8.61	1.97	1.87	0.09	cool
784		2.60	1.98	13.72	11.68	9.79	9.53	2.04	1.89	0.27	
785		-8.54	1.74	19.78	>17.66	9.57	8.25	1.12	9.09	1.32	
786	IRS 16SW	-1.87	-1.97	11.53	9.80	7.92	7.53	1.74	1.88	0.39	He I
791		-6.30	3.04	17.92	16.14	9.28	>12.73	1.77	6.86	-4.44	
792		-8.95	-1.41	17.42	14.36	10.06	8.96	3.06	4.30	1.11	
820	IRS 3	-5.24	2.91	14.98	10.64	4.84	3.35	4.35	5.8	1.49	red
825	IRS 10E*	4.94	3.11	13.62	9.76	5.95	5.20	3.86	3.81	0.75	
828		1.21	1.48	17.09	14.82	10.63	>12.73	2.26	4.20	-3.10	
829		0.88	0.60	14.54	12.10	9.20	8.31	2.44	2.90	0.89	
830		0.76	-0.01	15.29	12.81	9.56	8.58	2.48	3.26	0.98	
831		1.02	-0.79	17.14	14.91	9.78	>12.73	2.22	5.13	-3.94	
833		-9.26	0.70	18.19	15.86	9.61	>12.73	2.33	6.25	-4.12	
836		-8.89	-0.81	16.75	14.26	9.88	>12.73	2.50	4.38	-3.85	
838		-5.62	-2.32	>20.34	13.26	8.16	7.07	8.09	5.09	1.09	
839	IRS 13E	-6.18	-2.49	12.16	9.02	6.18	5.73	3.13	2.84	0.45	He I
840		-5.93	-2.63	11.90	>17.66	7.19	6.63	-6.76	11.47	0.56	
841		-7.31	-2.48	14.21	12.26	8.86	8.73	1.95	3.41	0.12	
845		-5.69	-4.65	16.57	14.01	8.82	>12.73	2.56	5.19	-4.91	
846	IRS 2L	-6.47	-4.82	14.26	10.60	6.49	5.55	3.67	4.11	0.94	
848		-4.98	-5.19	16.53	14.32	9.33	8.60	2.21	4.99	0.73	
849		-5.54	-5.32	16.83	14.61	8.77	7.80	2.21	5.84	0.97	
851		-4.20	-5.23	>20.34	16.04	9.66	9.24	5.31	6.38	0.42	
852		-4.76	-5.87	15.58	13.47	9.15	>12.73	2.11	4.33	-4.58	
856		-2.93	-5.84	15.69	13.63	10.34	>12.73	2.06	3.29	-3.39	
857		-3.57	-6.47	14.37	12.33	9.90	>12.73	2.04	2.43	-3.83	
864		1.69	3.96	15.03	12.39	>14.47	8.69	2.64	-3.08	6.77	
865		1.57	-0.87	14.83	13.00	>14.47	8.92	1.83	-2.47	6.54	
866		0.28	-1.07	14.91	12.48	>14.47	9.09	2.42	-2.98	6.38	
867		-11.30	-0.91	16.28	14.12	>14.47	9.06	2.17	-1.35	6.41	
868		-0.90	-1.61	13.81	11.48	>14.47	8.62	2.33	-3.99	6.85	
869		-5.81	-3.74	14.60	12.11	>14.47	7.73	2.48	-3.36	7.74	
870		-4.51	-5.76	14.53	12.27	>14.47	8.88	2.26	-3.19	6.59	

Table A.1: continued

ID	Name	$\Delta\alpha(^{\circ})$	$\Delta\delta(^{\circ})$	$H$	$K$	$L$	$M$	$H - K$	$K - L$	$L - M$	Notes
871		1.49	-7.91	17.80	15.11	>14.47	8.84	2.68	-0.36	6.62	
874		-8.65	-0.90	17.28	14.73	>14.47	9.68	2.55	-0.74	5.79	
876		-5.66	1.93	16.15	13.94	>14.47	8.96	2.22	-1.53	6.51	
877		2.51	-1.02	15.05	12.36	>14.47	7.54	2.70	-3.11	7.93	
878		-7.11	-3.55	16.93	15.32	>14.47	8.36	1.62	-0.15	7.11	
879		1.10	-6.90	15.70	13.78	>14.47	8.77	1.92	-1.69	6.70	
880		-7.27	-8.02	15.33	13.12	>14.47	9.55	2.21	-2.35	5.91	
881		-6.63	2.72	17.23	14.93	>14.47	8.11	2.30	-0.54	7.36	
882		1.38	0.32	16.97	15.19	>14.47	8.84	1.78	-0.28	6.63	
884		-8.58	-2.16	15.11	12.66	>14.47	9.56	2.45	-2.81	5.91	
886		-2.59	-4.35	14.40	12.21	>14.47	9.77	2.19	-3.26	5.69	
887		-7.44	-6.89	16.99	14.79	>14.47	8.63	2.20	-0.68	6.84	
888		-6.79	-9.56	13.30	11.08	>14.47	10.46	2.22	-4.39	5.01	
890		-2.62	-3.51	15.78	14.40	>14.47	8.34	1.38	-1.07	7.13	
892		2.21	3.05	17.36	15.11	>14.47	8.44	2.25	-0.36	7.02	
893		-3.88	-1.62	16.56	14.85	>14.47	10.49	1.71	-0.62	4.98	

Table A.2: Photometry of sources outside the NAOS/CONICA field of view. See also table A.1.

ID	$\Delta\alpha(^{\circ})$	$\Delta\delta(^{\circ})$	$L$	$M$	$L - M$	ID	$\Delta\alpha(^{\circ})$	$\Delta\delta(^{\circ})$	$L$	$M$	$L - M$
1	-0.80	-35.11	10.07	9.62	0.45	310	-33.72	21.24	10.08	9.61	0.46
3	-5.93	-32.19	10.79	10.34	0.45	311	12.40	21.90	9.86	9.60	0.26
4	-22.96	-32.77	9.78	9.20	0.58	312	-10.16	24.14	11.32	10.78	0.54
5	23.34	-32.39	10.10	9.75	0.35	314	-23.77	25.57	10.67	10.22	0.46
7	-8.82	-31.00	9.45	9.01	0.44	315	-8.63	26.07	10.97	10.47	0.50
8	12.45	-28.98	10.20	9.75	0.45	317	-7.89	27.65	10.84	10.48	0.36
9	16.52	-13.78	10.87	10.66	0.22	318	-32.09	32.00	10.39	9.85	0.54
10	-25.39	0.74	10.42	10.08	0.34	319	-15.80	35.63	10.76	9.99	0.77
11	23.03	9.63	10.43	9.94	0.49	320	-29.46	35.72	8.23	7.39	0.84
12	2.55	11.02	9.95	9.07	0.89	323	-26.85	-33.73	9.59	9.30	0.29
14	27.06	17.85	11.08	10.78	0.30	324	26.74	-31.71	11.31	10.36	0.95
15	-24.35	25.29	11.13	10.70	0.43	325	16.79	-27.16	10.93	10.07	0.86
16	-21.57	27.26	7.99	7.15	0.84	326	-5.95	-18.59	9.67	8.93	0.74
18	-3.93	-35.87	8.84	8.24	0.61	330	8.66	-2.77	9.24	8.70	0.53
19	26.62	-33.64	11.22	10.89	0.32	333	14.30	5.79	9.01	8.38	0.63
20	-0.83	-33.64	9.61	9.22	0.40	334	-27.12	6.83	10.22	10.10	0.13
23	-34.08	-31.70	9.67	9.38	0.28	335	17.07	10.67	10.47	9.89	0.58
24	-5.05	-30.79	10.02	9.23	0.79	336	-15.31	12.11	8.24	7.52	0.72
25	-22.60	-29.16	9.03	8.45	0.58	337	-22.06	15.15	10.94	10.09	0.84
28	17.22	-25.44	10.19	9.68	0.51	340	-1.47	22.73	8.80	8.06	0.74
29	-29.86	-22.60	8.15	7.62	0.54	341	-26.79	26.32	10.74	10.35	0.39
30	13.95	-21.14	10.50	9.93	0.57	343	-36.50	-34.74	10.17	9.91	0.26
31	-25.98	-20.28	8.39	7.73	0.66	344	1.61	-32.95	8.70	8.12	0.58
32	-36.24	-20.28	9.64	9.46	0.18	345	-20.59	-32.11	8.98	8.37	0.61
36	-26.61	-18.29	9.72	9.13	0.59	347	-21.08	-29.48	10.38	9.75	0.63
38	4.59	-17.19	9.50	8.78	0.72	351	11.43	-23.76	10.80	10.24	0.56

Table A.2: continued

ID	$\Delta\alpha(^{\circ})$	$\Delta\delta(^{\circ})$	$L$	$M$	$L - M$	ID	$\Delta\alpha(^{\circ})$	$\Delta\delta(^{\circ})$	$L$	$M$	$L - M$
39	-4.52	-16.13	9.02	8.28	0.74	352	19.70	-22.54	8.15	7.53	0.62
40	-19.68	-16.45	10.73	9.94	0.79	353	-27.50	-20.40	10.69	10.34	0.35
41	-19.80	-14.45	8.84	8.32	0.52	354	-16.47	-19.87	11.38	11.00	0.38
42	-38.13	-13.74	9.88	9.48	0.39	356	2.71	-18.97	10.80	10.18	0.62
43	2.85	-13.66	9.36	8.89	0.47	357	18.71	-18.06	11.40	10.52	0.88
44	-32.32	-11.85	11.01	10.74	0.27	359	-1.05	-14.51	10.15	9.73	0.41
45	-34.76	-10.12	9.76	9.45	0.31	364	6.26	-7.05	9.28	7.66	1.63
47	10.00	-9.68	8.85	6.98	1.87	367	-1.49	-10.65	10.45	8.96	1.49
48	-32.92	-6.90	9.32	8.72	0.61	369	-7.24	-10.17	9.69	9.12	0.57
49	17.06	-5.44	11.11	10.66	0.45	370	16.74	-10.04	10.92	10.35	0.57
51	17.50	-4.20	9.99	9.53	0.46	372	12.38	-8.21	10.04	9.62	0.41
52	-13.48	-2.55	10.45	9.60	0.85	373	-10.43	-8.48	11.14	10.14	1.00
53	17.59	-2.30	9.63	9.16	0.47	375	-12.17	-5.66	11.36	11.43	-0.07
54	-32.56	-0.91	9.94	9.56	0.38	381	-15.58	5.63	10.16	9.64	0.52
55	12.35	1.47	11.05	10.76	0.28	382	-12.82	5.72	11.19	10.62	0.57
57	25.02	6.37	10.15	9.64	0.51	385	8.23	7.58	9.69	8.86	0.83
58	14.09	7.34	11.10	10.89	0.21	387	-1.26	12.24	11.28	10.38	0.89
60	23.83	8.36	10.15	9.59	0.56	388	8.41	11.04	10.37	9.43	0.93
61	-23.95	10.41	10.82	10.34	0.48	389	-12.52	12.30	10.34	10.01	0.33
62	16.49	11.10	10.49	10.07	0.41	390	-20.92	13.02	10.95	10.48	0.46
63	33.05	11.47	10.00	9.55	0.45	391	-10.45	14.03	10.83	10.60	0.23
64	18.43	12.78	10.57	10.21	0.36	392	-10.94	14.67	9.96	9.50	0.46
65	-22.07	14.20	10.92	10.32	0.59	393	-0.81	14.79	10.40	9.85	0.55
66	11.21	16.88	10.85	10.85	0.00	394	-1.45	15.34	11.21	10.60	0.61
67	29.50	13.30	10.01	9.54	0.46	396	-5.53	18.64	11.43	10.90	0.53
68	-11.63	15.78	9.93	9.32	0.61	397	-30.91	18.77	9.09	8.48	0.61
69	24.57	13.93	9.94	9.51	0.44	398	-10.79	18.93	11.38	11.66	-0.28
70	2.98	15.26	10.17	10.02	0.16	399	-11.57	20.73	9.03	8.37	0.66
71	-18.56	16.13	10.83	10.41	0.42	400	-21.54	18.96	9.92	9.43	0.49
72	23.20	16.78	9.40	8.89	0.51	401	1.59	19.47	10.23	9.83	0.39
73	-31.65	17.76	10.38	9.91	0.47	402	-12.45	29.23	10.09	9.66	0.43
74	-3.92	19.83	10.40	10.02	0.38	404	-30.97	30.65	9.48	8.89	0.59
76	-22.83	21.47	10.30	9.86	0.44	405	13.32	-31.83	11.13	10.56	0.58
77	11.30	22.61	10.02	9.73	0.29	407	0.23	-25.44	10.26	9.75	0.50
79	-3.10	26.18	10.06	9.61	0.45	408	-16.50	-22.10	10.41	9.93	0.48
82	25.35	28.00	10.91	10.31	0.60	409	-8.60	-21.95	11.35	11.28	0.07
84	-8.64	31.88	10.77	10.17	0.60	410	-1.33	-20.79	10.34	9.73	0.61
86	5.82	32.43	10.74	10.58	0.16	411	0.21	-17.43	9.52	8.81	0.71
87	-24.44	33.48	10.37	10.00	0.38	412	-11.53	-14.79	10.96	9.78	1.19
88	30.61	34.30	10.88	10.65	0.23	413	-11.34	-12.48	7.63	7.03	0.60
89	5.35	34.34	10.20	9.88	0.33	414	-11.05	-12.46	9.57	8.72	0.85
93	16.39	-27.77	9.12	8.53	0.58	416	-8.95	-10.33	11.24	11.06	0.18
94	-13.78	-24.23	11.00	10.57	0.43	417	-13.10	-8.35	9.75	9.16	0.58
95	-14.01	-23.45	9.55	9.07	0.47	420	9.25	1.99	9.96	9.52	0.44
96	-16.80	-19.37	8.11	7.17	0.94	421	-35.04	-8.28	10.14	9.81	0.32



Table A.2: continued

ID	$\Delta\alpha(^{\circ})$	$\Delta\delta(^{\circ})$	$L$	$M$	$L - M$	ID	$\Delta\alpha(^{\circ})$	$\Delta\delta(^{\circ})$	$L$	$M$	$L - M$
97	22.45	-19.64	11.12	10.50	0.62	430	-30.73	-1.50	10.70	10.81	-0.11
98	8.49	1.54	10.00	9.37	0.63	435	-12.51	3.57	10.67	9.86	0.81
99	-15.42	-7.02	9.88	9.20	0.67	437	27.64	4.78	11.20	10.92	0.28
100	-27.63	1.68	10.26	9.83	0.43	443	14.67	9.22	10.47	10.18	0.29
101	-20.74	2.98	10.46	10.52	-0.07	444	-11.98	9.98	10.89	10.72	0.16
105	-27.40	15.31	10.43	9.97	0.46	445	-8.11	13.54	11.20	10.34	0.86
106	-32.23	22.22	9.99	9.59	0.40	446	10.44	13.89	10.27	10.26	0.01
107	26.52	22.48	10.11	9.74	0.38	448	12.40	16.95	10.22	10.36	-0.14
108	-1.42	28.44	8.42	7.69	0.73	449	24.76	18.65	9.36	8.76	0.60
110	28.18	32.38	10.55	10.40	0.15	451	-6.38	24.89	9.54	9.05	0.49
113	-0.67	-35.93	10.74	10.35	0.39	455	-6.55	28.37	8.67	8.08	0.59
114	0.69	-35.40	11.17	10.95	0.22	456	-17.33	31.48	10.09	9.54	0.55
116	13.84	-33.58	10.25	9.80	0.45	457	17.96	-20.00	9.26	8.56	0.70
117	-6.51	-33.52	10.47	10.03	0.44	458	-3.29	-17.10	11.26	10.48	0.78
121	10.30	-30.28	11.02	10.50	0.52	459	12.56	-9.47	10.80	10.44	0.35
122	11.28	-30.05	10.21	9.43	0.78	460	1.31	0.06	9.74	8.53	1.20
123	32.53	-29.84	6.84	5.98	0.86	461	12.59	-2.16	10.61	10.14	0.47
125	13.02	-29.60	10.09	9.52	0.57	464	-28.28	6.09	10.78	10.45	0.33
126	13.68	-28.88	11.19	10.90	0.29	467	-6.83	23.08	9.04	8.20	0.84
127	0.72	-25.97	10.53	9.98	0.55	468	-4.95	28.47	10.20	9.69	0.51
128	1.67	-25.85	10.78	10.21	0.56	470	0.78	-33.12	9.87	9.37	0.50
129	-10.05	-28.46	9.83	9.36	0.47	471	1.95	-33.48	10.87	10.26	0.60
131	22.33	-25.09	10.93	10.45	0.48	475	-4.62	-18.56	9.84	9.20	0.64
132	26.85	-25.61	10.74	10.31	0.43	476	-5.42	-16.26	10.91	10.69	0.22
133	23.56	-23.51	10.94	10.27	0.67	479	5.45	-11.76	9.59	9.12	0.48
134	24.38	-22.98	11.05	10.64	0.41	480	1.59	-10.00	11.16	10.41	0.74
135	20.49	-24.98	10.68	10.19	0.49	484	7.90	-5.81	9.98	8.60	1.37
136	-17.85	-23.75	10.50	9.60	0.90	487	-2.78	-9.21	10.16	9.21	0.95
137	11.97	-24.21	9.86	9.30	0.57	488	-6.29	-8.61	9.30	8.77	0.53
138	17.34	-24.00	9.91	9.35	0.57	491	26.09	-7.47	10.34	10.02	0.32
140	-0.08	-23.02	11.28	10.37	0.91	495	-21.97	1.98	10.80	10.31	0.49
142	-11.67	-22.43	9.34	8.55	0.79	496	17.67	3.27	9.20	8.49	0.71
143	15.64	-21.36	10.28	9.74	0.55	497	18.59	2.93	11.01	10.59	0.42
144	5.59	-19.32	10.08	9.60	0.48	498	17.98	3.94	10.14	9.78	0.36
145	6.19	-20.98	10.73	10.14	0.58	501	10.05	7.63	11.15	10.79	0.36
146	23.97	-20.49	10.08	9.66	0.42	508	-37.39	15.09	9.53	9.09	0.44
148	-2.89	-18.89	10.43	9.94	0.48	509	-12.38	16.47	10.40	9.60	0.79
149	13.73	-18.75	9.75	9.31	0.45	510	14.43	23.30	10.78	10.62	0.15
150	-37.33	-18.48	10.28	9.74	0.54	511	-30.13	28.55	9.78	9.27	0.50
151	-12.12	-17.95	10.25	9.39	0.85	513	-9.61	31.48	11.09	10.57	0.52
152	-32.96	-17.89	9.02	8.42	0.60	514	14.80	-27.34	10.39	9.82	0.56
154	-25.93	-16.56	10.51	10.19	0.32	515	10.09	-22.41	8.86	8.31	0.55
155	-25.73	-15.90	8.98	8.43	0.55	517	-4.70	-12.05	11.02	10.78	0.24
157	-14.00	-16.36	10.48	9.83	0.66	518	4.22	-9.00	9.96	9.11	0.85
158	27.70	-16.07	10.33	9.50	0.83	519	-4.45	-8.98	10.33	8.91	1.42

Table A.2: continued

ID	$\Delta\alpha(^{\circ})$	$\Delta\delta(^{\circ})$	$L$	$M$	$L - M$	ID	$\Delta\alpha(^{\circ})$	$\Delta\delta(^{\circ})$	$L$	$M$	$L - M$
161	6.30	-14.31	10.59	9.98	0.61	522	23.09	-2.82	9.32	8.69	0.63
162	8.67	-14.16	11.36	10.91	0.45	523	14.75	-2.71	11.28	10.58	0.71
163	16.06	-12.38	10.60	10.09	0.51	528	22.41	1.65	11.23	10.86	0.37
164	11.97	-12.39	9.83	9.36	0.48	538	-8.75	10.87	10.04	9.55	0.48
166	8.70	-11.63	10.52	9.83	0.69	540	8.03	14.63	10.22	9.67	0.55
168	10.12	-12.00	9.16	8.55	0.61	541	11.72	19.49	8.27	7.63	0.64
170	-1.67	-10.28	7.58	6.47	1.11	542	-18.19	-27.05	10.27	9.63	0.65
171	-12.40	-10.85	8.44	7.77	0.67	543	5.36	-19.99	10.60	10.00	0.60
172	-3.48	-10.67	9.32	8.79	0.53	544	13.26	-9.34	10.82	10.41	0.41
174	-5.13	-7.42	9.09	8.37	0.72	545	13.15	-9.00	10.47	10.05	0.42
176	-8.56	-8.35	9.41	8.98	0.43	553	12.39	11.79	8.32	7.71	0.60
178	-17.49	-6.35	9.27	8.36	0.91	554	-11.45	12.21	9.34	8.64	0.70
180	-32.72	-6.17	10.72	10.34	0.38	555	-36.02	14.58	8.99	8.37	0.63
184	12.79	-3.71	11.27	11.58	-0.31	556	13.37	22.71	8.36	7.67	0.69
185	12.43	-1.23	10.56	10.01	0.55	557	-1.17	23.36	9.40	8.77	0.63
186	-34.42	-2.43	9.94	9.71	0.23	558	-6.15	25.23	9.57	9.15	0.41
188	22.84	-0.83	10.40	10.10	0.31	561	15.72	-29.70	10.93	10.58	0.36
189	21.56	-0.56	10.90	11.56	-0.67	562	1.05	-27.69	9.81	9.22	0.59
190	15.10	0.07	11.14	11.61	-0.47	564	-16.00	-18.60	11.31	10.35	0.96
191	19.75	1.02	9.46	8.88	0.59	565	10.14	-15.66	11.22	9.74	1.48
192	-16.14	2.19	10.79	10.98	-0.19	566	-2.51	-16.75	9.93	8.96	0.97
193	-16.24	2.97	10.45	9.62	0.84	567	-13.59	-12.76	11.18	9.76	1.42
194	12.63	5.20	9.97	9.26	0.72	574	-11.54	-7.29	11.15	10.21	0.94
195	10.75	6.01	10.13	9.42	0.71	578	-17.80	-2.99	10.88	10.16	0.72
201	-8.95	11.88	11.26	10.17	1.10	579	-17.89	-0.22	10.48	9.76	0.72
203	-32.63	10.64	10.42	10.03	0.39	585	-12.31	1.55	9.77	8.84	0.92
204	22.35	11.83	9.55	9.07	0.48	588	7.60	6.82	7.80	7.12	0.67
205	-16.69	13.57	10.43	9.85	0.58	589	32.65	9.18	10.04	9.61	0.43
208	0.77	12.30	8.29	7.83	0.46	591	-25.06	9.50	11.48	10.49	0.99
209	-18.97	13.38	11.29	11.37	-0.08	594	5.58	18.01	10.94	10.18	0.76
210	3.57	13.75	11.28	11.71	-0.42	595	-36.13	19.07	8.86	7.77	1.09
211	-0.56	16.00	9.46	8.89	0.57	598	25.92	-26.48	9.80	9.44	0.36
212	-15.60	14.37	10.75	10.15	0.61	600	-10.34	-19.07	10.20	9.27	0.93
213	-2.71	16.03	10.12	9.71	0.41	601	3.87	-12.18	10.94	9.71	1.23
214	-31.31	16.58	10.25	9.83	0.42	604	2.92	-10.54	10.32	9.79	0.53
215	-2.16	17.91	10.94	10.79	0.15	608	11.59	-9.40	10.23	9.73	0.50
219	2.73	18.99	9.95	9.47	0.47	609	0.36	0.63	9.43	7.81	1.62
220	-3.54	20.15	10.55	10.08	0.47	610	20.16	-2.39	9.54	8.82	0.72
221	-22.26	18.81	9.94	9.44	0.50	616	14.36	-4.52	9.44	9.12	0.31
222	17.31	19.48	10.12	9.68	0.44	617	23.61	-2.23	10.49	9.80	0.69
224	-14.84	19.91	9.90	9.44	0.46	618	-32.52	7.10	10.94	10.36	0.58
225	-26.06	21.06	10.69	10.20	0.49	620	-32.02	12.88	10.10	9.62	0.48
226	-8.78	22.41	8.98	8.20	0.77	621	-34.03	12.79	9.87	9.33	0.55
227	-9.11	22.04	9.97	9.60	0.37	622	24.50	22.57	10.24	9.58	0.66
228	-23.94	22.67	10.53	9.97	0.56	624	-19.92	-27.53	10.71	10.10	0.61

Table A.2: continued

ID	$\Delta\alpha(^{\circ})$	$\Delta\delta(^{\circ})$	$L$	$M$	$L - M$	ID	$\Delta\alpha(^{\circ})$	$\Delta\delta(^{\circ})$	$L$	$M$	$L - M$
231	1.16	22.92	10.66	9.93	0.73	625	-7.73	-24.46	10.97	10.64	0.33
232	-4.97	22.84	10.96	10.42	0.54	626	8.05	-8.40	10.20	8.45	1.75
234	26.74	24.37	9.77	9.34	0.43	627	2.19	-4.11	10.42	8.27	2.16
235	-21.96	25.38	9.80	9.32	0.48	629	-15.81	-2.77	11.46	10.74	0.72
237	-0.55	25.85	10.81	10.27	0.54	642	1.15	-31.56	10.34	9.79	0.55
238	-37.72	26.39	9.91	10.10	-0.19	645	-8.47	-12.48	10.81	10.38	0.43
239	-1.71	26.22	10.56	10.13	0.43	647	4.34	-11.59	11.05	9.68	1.37
240	1.15	27.27	10.83	10.39	0.44	650	14.65	-4.48	9.03	8.24	0.80
241	1.60	30.55	11.00	10.64	0.36	655	9.08	15.31	11.04	10.82	0.21
242	-5.15	30.48	10.94	10.57	0.37	659	20.85	19.03	9.16	8.74	0.42
243	-28.99	31.16	9.44	8.89	0.55	680	-5.53	26.80	7.17	6.61	0.56
244	-18.12	31.20	10.90	10.33	0.56	686	1.26	21.25	11.09	10.45	0.64
245	-7.70	32.75	10.76	10.24	0.52	687	17.10	-19.13	9.74	9.12	0.62
246	-29.69	33.35	10.27	9.98	0.29	688	19.29	-14.30	9.16	8.71	0.45
249	-17.47	35.45	10.22	9.73	0.49	689	-3.43	-8.70	10.46	10.08	0.38
251	11.12	-34.59	9.84	9.50	0.34	694	18.96	10.68	10.35	9.59	0.76
252	31.18	-33.61	8.47	7.89	0.57	695	-18.04	-4.85	10.71	10.29	0.42
255	1.33	-30.84	11.09	10.53	0.56	701	-3.10	-28.46	10.61	8.98	1.63
258	31.67	-29.20	10.05	9.55	0.50	702	-3.32	-27.92	10.71	9.06	1.66
259	-13.50	-24.95	9.32	8.84	0.48	710	-1.82	-28.31	7.74	5.69	2.05
260	-14.20	-24.79	10.14	9.61	0.52	711	15.20	-1.79	10.26	9.79	0.46
263	-15.24	-24.36	10.37	9.96	0.40	716	-5.73	-10.21	9.40	8.90	0.50
264	11.13	-23.16	10.31	9.83	0.48	719	0.45	7.62	10.09	8.52	1.57
265	-19.19	-22.44	8.38	7.74	0.64	729	-10.19	-0.58	9.05	6.73	2.32
268	-13.64	-21.29	11.24	11.43	-0.19	736	-2.90	3.35	9.40	7.69	1.71
269	18.66	-19.25	11.45	10.76	0.69	737	16.79	-29.41	9.78	9.18	0.59
270	16.15	-17.32	10.22	9.68	0.54	749	-18.32	-5.60	10.75	10.02	0.73
273	-4.94	-12.66	10.73	10.29	0.44	751	-10.55	29.56	7.63	6.89	0.75
275	18.55	-11.56	10.79	10.55	0.24	752	-1.55	-28.53	7.90	5.46	2.44
277	13.31	-7.95	9.79	9.39	0.41	758	-2.61	2.97	9.34	7.86	1.48
279	-2.31	-8.16	9.95	9.62	0.33	766	6.46	19.30	8.44	7.86	0.59
280	-2.90	-7.51	9.92	9.08	0.83	767	19.80	-14.17	8.99	8.50	0.50
281	9.02	-6.02	10.81	10.68	0.12	769	-7.86	-1.35	11.14	9.80	1.34
282	-34.65	-4.42	9.92	9.63	0.29	770	-8.54	-0.45	10.41	8.46	1.95
283	10.26	-4.55	7.48	6.71	0.77	775	-9.67	-1.10	10.28	7.77	2.52
284	12.73	-4.85	10.32	9.92	0.40	795	12.00	19.71	7.16	6.73	0.43
285	20.25	-0.67	10.78	10.31	0.47	796	-0.88	30.80	8.75	8.16	0.59
286	7.65	-0.21	8.67	8.02	0.65	800	-5.74	-2.11	9.46	7.53	1.93
290	18.95	1.94	10.36	9.88	0.48	802	-6.36	29.76	10.42	9.88	0.54
292	11.56	7.86	10.71	9.86	0.85	810	-26.99	-22.07	8.65	8.13	0.53
293	-13.49	9.11	9.72	9.29	0.42	812	14.50	-14.14	9.71	9.24	0.48
294	5.97	9.46	11.39	11.27	0.12	813	5.69	-8.80	6.60	5.02	1.58
295	8.46	9.89	9.45	8.77	0.68	815	24.91	-9.28	9.05	8.56	0.49
297	-23.49	11.84	11.01	10.30	0.71	816	23.62	-7.14	9.24	8.81	0.43
298	25.88	12.98	10.64	10.23	0.41	821	-5.27	-2.90	7.03	3.04	3.99

Table A.2: continued

ID	$\Delta\alpha(^{\circ})$	$\Delta\delta(^{\circ})$	$L$	$M$	$L - M$	ID	$\Delta\alpha(^{\circ})$	$\Delta\delta(^{\circ})$	$L$	$M$	$L - M$
299	25.64	13.36	10.97	10.57	0.40	844	-5.46	3.51	8.72	7.36	1.36
300	-21.41	13.85	10.93	10.40	0.53	860	-28.23	6.57	9.53	9.05	0.49
303	-6.32	16.66	8.64	7.99	0.65	861	-17.76	22.73	9.46	8.93	0.53
305	-8.44	17.37	9.70	8.86	0.84	862	-12.47	27.01	9.15	8.57	0.58
306	-8.84	18.47	9.73	9.25	0.48	863	5.26	28.82	8.19	6.42	1.76
307	-7.70	20.09	10.69	10.88	-0.18	864	-11.12	31.87	8.94	8.57	0.37
308	16.19	18.03	10.09	9.74	0.36	865	-38.65	34.04	11.42	9.23	2.19
309	-10.48	20.13	10.97	10.18	0.79						

Table A.3: Extinction corrected flux densities of compact  $N$ -band sources.

ID	Name	$\Delta\alpha(^{\circ})$	$\Delta\delta(^{\circ})$	Flux density (Jy)								
				1.6	2.1	3.8	4.7	8.6	11.3	12.8	18.7	19.5
1	IRS 1W	5.1	-5.05	1.37	2.29	12.65	16.29	20.42	16.35	22.93	16.48	18.94
2	...	5.8	-5.3	...	...	...	...	2.21	1.2	3.1	...	...
3	...	3.5	-4.0	0.1	0.12	0.25	0.31	0.13	0.42	0.6	0.98	0.46
4	...	3.5	-4.05	...	...	...	...	0.24	...	...	...	...
5	...	5.3	-6.55	...	0.07	0.12	0.15	0.06	0.03	0.13	...	...
6	IRS 2L	-3.6	-9.45	0.13	0.48	2.98	3.98	5.26	4.72	7.49	2.05	2.58
7	IRS 2S	-4.0	-11.05	0.5	0.49	0.8	0.64	0.68	0.61	1.3	0.75	1.01
8	IRS 3	-2.45	-1.8	0.07	0.46	13.61	30.2	13.42	6.57	12.85	5.85	6.88
9	...	-2.25	-3.3	...	...	...	...	0.21	0.03	0.31	...	...
10	...	-1.0	-1.65	...	...	...	...	0.14	0.06	0.14	0.23	...
11	IRS 4	10.3	-11.5	...	...	...	...	0.11	0.19	0.45	0.48	0.61
12	...	9.8	-14.4	...	...	...	...	0.14	0.27	0.63	0.77	0.76
13	IRS 5	8.5	4.15	...	...	4.27	4.88	5.11	4.21	5.85	3.21	2.85
14	IRS 5NE	12.7	5.0	...	...	0.53	0.8	0.51	0.6	0.56	0.95	0.74
15	IRS 5E	10.8	3.7	...	...	0.15	0.21	0.59	1.06	1.54	1.58	1.72
16	...	10.0	4.25	...	...	...	...	0.04	...	...	...	...
17	...	11.15	2.9	...	...	...	...	0.05	...	...	...	...
18	IRS 5S	9.0	2.35	...	...	0.36	0.43	0.63	0.51	0.38	0.63	1.06
19	IRS 5SE1	10.55	1.3	...	...	0.19	0.18	0.5	0.97	1.1	2.84	3.58
20	IRS 5SE2	10.95	1.1	...	...	...	...	0.04	0.09	0.13	...	...
21	...	12.8	-0.15	...	...	1.88	1.03	0.08	0.08	0.12	0.21	...
22	IRS 6W	-7.5	-4.25	0.79	0.7	0.87	1.21	3.67	2.95	8.0	2.95	3.37
23	IRS 6E	-5.3	-4.8	0.63	1.22	3.42	3.44	0.21	0.04	0.17	0.16	...
24	...	-7.35	-7.25	0.09	0.1	0.21	0.28	0.19	0.08	0.58	0.43	0.43
25	IRS 7	0.0	0.0	5.04	2.58	18.97	12.59	1.47	1.14	1.75	0.36	0.41
26	...	-0.25	2.3	...	...	...	...	0.05	0.03	0.11	0.07	0.11
27	IRS 15	1.1	5.65	...	...	1.71	1.28	0.14	0.12	0.13	0.08	0.13
28	...	3.65	1.55	...	0.33	0.32	0.44	0.15	0.24	0.32	0.4	0.34
29	IRS 9	5.4	-11.95	1.31	1.43	2.06	1.15	0.21	0.13	0.21	0.11	0.26
30	IRS 9N	5.4	-11.45	0.24	0.18	0.54	0.65	0.59	0.76	1.21	0.87	1.37
31	...	3.5	-10.9	0.01	...	0.24	...	3.68	2.6	3.58	1.4	2.94
32	...	4.05	-12.9	0.02	0.02	0.27	0.45	2.93	2.77	3.9	2.13	5.51
33	...	5.0	-16.0	0.07	0.06	0.07	...	0.82	0.94	...	...	...
34	...	3.4	-16.9	...	...	...	...	0.03	...	...	...	...
35	IRS 10W	6.35	-0.5	0.45	0.95	3.72	6.49	11.06	10.31	11.85	9.32	9.75
36	IRS 10E*	7.5	-1.45	0.24	1.04	4.9	5.5	0.64	0.25	0.75	0.32	0.37
37	...	6.55	2.05	...	...	...	...	0.1	...	...	...	...
38	...	7.8	-0.4	0.05	0.04	0.05	...	0.21	0.38	...	...	...
39	...	6.2	-8.45	...	...	...	...	0.46	0.56	1.67	0.99	0.71

40	...	6.1	-9.55	...	...	...	...	0.48	0.12	0.76	...	...
41	...	3.2	-2.2	0.05	0.1	0.15	...	0.01	0.13	...	...	...
42	IRS 12N	-3.5	-12.45	1.37	1.66	2.62	1.77	0.15	0.12	0.1	...	...
43	...	-3.8	-14.9	...	...	...	...	0.02	0.03	...	...	...
44	IRS 13E	-3.35	-7.1	0.92	2.05	3.96	3.37	4.28	4.49	6.16	2.11	2.89
45	IRS 13W	-4.2	-7.6	0.23	0.37	0.76	0.42	0.25	2.02	2.59	1.1	2.0
46	...	-2.65	-8.0	...	...	...	...	0.36	0.24	0.74	...	...
47	IRS 13N	-3.15	-6.5	0.01	0.03	1.34	1.58	0.38	0.65	1.11	0.55	0.58
48	IRS 13NE	-2.85	-7.0	...	0.04	0.64	0.98	0.43	0.67	1.13	0.47	0.67
49	IRS 14NE	0.7	-13.75	1.24	1.41	0.97	0.47	0.05	0.05	0.08	0.17	...
50	IRS 14SW	-0.4	-14.5	1.25	1.25	0.6	0.25	0.02	0.02	0.02	...	...
51	...	1.1	-12.65	0.17	0.13	0.08	...	0.05	0.06	0.2	0.55	0.52
52	AF/AHH	-6.65	-12.45	0.7	0.56	0.39	0.38	0.02	0.01	...	...	...
53	IRS 20	-2.2	-11.95	0.65	0.49	0.39	0.24	0.02	0.05	0.15	...	...
54	IRS 21	2.15	-8.35	0.17	0.57	3.58	4.29	4.56	4.57	5.44	3.76	4.1
55	IRS 29	-1.75	-4.2	0.15	0.6	2.04	1.98	0.15	0.02	0.04	...	...
56	IRS 33SW	-0.4	-8.7	0.55	0.44	0.42	0.23	0.08	0.05	0.09	...	...
57	IRS 34(SW)	-4.05	-4.0	...	0.01	0.16	0.2	0.12	0.04	0.16	...	...
58	IRS 34NE	-3.65	-3.55	0.13	0.16	0.33	0.31	0.14	0.08	0.18	0.13	0.19
59	IRS 33NW	-0.9	-7.25	0.28	0.27	0.23	0.16	0.69	0.29	0.61	0.68	0.73
60	...	-1.65	-6.15	0.14	0.1	0.12	0.14	1.27	1.32	1.9	1.37	0.66
61	IRS 16NW	-0.1	-4.45	1.47	0.96	0.52	0.36	0.01	...	...	...	...
62	IRS 16NE	2.75	-4.7	3.61	1.77	1.61	1.18	0.08	...	...	...	...
63	...	1.25	-4.65	...	...	...	...	0.01	0.01	0.05	...	...
64	SgrA* Clump	-0.25	-5.65	0.04	0.06	0.07	...	0.02	0.17	0.23	0.32	0.29

wavelength $\lambda$ (in $\mu\text{m}$ )	$(A_\lambda/A_V)_{\text{RL}}$	$(A_\lambda/A_V)_{\text{Moneti}}$	wavelength $\lambda$ (in $\mu\text{m}$ )	$(A_\lambda/A_V)_{\text{RL}}$	$(A_\lambda/A_V)_{\text{Moneti}}$
0.55	1.000	1.000	11.00	0.060	0.102
0.64	0.748		11.50	0.047	0.084
0.65		0.769	12.00	0.037	0.072
0.79	0.482		12.50	0.030	0.063
0.80		0.558	13.00	0.027	0.057
1.00		0.410	13.50		0.055
1.21	0.282		14.00		0.055
1.25		0.280	14.50		0.056
1.65	0.175	0.174	15.00		0.057
2.20	0.112	0.111	15.50		0.059
2.50		0.096	16.00		0.061
3.00		0.092	16.50		0.064
3.45	0.058		17.00		0.068
3.50		0.072	17.50		0.071
4.00		0.053	18.00		0.073
4.50		0.051	18.50		0.073
4.80	0.023		19.00		0.072
5.00		0.049	19.50		0.070
5.50		0.048	20.00		0.068
6.00		0.046	20.50		0.066
6.50		0.045	21.00		0.064
7.00		0.044	21.50		0.063
7.50		0.043	22.00		0.061
8.00	0.020	0.046	22.50		0.059
8.50	0.043	0.063	23.00		0.056
9.00	0.074	0.099	23.50		0.054
9.50	0.087	0.145	24.00		0.052
10.00	0.083	0.143	> 24.0		$\propto \lambda^{-2}$
10.50	0.074	0.125			

Table A.4: Extinction laws of Rieke & Lebofsky (1985) and Moneti et al. (2001). See also fig. 2.2.

Appendix B

Large Figures

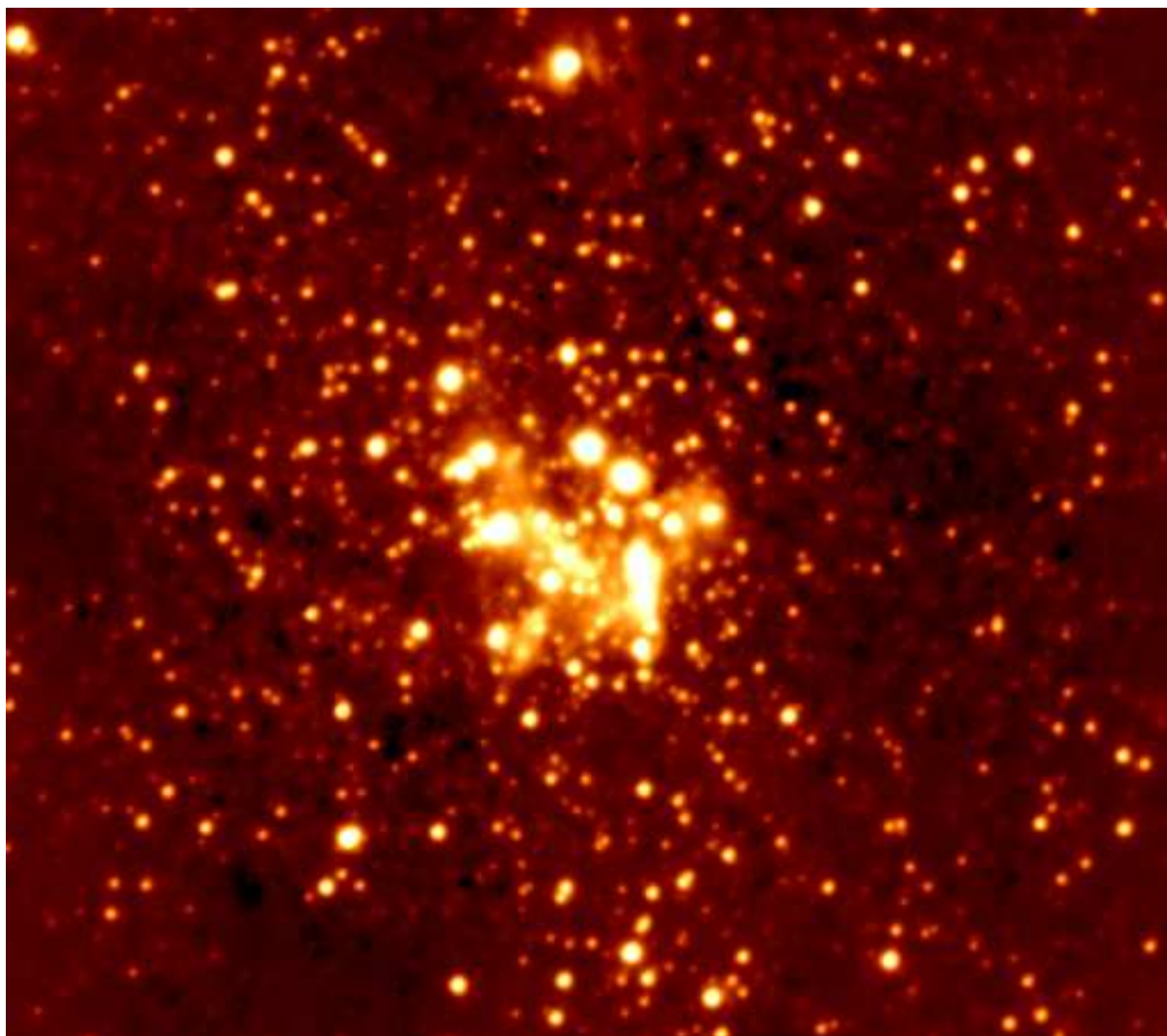


Figure B.1: Final ISAAC *L*-band image of the Galactic center. The field of view is  $72.6'' \times 72.6''$ .



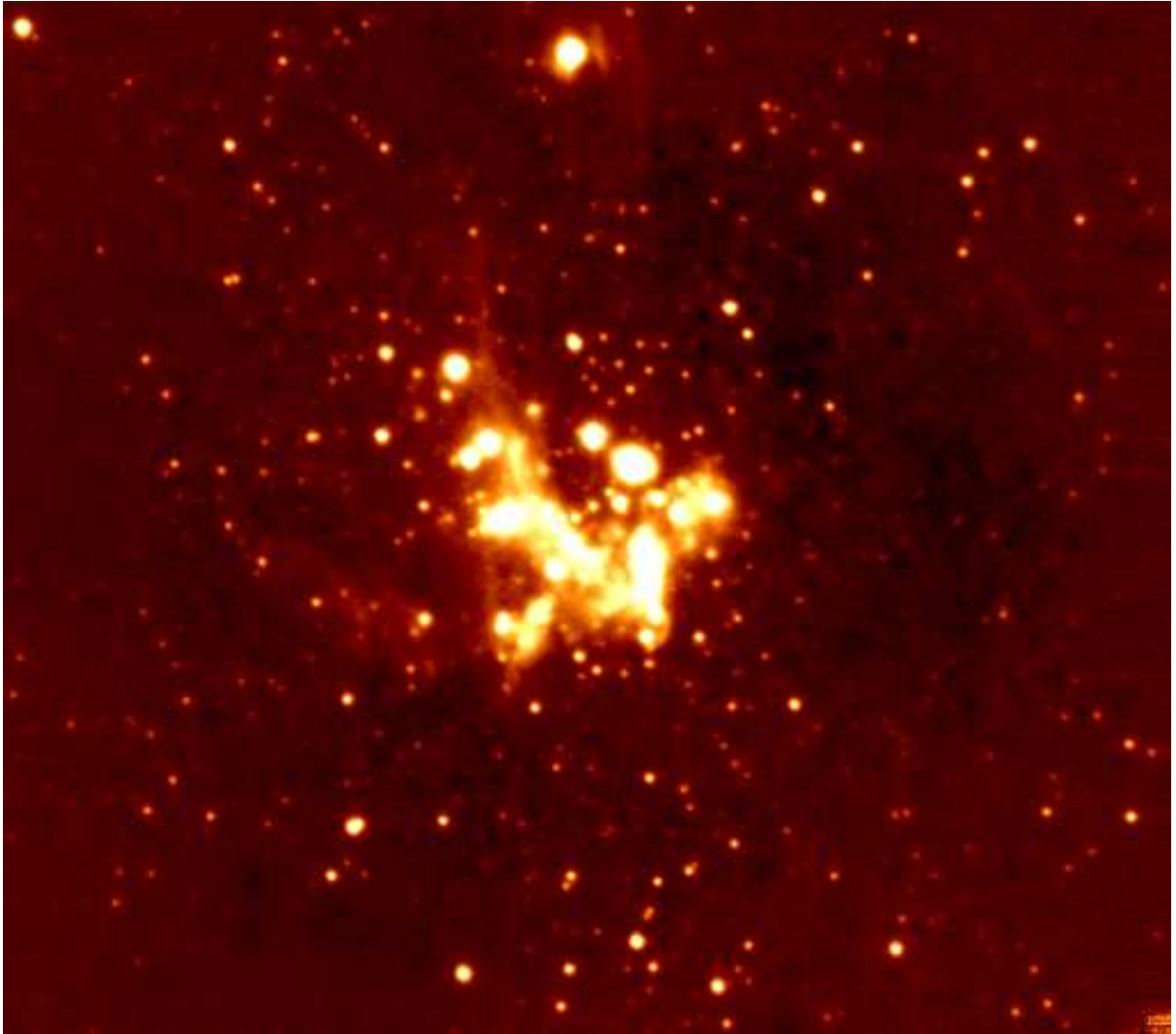


Figure B.2: Final ISAAC *M*-band image of the Galactic center. The field of view is  $72.6'' \times 72.6''$ .

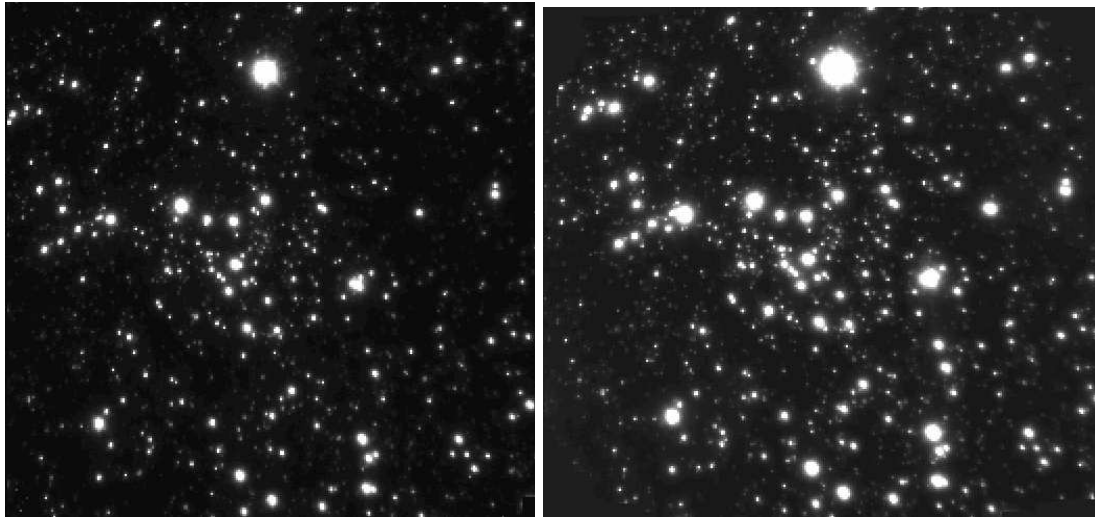


Figure B.3:  $H$ - (left) and  $K$ -band images obtained with NAOS/CONICA, reduced to a pixel scale of 0.071 arcseconds via rebinning.

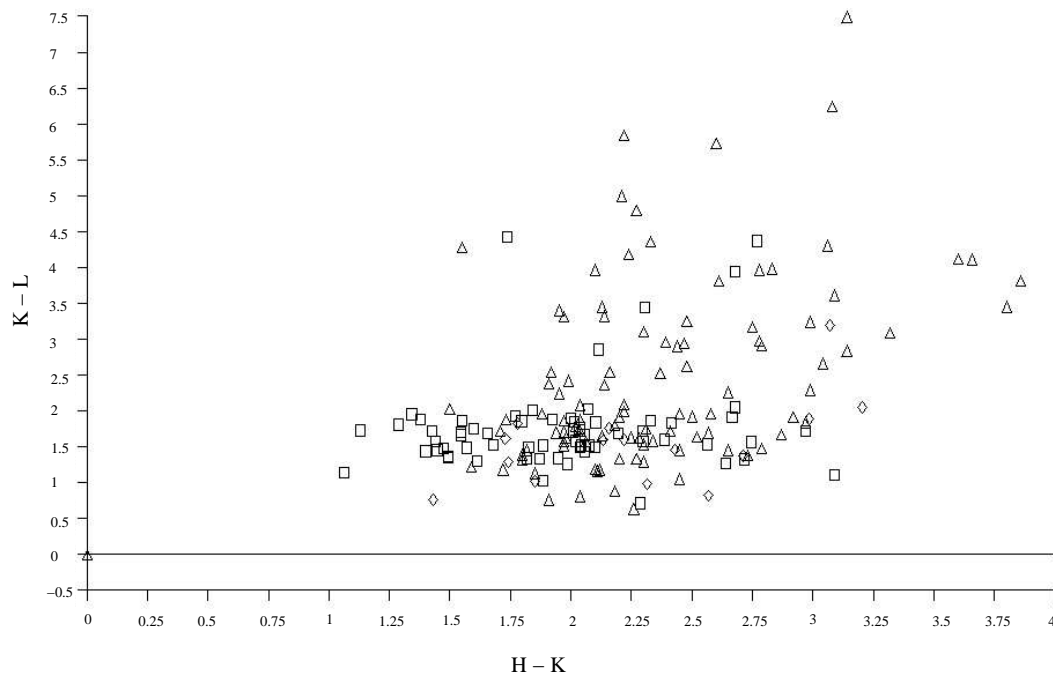


Figure B.4: Two-color diagram showing  $(K - L)_{\text{obs}}$  versus  $(H - K)_{\text{obs}}$ . The triangles represent sources from the inner  $18'' \times 18''$ , the squares represent brighter sources ( $m_L < 9.5$ ) and the diamonds a selection of fainter sources from outside this inner region.

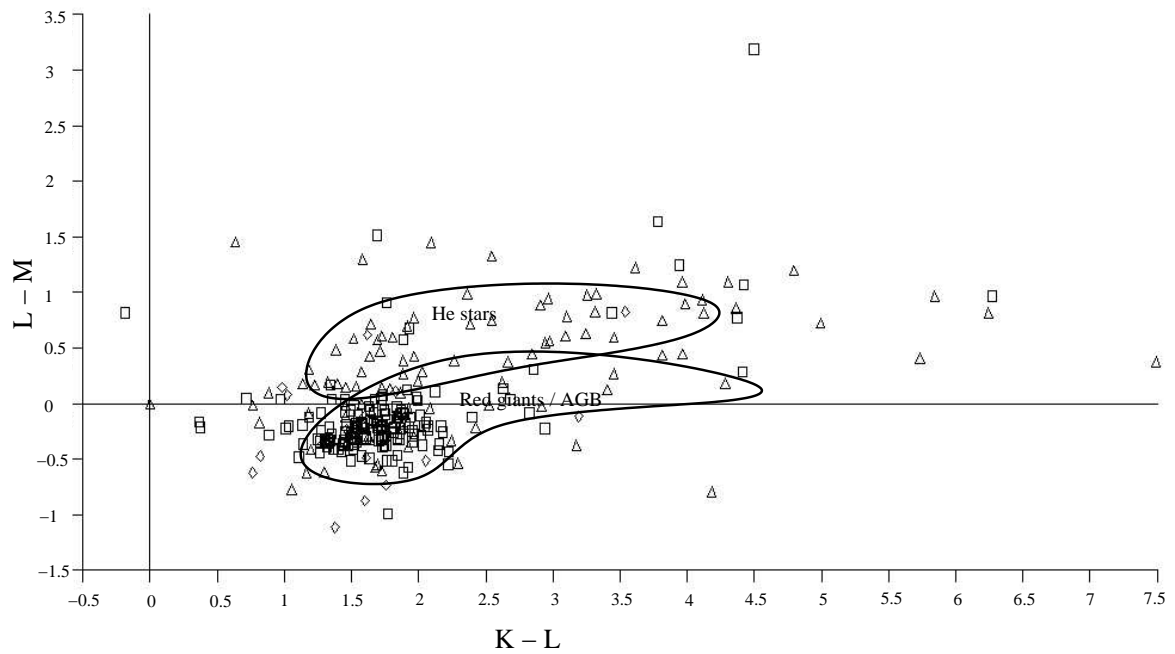


Figure B.5: Two-color diagram showing  $(L - M)_{\text{obs}}$  versus  $(K - L)_{\text{obs}}$ . The triangles represent sources from the inner  $18'' \times 18''$ , the squares represent brighter sources ( $m_L < 9.5$ ) and the diamonds a selection of fainter sources from outside this inner region. The marked areas fully contain the spectroscopically identified He stars and red giants / AGB stars from table A.1.

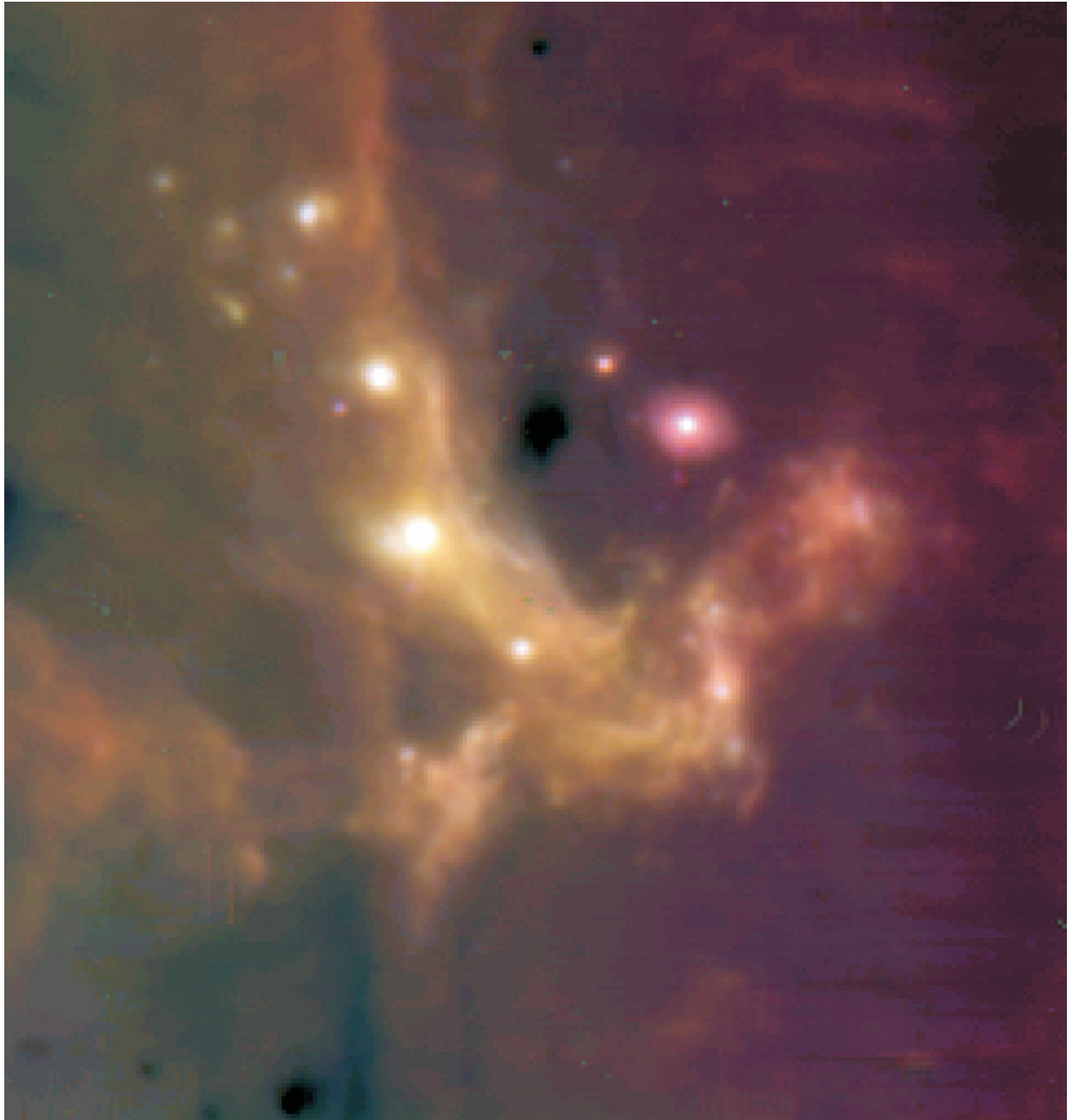


Figure B.6: VISIR *N*-band three-color composite view of the Galactic center. The blue channel is  $8.6 \mu\text{m}$ , green is  $11.3 \mu\text{m}$  and red is  $12.8 \mu\text{m}$ .

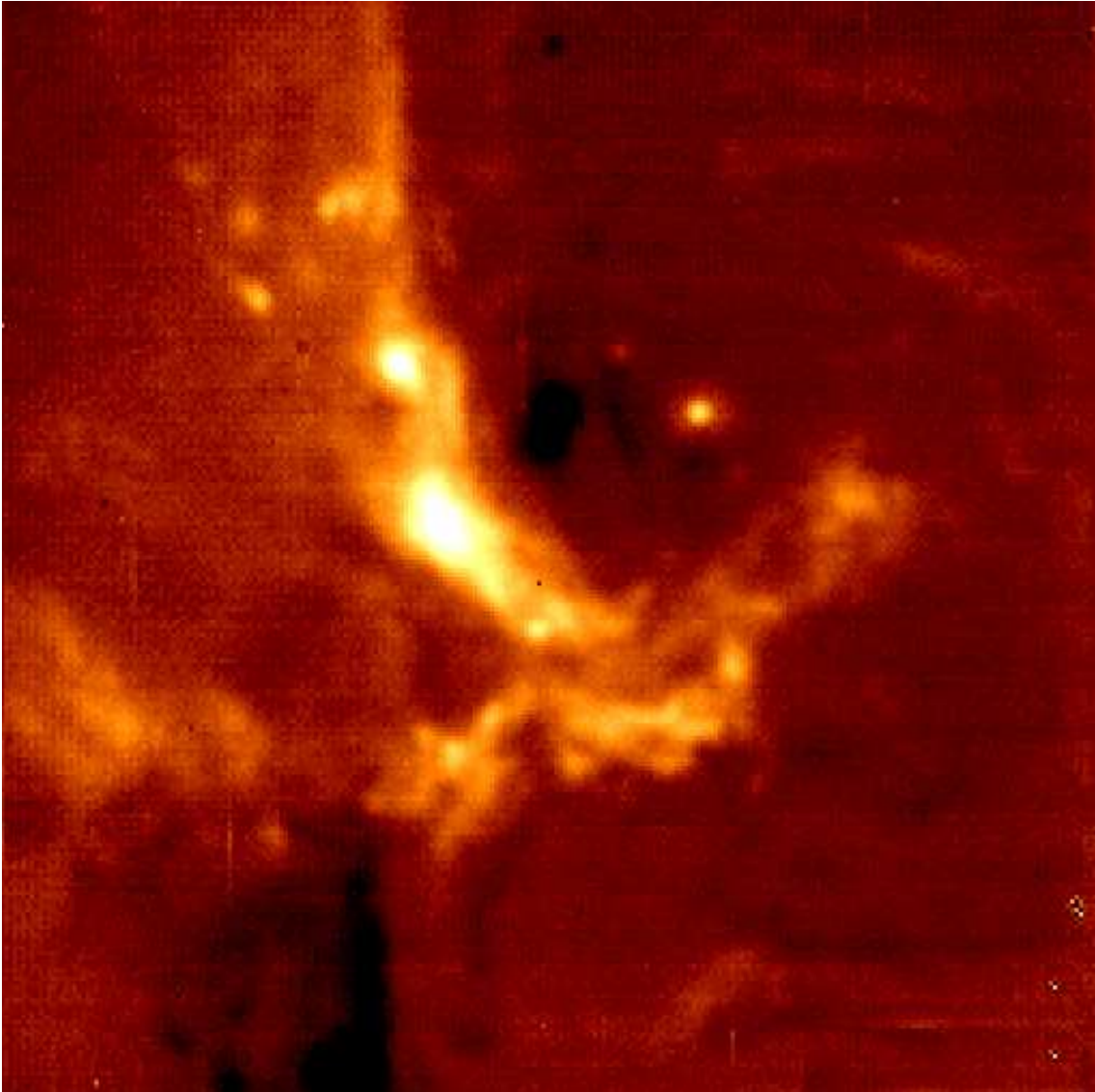


Figure B.7: VISIR  $19.5 \mu\text{m}$  image of the Galactic center. The field of view is  $32'' \times 32''$ .

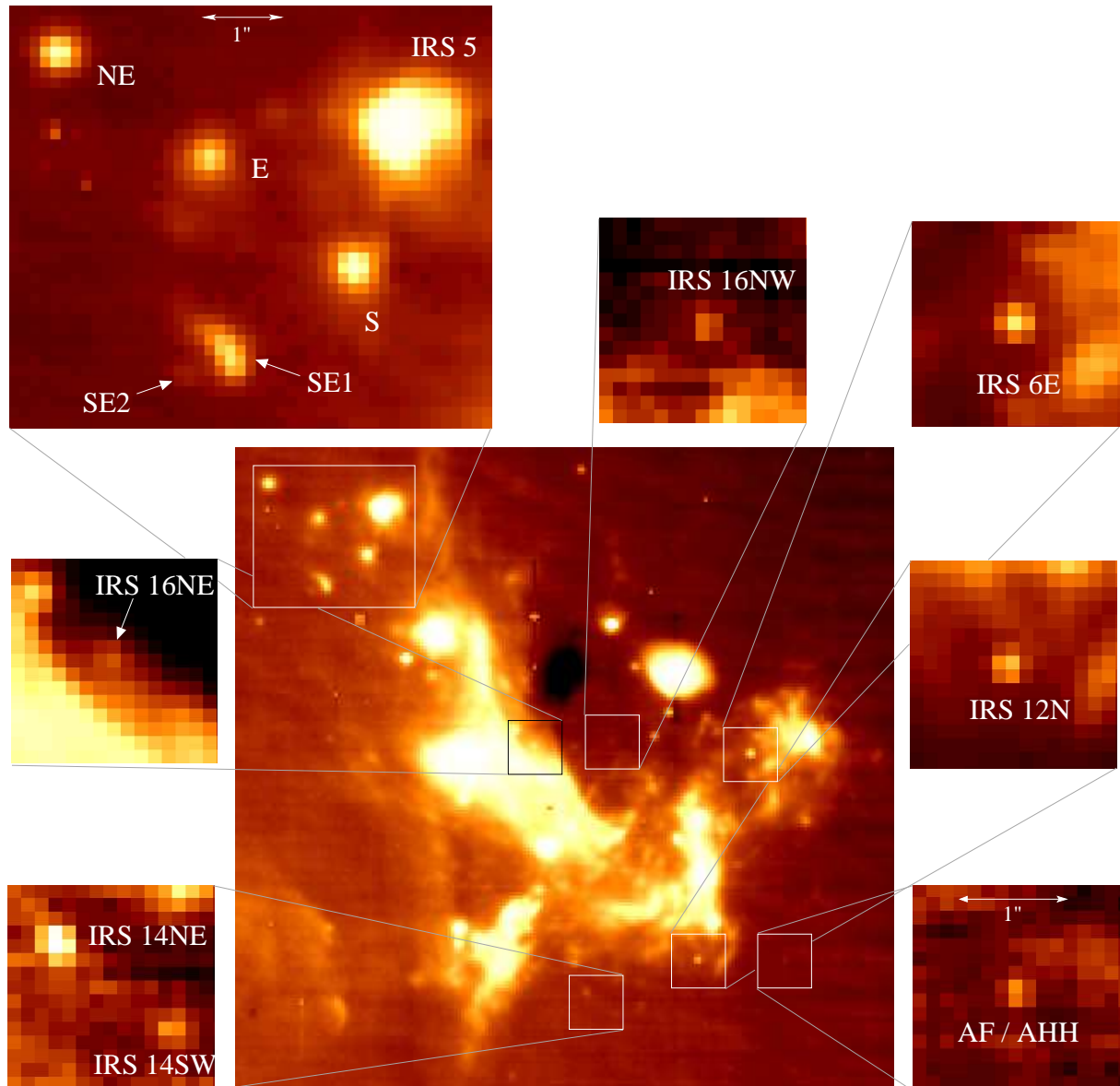


Figure B.8: VISIR 8.6  $\mu\text{m}$  view of the Galactic center. The field of view is approximately  $24'' \times 24''$ . The insets show enlarged views of the newly detected stars AF/AHH, IRS 6E, IRS 12N, IRS 14NE, IRS 14SW, IRS 16NE and IRS 16NW (see section 5), as well as the intriguing group of bright sources located to the east of IRS 5 (upper left, see section 5.4).

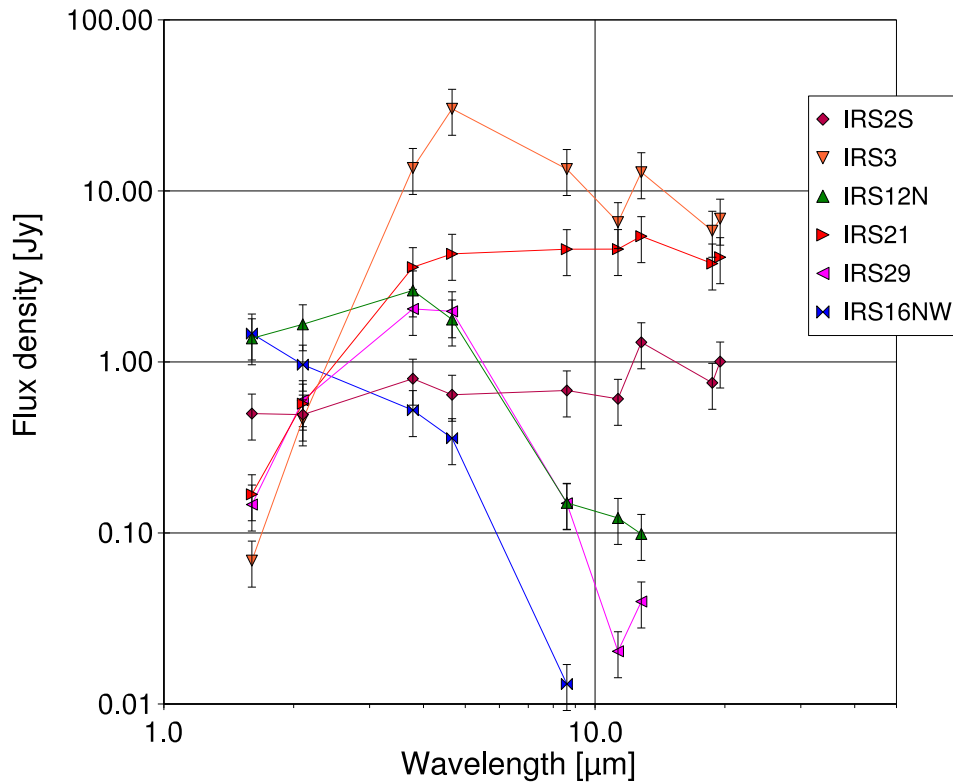


Figure B.9: Spectral energy distributions of typical Galactic center mid-infrared sources. They represent the types described in section 5.1: IRS 21 (red) is a luminous Northern Arm bow-shock source, IRS 2S (dark red) is a lower luminosity bow-shock source, IRS 12N (green) is a cool star, IRS 16NW is a relatively dust free hot star, IRS 29 (purple) is a dusty hot star (WC9, see text), while IRS 3 (orange) is unclassified.

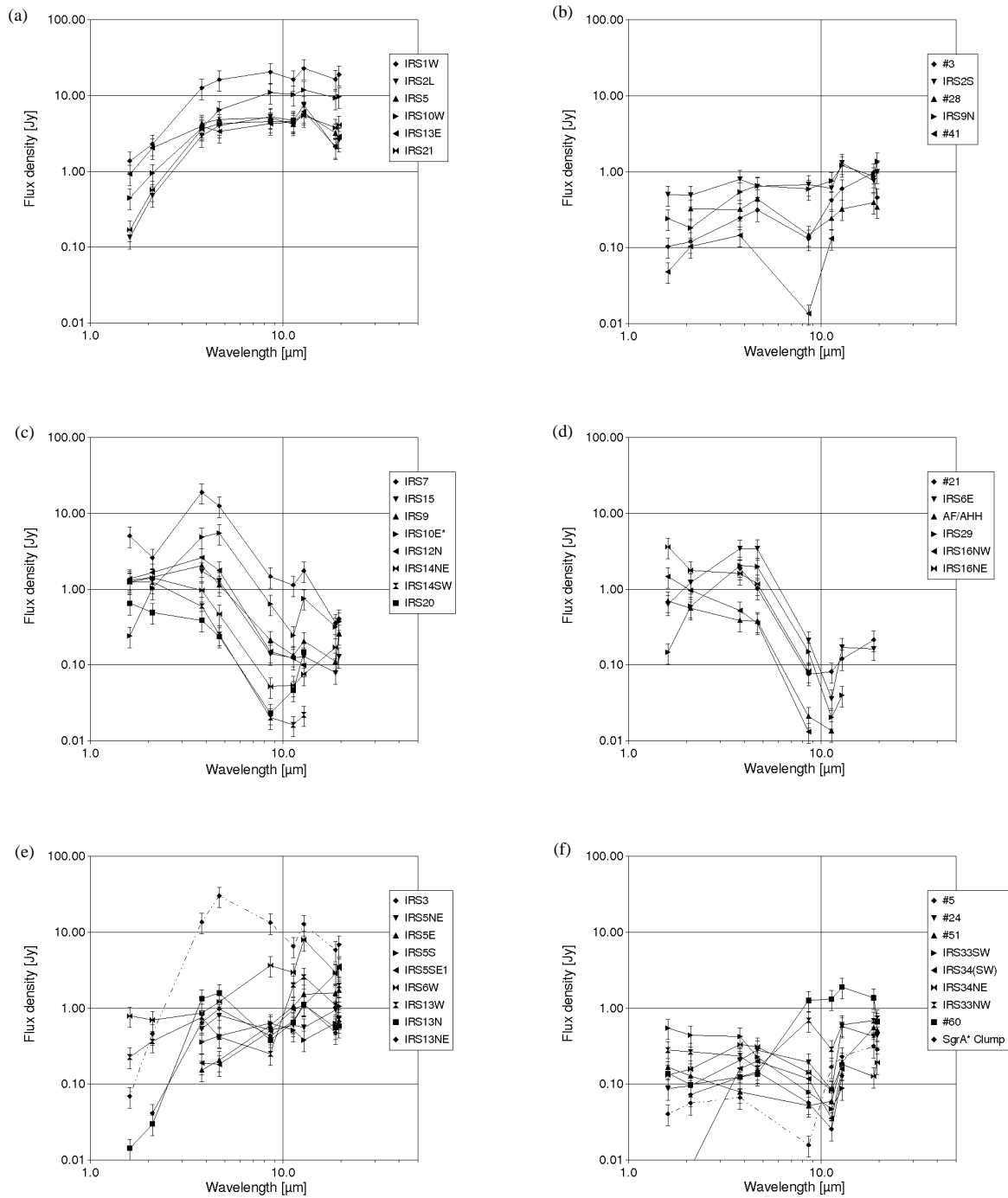


Figure B.10: Spectral energy distributions of Galactic center mid-infrared sources. The SEDs have been grouped by type, as described in section 5.1: (a) shows the typical luminous bow-shock sources, (b) shows lower luminosity bow-shock sources, (c) cool stars, (d) hot stars, while (e) and (f) show the SEDs of unclassified sources. In (e) and (f), IRS 3 and the Sgr A\* clump are distinguished by a dash-dotted line.



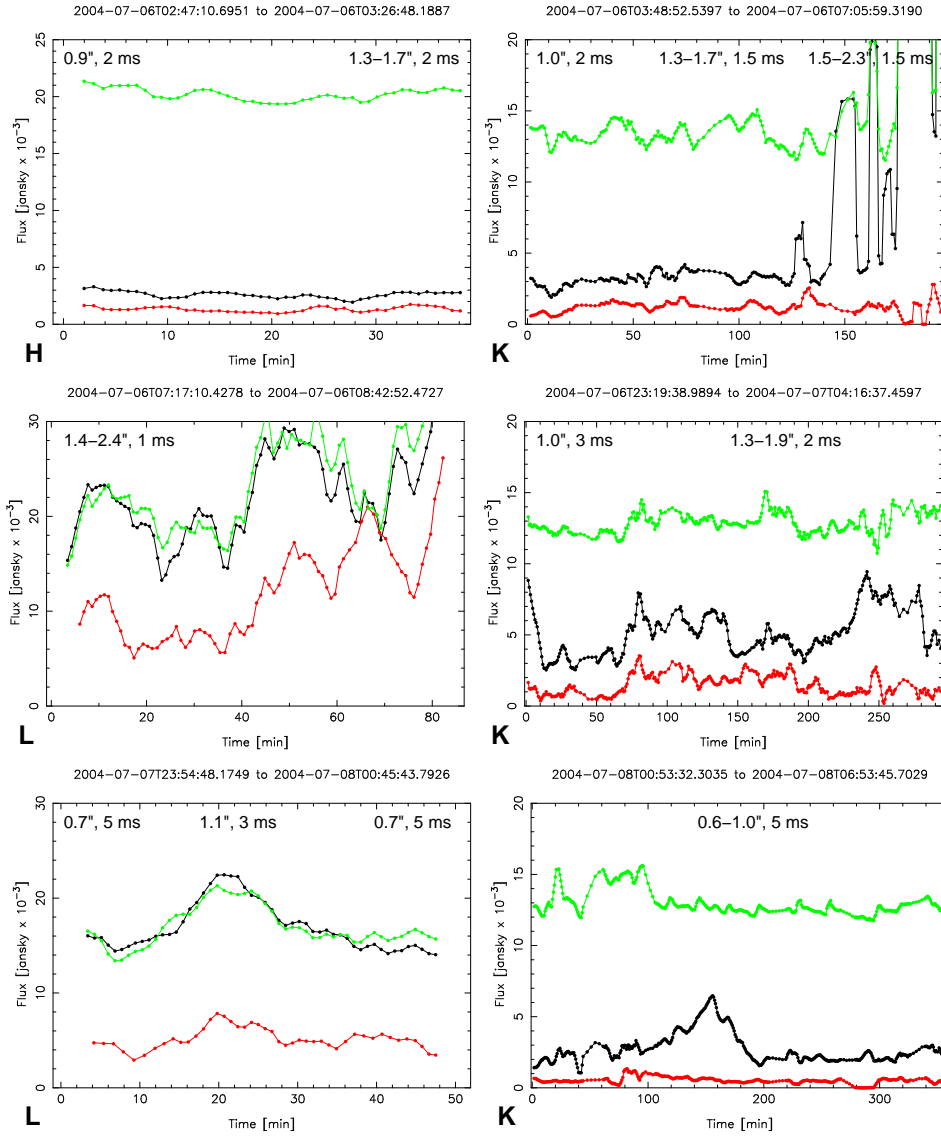


Figure B.11: Light curves of all NIR observations in July 2004. Shown are the dereddened flux densities of S1 (green), Sgr A\* (black), and a field free of stars (red). The data were smoothed with a sliding point window comprising five samples in case of the K- and H-band data, 9 samples in case of the L'-band data. Here, one sample corresponds to a photometric measurement on an individual image (i.e.  $\text{DIT} \times \text{NDIT}$  integration time, see table 3.2). The quality of the data is fairly variable, which is closely related to the seeing and coherence time of the atmosphere during the observations, resulting in variable AO performance. Seeing and atmospheric coherence time are indicated in the plots. Generally, the light curve of S1 and of the background (expected to be constant) give a good idea of the data quality and relative uncertainties of the observations. Values for seeing and coherence time are from the ESO Observatories Ambient Conditions Database.

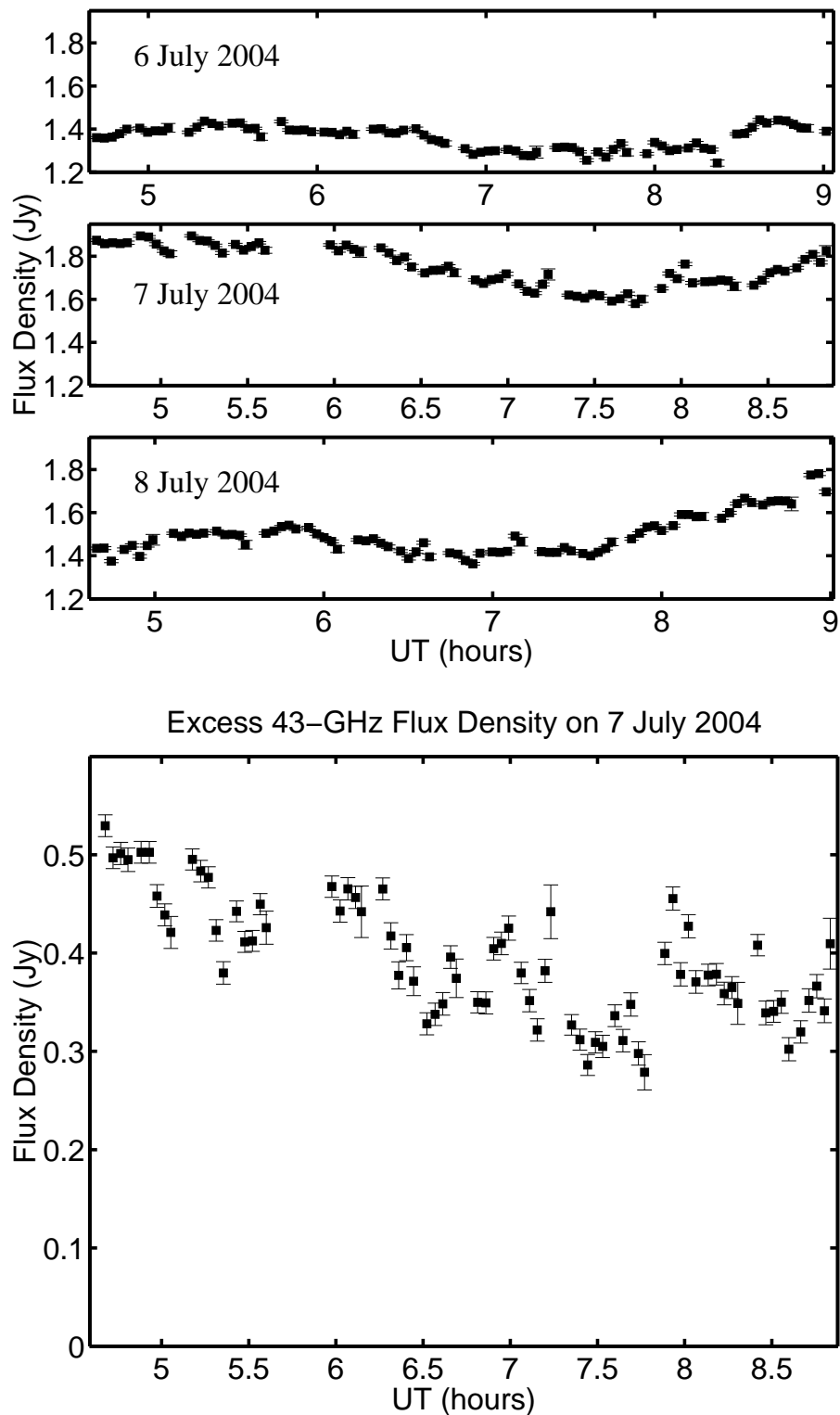


Figure B.12: VLA 43 GHz light curves. The top graphs show the correlated flux density as measured on 6, 7, and 8 of July (see tab. 3.1). The bottom graph shows the excess flux density on 7 July calculated as the difference between the data from this day and the mean of 6 and 8 July.

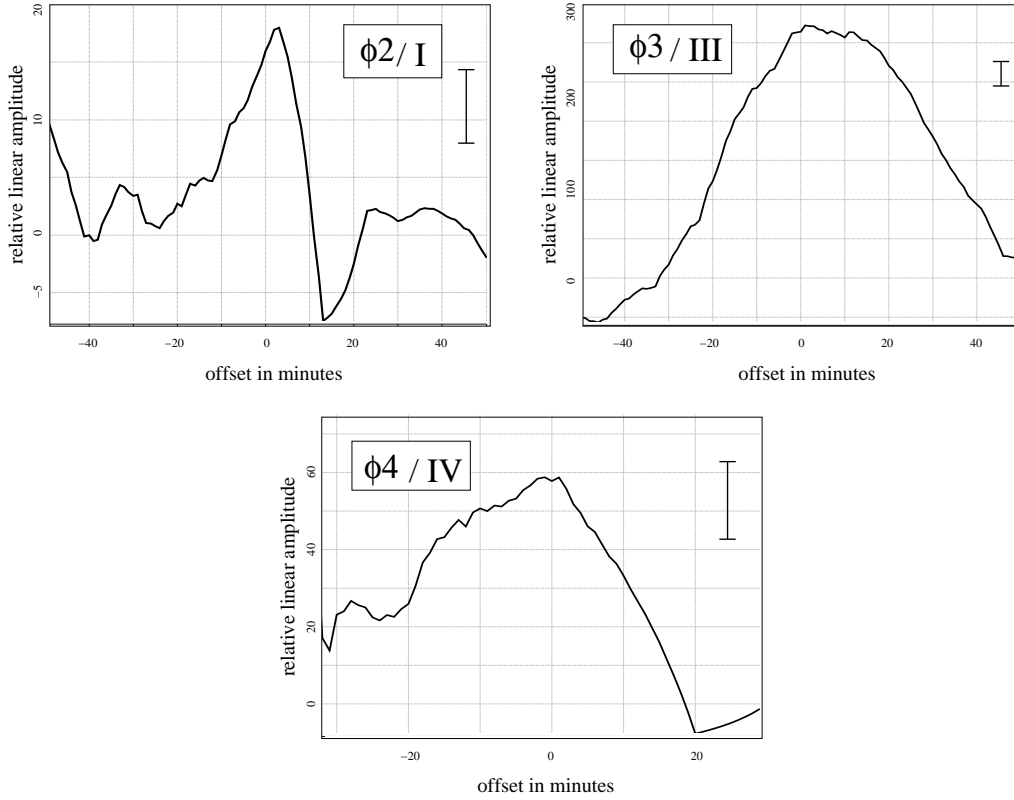


Figure B.13: Cross-correlation between the NIR data (40 s bins, 20 s integration time per image) and the X-ray data (10 minute bins) for the flares  $\phi 2/\text{I}$  (top left),  $\phi 3/\text{III}$  (top right), and  $\phi 4/\text{IV}$  (bottom; see tab. 6.2). Only the flare data overlapping in time (i.e.  $\approx 40$  minutes before until 20 minutes after 07 July 0.0 UT for  $\phi 2/\text{I}$ ,  $\approx 177$  minutes until 223 minutes after midnight for  $\phi 3/\text{III}$ , and  $\approx 223$  minutes until 256 minutes after midnight for  $\phi 4/\text{IV}$ ) were cross-correlated. The error bars indicate an estimate of the signal to noise ratio (SNR) derived from the SNR of the individual X-ray bins and the approximate number of bins averaged for each cross-correlation measurement. At a  $\sim 2.6$ , 9, and  $3\sigma$  level, respectively, the light curves indicate a simultaneous flare event around midnight corresponding to a time delay of less than 10 minutes (see text). For the flares  $\phi 3/\text{III}$  and  $\phi 4/\text{IV}$  the entire event was covered. The offsets are given in minutes.

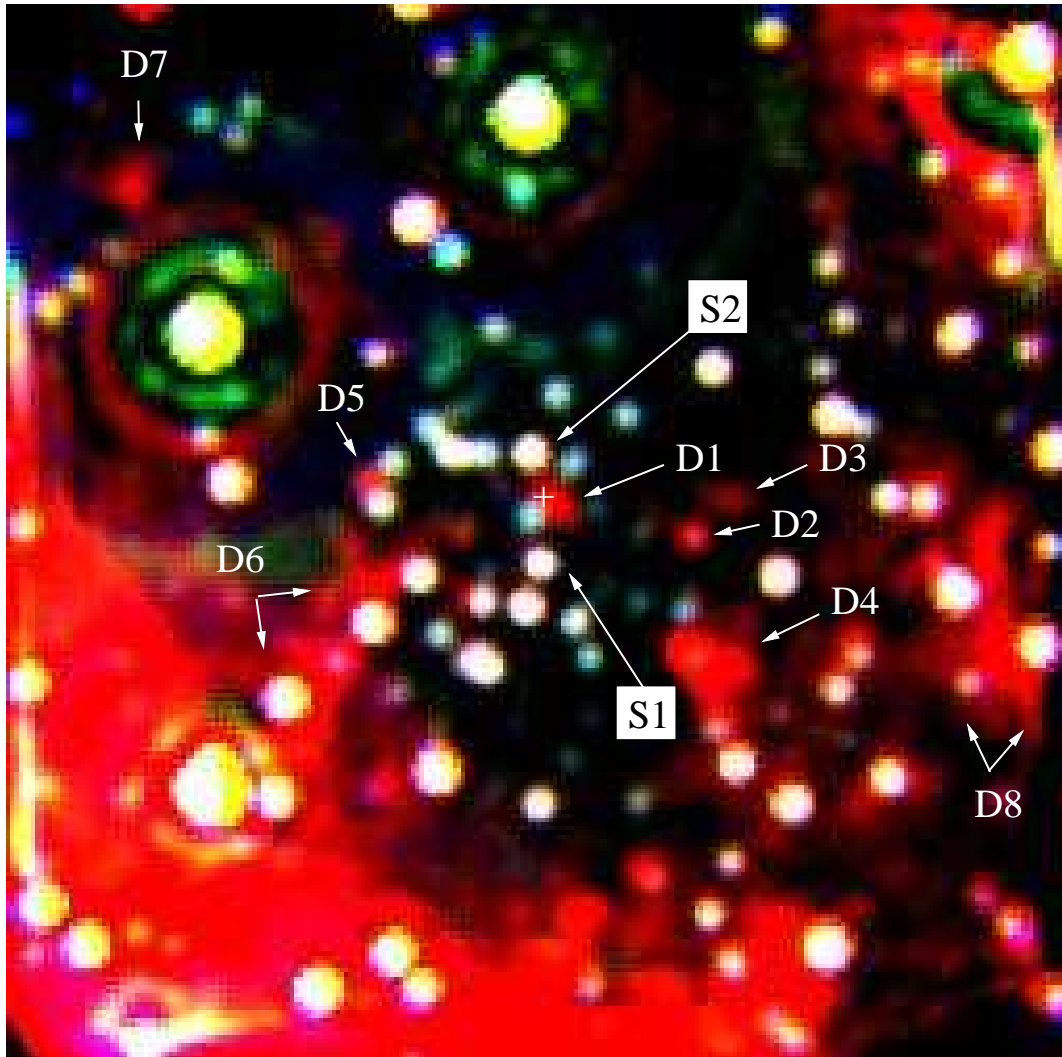


Figure B.14: *HKL'* multi-color image of the central  $2.6'' \times 2.6''$  as taken with NAOS/CONICA on 6 July 2004. North is up and East is to the left. *H* is blue, *K* is green, and *L'* is red. The white cross marks the position of Sgr A\*. This figure is a different representation of the data shown in fig. 6.6, covering a larger field of view. Immediately west of the position of Sgr A\* an extended red emission component (D1) is evident.

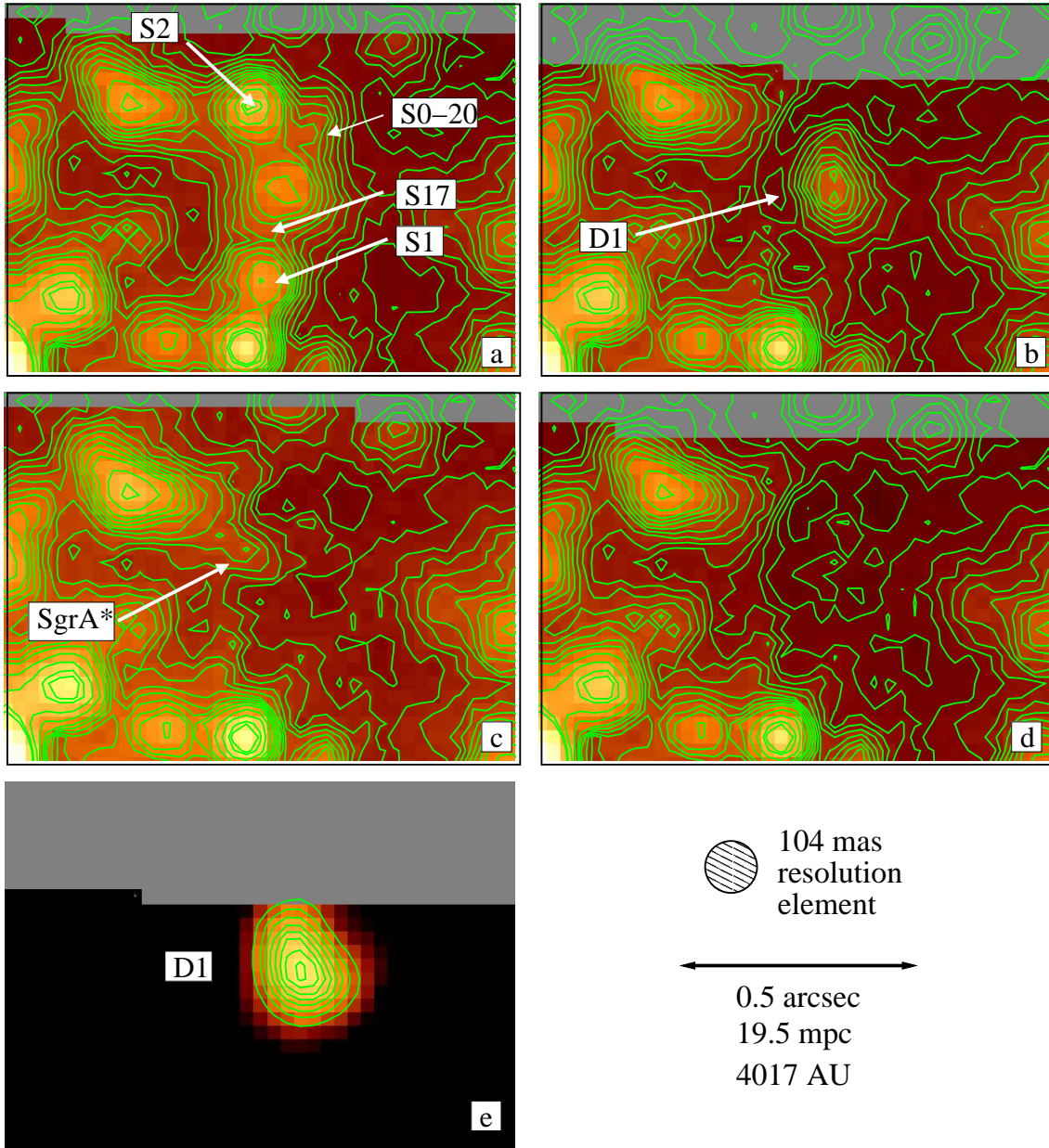


Figure B.15: The central  $0.76'' \times 1.06''$  shown in a combined color and contour map. The contour lines correspond to 4, 6, 8, 10, 12, 14, 16, 18, 20, 22, 24, 26, 30, 35, 40, 42 and 10, 14, 19, 24, 29, 33, 38, 43, 48, 52, 57, 62, 71, 83, 95, 98 % of the peak brightness of the star S2. Panel **a**) shows the complete image section in  $L'$  band. Panel **b**) shows the image section with scaled PSF subtraction of the sources S2 ( $L' = 12.78$ , used as a calibrator), S1 ( $L' = 13.80 \pm 0.12$ ), S17 ( $L' = 13.79 \pm 0.12$ ), S0-20 ( $L' = 13.89 \pm 0.13$ ), and Sgr A\* ( $L' = 14.1 \pm 0.2$ ). The dust component D1 ( $L' = 12.8 \pm 0.20$ ) is clearly visible. Panel **c**) shows the image section with D1 subtracted instead of Sgr A\*. In panel **d**) both Sgr A\* and D1 have been subtracted, while Panel **e**) shows the model of the dust component D1 by itself. The background in the central  $0.3''$  is flat and has an  $L'$  brightness of  $L' = 15$  per beam with a  $3\sigma$  deviation of less than  $\pm 0.42$  magnitudes.

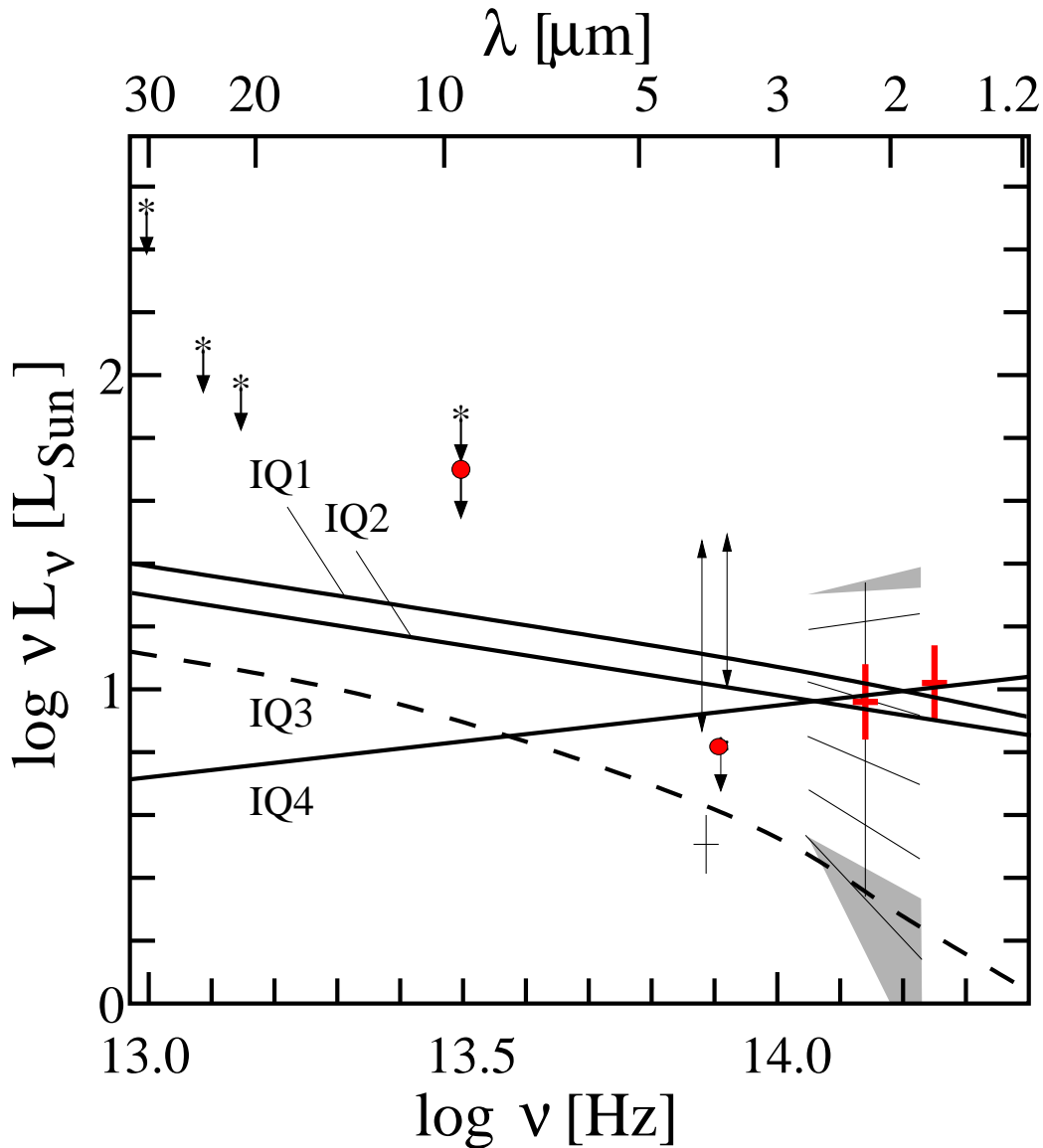


Figure B.16: The near- to mid-infrared  $\log(\nu L_\nu)$  spectrum of Sgr A\* compared to emission models during low flux density states. Red data points indicate the measurements described in this thesis. The  $\log(\nu L_\nu)$  values are based on the following data: The new quasi-simultaneous  $L'$ -,  $K$ - and  $H$ -band flux densities during the low near-infrared flux IQ-state are shown in red. The 30 μm and 24.3 μm flux density limits are taken from Telesco et al. (1996) and Serabyn et al. (1997), respectively; at 8.7 μm the resulting limit of about 100 mJy is lower than the value given by Stolovy et al. (1996); at 3.8 μm the obtained IQ flux density value ( $19 \pm 5$  mJy) as well as the IQ flux density values (6.4 - 17.5 mJy) given by Genzel et al. (2003) and the range of flux densities (4 - 17 mJy,  $1.3 \pm 0.3$  mJy) given by Ghez et al. (2004b, 2005) are shown. For clarity the latter two ranges were displaced slightly in frequency with respect to the center of the  $L'$ -band. In addition the representative SSC models IQ1-IQ4 are plotted, with parameters as listed in tab. 6.4.

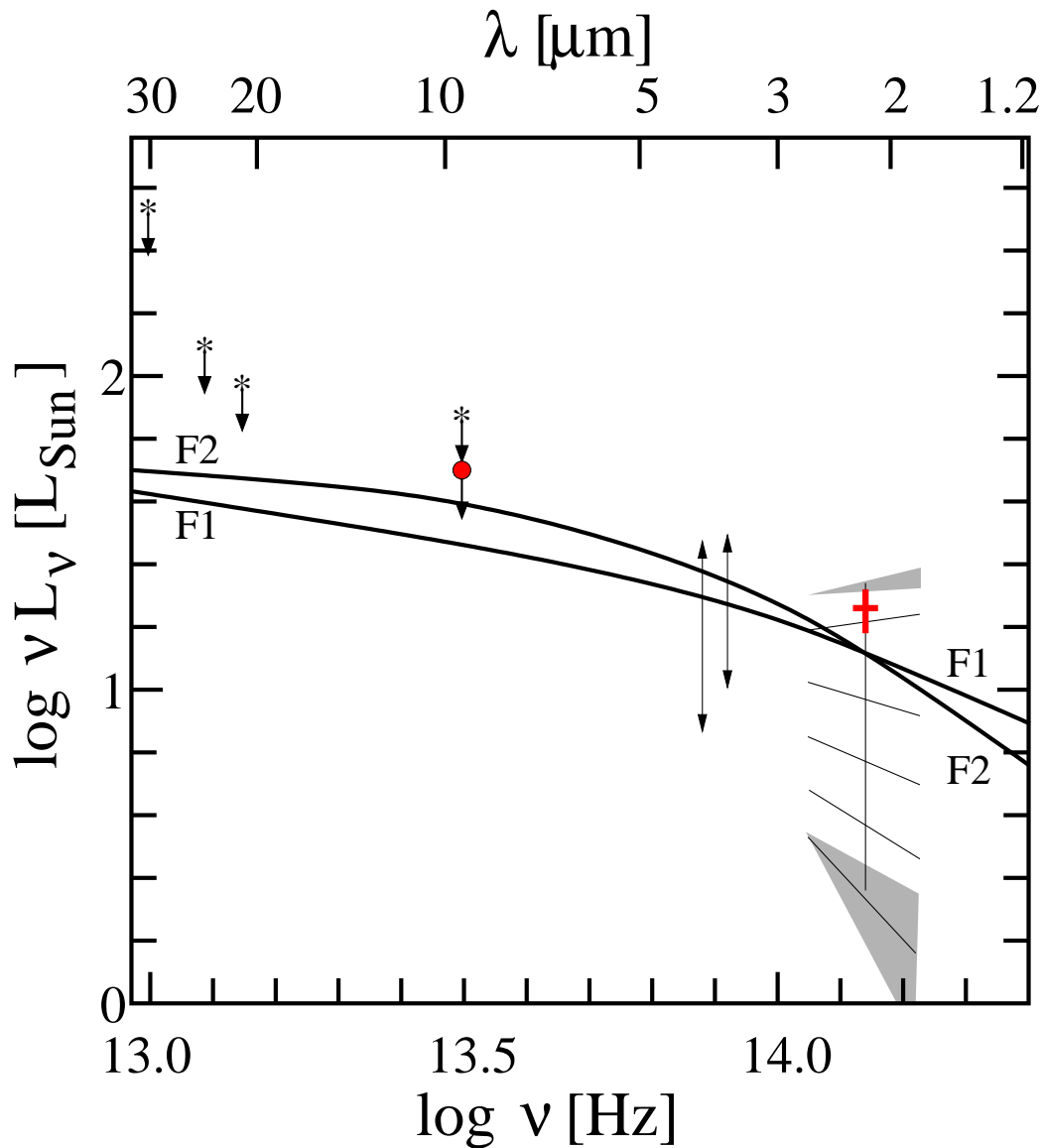


Figure B.17: The near- to mid-infrared  $\log(\nu L_\nu)$  spectrum of Sgr A\* compared to flare emission models for the strong X-ray/near-infrared flare  $\phi 3/\text{III}$ . (See also caption of fig. 6.6). Finally the  $K$ -band spectra of flares including the slopes (grey shaded area) as measured by Eisenhauer et al. (2005) and Ghez et al. (2005) are shown. The thin lines between the grey shaded areas indicate how the slope may change as a function of flare flux as suggested by Ghez et al. (2005). In addition the representative SSC flare models F1 and F2 are plotted with parameters as listed in tab. 6.2.





# Bibliography

- Ageorges, N., Lidman, C., Brandner, W., & Moutou, C. 2005, Very Large Telescope: NAOS-CONICA User Manual, European Southern Observatory
- Baganoff, F. K., Bautz, M. W., Brandt, W. N., et al. 2001, *Nature*, 413, 45
- Baganoff, F. K., Bautz, M. W., Ricker, G. R., et al. 2002, in *Bulletin of the American Astronomical Society*, Vol. 34, *Bulletin of the American Astronomical Society*, 1153–+
- Baganoff, F. K., Maeda, Y., Morris, M., et al. 2003, *ApJ*, 591, 891
- Ball, G. H., Narayan, R., & Quataert, E. 2001, *ApJ*, 552, 221
- Becklin, E. E., Gatley, I., & Werner, M. W. 1982, *ApJ*, 258, 135
- Becklin, E. E., Matthews, K., Neugebauer, G., & Willner, S. P. 1978, *ApJ*, 219, 121
- Becklin, E. E. & Neugebauer, G. 1968, *ApJ*, 151, 145
- Becklin, E. E. & Neugebauer, G. 1969, *ApJ*, 157, L31+
- Bélangier, G., Goldwurm, A., Melia, F., et al. 2005, *ApJ*, 635, 1095
- Blandford, R. D. & Begelman, M. C. 1999, *MNRAS*, 303, L1
- Blandford, R. D. & Konigl, A. 1979, *ApJ*, 232, 34
- Blandford, R. D. & McKee, C. F. 1977, *MNRAS*, 180, 343
- Blum, R. D., Sellgren, K., & Depoy, D. L. 1996, *ApJ*, 470, 864
- Bogdan, T. G. & Schlickeiser, R. 1985, *A&A*, 143, 23
- Bower, G. C., Falcke, H., Herrnstein, R. M., et al. 2004, *Science*, 304, 704
- Bower, G. C., Falcke, H., Sault, R. J., & Backer, D. C. 2002, *ApJ*, 571, 843
- Bower, G. C., Falcke, H., Wright, M. C., & Backer, D. C. 2005, *ApJ*, 618, L29
- Bower, G. C., Wright, M. C. H., Falcke, H., & Backer, D. C. 2003, *ApJ*, 588, 331
- Bregman, J. N. 1985, *ApJ*, 288, 32
- Burbidge, G. R. 1956, *ApJ*, 124, 416
- Clénet, Y., Rouan, D., Gendron, E., et al. 2004a, *A&A*, 417, L15

- Clénet, Y., Rouan, D., Gendron, E., et al. 2001, *A&A*, 376, 124
- Clénet, Y., Rouan, D., Gratadour, D., et al. 2004b, *A&A*, 424, L21
- Clénet, Y., Rouan, D., Gratadour, D., et al. 2005, *A&A*, 439, L9
- Cotera, A. & Rigaut, F. 2001, *Galactic Center Newsletter*, 12, 4
- Cotera, A. S., Simpson, J. P., Erickson, E. F., et al. 1999, *ApJ*, 510, 747
- Cuby, J. G., Lidman, C., Moutou, C., Johnson, R., & Doublier, V. 2002, *Very Large Telescope: ISAAC User Manual*, European Southern Observatory
- Davidge, T. J., Simons, D. A., Rigaut, F., Doyon, R., & Crampton, D. 1997, *AJ*, 114, 2586
- Depoy, D. L. 1990, in *ASP Conf. Ser. 14: Astrophysics with Infrared Arrays*, 219–+
- Depoy, D. L. & Sharp, N. A. 1991, *AJ*, 101, 1324
- Diolaiti, E., Bendinelli, O., Bonaccini, D., et al. 2000, *A&AS*, 147, 335
- Draine, B. T. 1989, in *Infrared Spectroscopy in Astronomy*, 93–98
- Draine, B. T. & Lee, H. M. 1984, *ApJ*, 285, 89
- Eckart, A., Baganoff, F. K., Morris, M., et al. 2004a, *A&A*, 427, 1
- Eckart, A., Baganoff, F. K., Schödel, R., et al. 2006a, *A&A*, 450, 535
- Eckart, A., Bertram, T., Mouawad, N., et al. 2003a, *Ap&SS*, 286, 269
- Eckart, A. & Genzel, R. 1996, *Nature*, 383, 415
- Eckart, A., Genzel, R., Ott, T., & Schödel, R. 2002, *MNRAS*, 331, 917
- Eckart, A., Hofmann, R., Duhoux, P., Genzel, R., & Drapatz, S. 1992, in *High-Resolution Imaging by Interferometry*, 175–+
- Eckart, A., Moulataka, J., Viehmann, T., Straubmeier, C., & Mouawad, N. 2004b, *ApJ*, 602, 760
- Eckart, A., Moulataka, J., Viehmann, T., et al. 2003b, *Astronomische Nachrichten Supplement*, 324, 521
- Eckart, A., Moulataka, J., Viehmann, T., et al. 2003c, in *Astron. Nachr.324, S1: Supplement: Proceedings of the Galactic Center Workshop 2002 - The central 300 parsecs of the Milky Way*, 557–561
- Eckart, A., Moulataka, J., Viehmann, T., et al. 2005, in *Science with Adaptive Optics*, ed. W. Brandner & M. E. Kasper, 279–+
- Eckart, A., Ott, T., & Genzel, R. 1999, *A&A*, 352, L22

- Eckart, A., Schödel, R., Straubmeier, C., et al. 2006b, in Presented at the Society of Photo-Optical Instrumentation Engineers (SPIE) Conference, Vol. 6268, Advances in Stellar Interferometry. Edited by Monnier, John D.; Schöller, Markus; Danchi, William C.. Proceedings of the SPIE, Volume 6268, pp. 62681J (2006).
- Eisenhauer, F., Genzel, R., Alexander, T., et al. 2005, *ApJ*, 628, 246
- Eisenhauer, F., Schödel, R., Genzel, R., et al. 2003, *ApJ*, 597, L121
- Geballe, T. R., Rigaut, F., Roy, J.-R., & Draine, B. T. 2004, *ApJ*, 602, 770
- Gehrz, R. 1989, in IAU Symposium, Vol. 135, Interstellar Dust, ed. L. J. Allamandola & A. G. G. M. Tielens, 445–+
- Genzel, R., Eckart, A., Ott, T., & Eisenhauer, F. 1997, *MNRAS*, 291, 219
- Genzel, R., Pichon, C., Eckart, A., Gerhard, O. E., & Ott, T. 2000, *MNRAS*, 317, 348
- Genzel, R., Schödel, R., Ott, T., et al. 2003, *ApJ*, 594, 812
- Gezari, D., Dwek, E., & Varosi, F. 1996, in IAU Symp. 169: Unsolved Problems of the Milky Way, 231–+
- Gezari, D. Y., Shu, P., Lamb, G., et al. 1985, *ApJ*, 299, 1007
- Ghez, A. M., Duchêne, G., Matthews, K., et al. 2003, *ApJ*, 586, L127
- Ghez, A. M., Hornstein, S. D., Bouchez, A., et al. 2004a, in Bulletin of the American Astronomical Society, 1384–+
- Ghez, A. M., Klein, B. L., Morris, M., & Becklin, E. E. 1998, *ApJ*, 509, 678
- Ghez, A. M., Morris, M., Becklin, E. E., Tanner, A., & Kremenek, T. 2000, *Nature*, 407, 349
- Ghez, A. M., Salim, S., Hornstein, S. D., et al. 2005, *ApJ*, 620, 744
- Ghez, A. M., Wright, S. A., Matthews, K., et al. 2004b, *ApJ*, 601, L159
- Goldwurm, A., Brion, E., Goldoni, P., et al. 2003, *ApJ*, 584, 751
- Gould, R. J. 1979, *A&A*, 76, 306
- Herrnstein, R. M., Zhao, J.-H., Bower, G. C., & Goss, W. M. 2004, *AJ*, 127, 3399
- Ho, P. T. P., Moran, J. M., & Lo, K. Y. 2004, *ApJ*, 616, L1
- Høg, E., Fabricius, C., Makarov, V. V., et al. 2000, *A&A*, 355, L27
- Hornstein, S. D., Ghez, A. M., Tanner, A., et al. 2002, *ApJ*, 577, L9
- Horrobin, M., Eisenhauer, F., Tecza, M., et al. 2004, *Astronomische Nachrichten*, 325, 88
- Igumenshchev, I. V. 2002, *ApJ*, 577, L31
- King, I. R. 1971, *PASP*, 83, 199

- Koornneef, J. 1983, *A&A*, 128, 84
- Kormendy, J. 1973, *AJ*, 78, 255
- Krabbe, A., Genzel, R., Eckart, A., et al. 1995, *ApJ*, 447, L95+
- Lacy, J. H., Baas, F., Townes, C. H., & Geballe, T. R. 1979, *ApJ*, 227, L17
- Lacy, J. H., Townes, C. H., Geballe, T. R., & Hollenbach, D. J. 1980, *ApJ*, 241, 132
- Lagage, P.-O., Pel, J.-W., Claret, A., et al. 2003, in *Instrument Design and Performance for Optical/Infrared Ground-based Telescopes*. Edited by Iye, Masanori; Moorwood, Alan F. M. *Proceedings of the SPIE*, Volume 4841, pp. 923-931 (2003)., 923–931
- Latvakoski, H. M., Stacey, G. J., Gull, G. E., & Hayward, T. L. 1999, *ApJ*, 511, 761
- Leinert, C., Allard, F., Richichi, A., & Hauschildt, P. H. 2000, *A&A*, 353, 691
- Liu, S., Melia, F., & Petrosian, V. 2006, *ApJ*, 636, 798
- Low, F. J., Kleinmann, D. E., Forbes, F. F., & Aumann, H. H. 1969, *ApJ*, 157, L97+
- Lutz, D. 1999, in *ESA SP-427: The Universe as Seen by ISO*, ed. P. Cox & M. Kessler, 623–+
- Lutz, D., Feuchtgruber, H., Genzel, R., et al. 1996, *A&A*, 315, L269
- Maillard, J. P., Paumard, T., Stolovy, S. R., & Rigaut, F. 2004, *A&A*, 423, 155
- Marchenko, S. V., Moffat, A. F. J., & Grosdidier, Y. 1999, *ApJ*, 522, 433
- Markoff, S., Falcke, H., Yuan, F., & Biermann, P. L. 2001, *A&A*, 379, L13
- Marscher, A. P. 1983, *ApJ*, 264, 296
- Mathis, J. S. 1990, *ARA&A*, 28, 37
- Mathis, J. S., Rumpl, W., & Nordsieck, K. H. 1977, *ApJ*, 217, 425
- Melia, F. & Falcke, H. 2001, *ARA&A*, 39, 309
- Moneti, A., Stolovy, S., Blommaert, J. A. D. L., Figer, D. F., & Najarro, F. 2001, *A&A*, 366, 106
- Moultaka, J., Eckart, A., Schödel, R., Viehmann, T., & Najarro, F. 2005, *A&A*, 443, 163
- Moultaka, J., Eckart, A., Viehmann, T., et al. 2004a, *A&A*, 425, 529
- Moultaka, J., Eckart, A., Viehmann, T., & Schödel, R. 2006, *Journal of Physics Conference Series*, 54, 57
- Moultaka, J., Eckart, A., Viehmann, T., et al. 2004b, in *IAU Symposium, Vol. 222, The Interplay Among Black Holes, Stars and ISM in Galactic Nuclei*, ed. T. Storchi-Bergmann, L. C. Ho, & H. R. Schmitt, 141–144
- Najarro, F., Krabbe, A., Genzel, R., et al. 1997, *A&A*, 325, 700

- Narayan, R., Quataert, E., Igumenshchev, I. V., & Abramowicz, M. A. 2002, *ApJ*, 577, 295
- Narayan, R., Yi, I., & Mahadevan, R. 1995, *Nature*, 374, 623
- Ott, T., Eckart, A., & Genzel, R. 1999, *ApJ*, 523, 248
- Porquet, D., Predehl, P., Aschenbach, B., et al. 2003, *A&A*, 407, L17
- Pott, J.-U., Eckart, A., Glindemann, A., et al. 2005, *The Messenger*, 119, 43
- Pott, J.-U., Glindemann, A., Eckart, A., et al. 2004, in Presented at the Society of Photo-Optical Instrumentation Engineers (SPIE) Conference, Vol. 5491, *New Frontiers in Stellar Interferometry*, Proceedings of SPIE Volume 5491. Edited by Wesley A. Traub. Bellingham, WA: The International Society for Optical Engineering, 2004., p.126, ed. W. A. Traub, 126–+
- Quataert, E. 2003, *ArXiv Astrophysics e-prints*
- Quataert, E. & Gruzinov, A. 2000, *ApJ*, 539, 809
- Reid, M. J. 1993, *ARA&A*, 31, 345
- Reid, M. J., Readhead, A. C. S., Vermeulen, R. C., & Treuhaft, R. N. 1999, *ApJ*, 524, 816
- Rieke, G. H. & Lebofsky, M. J. 1985, *ApJ*, 288, 618
- Rieke, G. H., Rieke, M. J., & Paul, A. E. 1989, *ApJ*, 336, 752
- Rieke, M. J. 1987, in *Nearly Normal Galaxies. From the Planck Time to the Present*, 90–95
- Rigaut, F., Geballe, T. R., Roy, J.-R., & Draine, B. T. 2003, *Astronomische Nachrichten Supplement*, 324, 551
- Sanders, D. B., Scoville, N. Z., & Solomon, P. M. 1985, *ApJ*, 289, 373
- Schödel, R., Eckart, A., Mužić, K., et al. 2007, *A&A*, 462, L1
- Schödel, R., Ott, T., Genzel, R., et al. 2003, *ApJ*, 596, 1015
- Schödel, R., Ott, T., Genzel, R., et al. 2002, *Nature*, 419, 694
- Scoville, N. Z., Stolovy, S. R., Rieke, M., Christopher, M., & Yusef-Zadeh, F. 2003, *ApJ*, 594, 294
- Sedlmayr, E. 1989, in *IAU Symposium*, Vol. 135, *Interstellar Dust*, ed. L. J. Allamandola & A. G. G. M. Tielens, 467–+
- Serabyn, E., Carlstrom, J., Lay, O., et al. 1997, *ApJ*, 490, L77+
- Shu, F. H. 1982, *The Physical Universe, An introduction to Astronomy* (University Science Books)
- Simons, D. A. & Becklin, E. E. 1996, *AJ*, 111, 1908

- Spitzer, L. 1978, *Physical processes in the interstellar medium* (New York Wiley-Interscience, 1978. 333 p.)
- Stolovy, S. R., Hayward, T. L., & Herter, T. 1996, *ApJ*, 470, L45+
- Tamura, M., Werner, M. W., Becklin, E. E., & Phinney, E. S. 1996, *ApJ*, 467, 645
- Tanner, A., Ghez, A. M., Morris, M., et al. 2002, *ApJ*, 575, 860
- Tanner, A., Ghez, A. M., Morris, M. R., & Christou, J. C. 2005, *ApJ*, 624, 742
- Tanner, A. M., Ghez, A. M., Morris, M., & Becklin, E. E. 2003, *Astronomische Nachrichten Supplement*, 324, 597
- Telesco, C. M., Davidson, J. A., & Werner, M. W. 1996, *ApJ*, 456, 541
- Thronson, Jr., H. A., Majewski, S., Descartes, L., & Hereld, M. 1990, *ApJ*, 364, 456
- Trumpler, R. J. 1930, *PASP*, 42, 214
- Tsuji, T., Ohnaka, K., Aoki, W., & Nakajima, T. 1996, *A&A*, 308, L29
- van der Bliik, N. S., Manfroid, J., & Bouchet, P. 1996, *VizieR Online Data Catalog*, 411, 90547
- van der Laan, H. 1966, *Nature*, 211, 1131
- Viehmann, T., Eckart, A., Moulataka, J., & Straubmeier, C. 2004, in *The Dense Interstellar Medium in Galaxies*, ed. S. Pfalzner, C. Kramer, C. Staubmeier, & A. Heithausen, 303–+
- Viehmann, T., Eckart, A., Schödel, R., et al. 2005a, *A&A*, 433, 117
- Viehmann, T., Eckart, A., Schödel, R., Pott, J.-U., & Moulataka, J. 2006, *ApJ*, 642, 861
- Viehmann, T., Eckart, A., Schoedel, R., et al. 2005b, *VizieR Online Data Catalog*, 343, 30117
- Voigt, H. H. 1991, *Abriss der Astronomie* (Spektrum Akademischer Verlag)
- Weisskopf, M. C., Brinkman, B., Canizares, C., et al. 2002, *PASP*, 114, 1
- Willner, S. P. 1978, *ApJ*, 219, 870
- Yuan, F., Markoff, S., & Falcke, H. 2002, *A&A*, 383, 854
- Yuan, F., Quataert, E., & Narayan, R. 2003, *ApJ*, 598, 301
- Yuan, F., Quataert, E., & Narayan, R. 2004, *ApJ*, 606, 894
- Yusef-Zadeh, F., Bushouse, H., Dowell, C. D., et al. 2006, *ApJ*, 644, 198
- Zhao, J.-H., Herrnstein, R. M., Bower, G. C., Goss, W. M., & Liu, S. M. 2004, *ApJ*, 603, L85
- Zhao, J.-H., Young, K. H., Herrnstein, R. M., et al. 2003, *ApJ*, 586, L29

# List of Figures

2.1	PSF and brightness profile of ISAAC <i>L</i> -band image . . . . .	9
2.2	Extinction laws of Rieke & Lebofsky (1985) and Moneti et al. (2001) . . . . .	16
2.3	Dimensionless parameters of spectral index $\alpha$ . . . . .	19
3.1	<i>K</i> -band light curve from July 07 . . . . .	24
3.2	890 $\mu\text{m}$ light curves from July 05-07 . . . . .	30
4.1	Extinction towards Sgr A* with new <i>M</i> -band result . . . . .	37
4.2	<i>H</i> -, <i>K</i> - and <i>M</i> -band view of IRS 3 . . . . .	38
4.3	NAOS/CONICA <i>L</i> -band view of IRS 3 . . . . .	39
6.1	<i>K</i> -band light curve from July 07 . . . . .	48
6.2	X-ray and NIR light curves on a common time axis . . . . .	49
6.3	Chandra X-ray light curve for 6/7 July 2005 . . . . .	50
6.4	The stellar cluster in the immediate vicinity of Sgr A* . . . . .	51
6.5	Chandra light curve for 5th/6th July 2005 . . . . .	52
6.6	The stellar cluster in the immediate vicinity of Sgr A* during its IQ flux density state . . . . .	54
6.7	The central $5.0'' \times 4.4''$ at 8.6 $\mu\text{m}$ and 19.5 $\mu\text{m}$ . . . . .	55
6.8	Flare amplitude as function of flare rate . . . . .	58
B.1	ISAAC <i>L</i> -band image of the Galactic center . . . . .	80
B.2	ISAAC <i>M</i> -band image of the Galactic center . . . . .	81
B.3	NAOS/CONICA <i>H</i> - and <i>K</i> -band images . . . . .	82
B.4	<i>K</i> – <i>L</i> vs. <i>H</i> – <i>K</i> two-color diagram . . . . .	82
B.5	<i>L</i> – <i>M</i> vs. <i>K</i> – <i>L</i> two-color diagram . . . . .	83
B.6	VISIR <i>N</i> -band three-color composite view of the Galactic center . . . . .	84
B.7	VISIR 19.5 $\mu\text{m}$ image of the Galactic center . . . . .	85
B.8	8.6 $\mu\text{m}$ view of the Galactic center showing newly detected stars . . . . .	86
B.9	SEDs of Galactic center mid-infrared sources . . . . .	87
B.10	SEDs of Galactic center mid-infrared sources . . . . .	88
B.11	Light curves of NIR observations in July 2004 . . . . .	89
B.12	VLA 43 GHz light curves . . . . .	90
B.13	Cross-correlation between NIR and X-ray data for flares $\phi 2/\text{I}$ , $\phi 3/\text{III}$ , $\phi 4/\text{IV}$ . . . . .	91
B.14	<i>HKL'</i> image of the central $2.6'' \times 2.6''$ . . . . .	92
B.15	Color and contour map of Sgr A* and dust component D1 . . . . .	93
B.16	NIR to MIR spectrum of Sgr A* during low flux state . . . . .	94
B.17	NIR to MIR spectrum of Sgr A* for X-ray/NIR flare $\phi 3/\text{III}$ . . . . .	95





# List of Tables

3.1	Observation log of July 2004 Sgr A* observations . . . . .	23
3.2	Details of July 2004 near-infrared observations . . . . .	23
3.3	Avg. position and flux density of Sgr A* from the NIR data . . . . .	25
3.4	8.6 $\mu\text{m}$ flux densities of Sgr A* . . . . .	26
3.5	X-ray flare count rates . . . . .	28
6.1	Emission properties of Sgr A* NIR flare events . . . . .	47
6.2	NIR/X-ray flare flux densities . . . . .	49
6.3	Emission properties of Sgr A* radio flare events . . . . .	53
6.4	Parameters for models of IQ and flare states of Sgr A* . . . . .	62
A.1	Photometry of sources detected in NAOS/CONICA and ISAAC images. The classifications are from Blum et al. (1996), with “cool” referring to red giants or supergiants and “red” signifying objects with featureless $K$ - band spectra and a strong IR excess. The zero-point for the positions is 17:45:42.93 RA -29:00:29.91 DEC (IRS 16NE) in the J2000 coordinate system, with an offset of 2.83” (RA) and $-0.91$ ” (DEC) from Sgr A* . . . . .	67
A.1	continued . . . . .	68
A.1	continued . . . . .	69
A.1	continued . . . . .	70
A.1	continued . . . . .	71
A.2	Photometry of sources outside the NAOS/CONICA field of view. See also table A.1. . . . .	71
A.2	continued . . . . .	72
A.2	continued . . . . .	73
A.2	continued . . . . .	74
A.2	continued . . . . .	75
A.2	continued . . . . .	76
A.3	Extinction corrected flux densities of compact $N$ -band sources. . . . .	76
A.4	Extinction laws of Rieke & Lebofsky (1985) and Moneti et al. (2001) . . . . .	78



# Acknowledgements

My special thanks go to the supervisor of my thesis, Prof. Dr. Andreas Eckart, for providing the opportunity to work on such an important and interesting field of research. His enthusiasm for and knowledge of astronomy has been a constant source of inspiration, and his permanent readiness to engage in discussions and provide advice and helpful suggestions and ideas have made it a pleasure to work with him and learn from his experience.

I would also like to thank all my colleagues and co-workers at the I. Physikalisches Institut, and in particular the members of the working group of Prof. Dr. Eckart, for providing a friendly and encouraging working environment.

In this context, I am especially grateful to Dr. Christian Straubmeier, for his excellent and enthusiastic provision of computer infrastructure and hardware support, and to Jens Zuther and Thomas Bertram for their patient and expert help with all software-related computer problems.

I am equally grateful to Dr. Rainer Schödel, for many helpful comments and fruitful discussions of Galactic center related topics, and to Jörg-Uwe Pott, who provided deeper insights into the nature of IRS 3 and dust shells and extinction in general.

Thanks are also due to the Deutsche Forschungsgemeinschaft for partly funding this work via grant SFB 494.

Last but not least, I am deeply indebted to my parents and the rest of my family for all the support they provided, and without which I never would have made it this far.

# Erklärung

Ich versichere, daß ich die von mir vorgelegte Dissertation selbständig angefertigt, die benutzten Quellen und Hilfsmittel vollständig angegeben und die Stellen der Arbeit – einschließlich Tabellen, Karten und Abbildungen –, die anderen Werken im Wortlaut oder dem Sinn nach entnommen sind, in jedem Einzelfall als Entlehnung kenntlich gemacht habe; daß diese Dissertation noch keiner anderen Fakultät oder Universität zur Prüfung vorgelegen hat; daß sie – abgesehen von unten angegebenen Teilpublikationen – noch nicht veröffentlicht worden ist sowie, daß ich eine solche Veröffentlichung vor Abschluß des Promotionsverfahrens nicht vornehmen werde. Die Bestimmungen dieser Promotionsordnung sind mir bekannt. Die von mir vorgelegte Dissertation ist von Prof. Dr. Andreas Eckart betreut worden.

(Thomas Viehmann)

## Teilpublikationen

Eckart, A., Baganoff, F. K., Schödel, R., et al. 2006, *A&A*, 450, 535: *The flare activity of Sagittarius A\*. New coordinated mm to X-ray observations*

Viehmann, T., Eckart, A., Moutaka, J., & Straubmeier, C. 2004, in “The Dense Interstellar Medium in Galaxies”, ed. S. Pfalzner, C. Kramer, C. Staubmeier, & A. Heithausen, 303–+: *The Galactic Center in the IR - VLT Infrared Observations of the Galactic Center*

Viehmann, T., Eckart, A., Schödel, R., et al. 2005, *A&A*, 433, 117: *L- and M-band imaging observations of the Galactic Center region*

Viehmann, T., Eckart, A., Schödel, R., Pott, J.-U., & Moutaka, J. 2006, *ApJ*, 642, 861: *Dusty Sources at the Galactic Center the N- and Q-Band Views with VISIR*

Viehmann, T., Eckart, A., Schoedel, R., et al. 2005, *VizieR Online Data Catalog*, 343, 30117: *L- & M-band imaging of the Galactic Center (Viehmann+, 2005)*

# Lebenslauf

Name	Viehmann
Vorname	Thomas
Geburtsdatum	24. September 1975
Geburtsort	Leiden (Niederlande)
Anschrift	Kölner Ring 130 50374 Erftstadt
Staatsangehörigkeit	deutsch
Familienstand	ledig

## Schulbildung

1981 - 1985	Grundschule Nordschule, Erftstadt-Lechenich
1985 - 1994	Städtisches Gymnasium Erftstadt-Lechenich
Juni 1994	Abitur
1994 - 1995	Wehrdienst

## Hochschulbildung

1995 - 2003	Studium der Physik an der Universität zu Köln
in 1999	Vordiplom (Physik)
2002 - 2003	Diplomarbeit am I. Physikalischen Institut der Universität zu Köln: <i>Infrared Observations of the Galactic Center</i>
November 2003	Diplom in Physik
Dez. 2003 - Apr. 2007	Wissenschaftlicher Mitarbeiter am I. Physikalischen Institut der Universität zu Köln
seit Dezember 2003	Doktorarbeit am I. Physikalischen Institut der Universität zu Köln Thema der Dissertation: <i>Near- and mid-infrared studies of the Galactic Center and Sagittarius A*</i> Betreuer: Prof. Dr. Andreas Eckart